THE INFLUENCE OF SHELL STRUCTURE ON NEAR-BARRIER FUSION OF NEUTRON-RICH NUCLEI

James Edgar Johnstone

Accepted by the Graduate Faculty, Indiana University, in partial fulfillment of the requirements for the degree of Doctor of Philosophy.

Doctoral Committee:

_____

Romualdo T. deSouza, Ph.D., Chair

_____

Charles J. Horowitz, Ph.D.

_____

Caroline C. Jarrold, Ph.D.

_____

Liang-Shi Li, Ph.D.

July 18, 2022

Acknowledgements

There are a myriad of people who have been integral to my growth in life and my advancement in science. I owe a great deal of that advancement to my advisor, Dr. Romualdo deSouza, who took a young scientist and put in the time and effort to show me how research is done. I have learned a lot during my time in the deSouza group and I am sure I would not be the scientist I am today without the opportunity to learn here at Indiana University.

I would also like to thank the rest of the Indiana University Nuclear Chemistry group. I will always be grateful to have been afforded the opportunity to work with Dr. Sylvie Hudan which meant my graduate education was spent directly learning from, not one, but two great nuclear scientists. I would like to give a special thanks for my fellow graduate students at IU: Dr. Blake Wiggins, Dr. Jessica Vadas, Carley Folluo, Conor McGee, Rohit Kumar Prajapat, and Hunter Desilets. The bond between graduate students is unique and I am grateful for the time we were able to learn and grow together. Additionally, I want to thank the undergraduate students who I worked with during my graduate career: Jacob Huston, Joshua Jun, Kamal Singh, Julian Spangler. I am excited to see where the world takes you!

I have been blessed to have had a wide array of educators pour into me as I have grown up. In particular, Mrs. Courtney Potts, Mr. Jason Wirth, and Dr. Gregory Powell all believed in me and helped to spark my love of science. Thank you for your belief and your encouragement and your love of teaching.

Lastly, I want to thank my friends and family for their continued support. My parents, Bruce and Marleen, have always been and continue to be supportive and encouraging in the path I chose to follow. My brothers, David and Matthew, exemplify what brothers should be and have been a great source of discussion both philosophical and scientific. My friends Caleb Cramer, Caleb Goode, Jamie Tutak, Andrew Vun, and Jacob Yansek have continued to lift me up during the difficulties of graduate school. And of course I am ever thankful for my wife, Amber, who has been by my side every day and has been a constant source of light and joy in my life.

James Edgar Johnstone

THE INFLUENCE OF SHELL STRUCTURE ON NEAR-BARRIER FUSION OF
NEUTRON-RICH NUCLEI

Understanding neutron-rich nuclear material is a topic at the forefront of physics
research and has far-reaching implications for many areas of nuclear science including nu-
clear astrophysics, heavy-element nucleosynthesis, and the nuclear equation-of-state. Fu-
sion studies are a unique tool for gaining access to an understanding of the nucleus far from
stability. Systematic fusion measurements along isotopic chains have provided insight into
how nuclear structure and dynamics change with increasing neutron number. Building
on previous studies, the near-barrier fusion cross-sections for ^{41,45}K,^{36,44}Ar+^{16}O,^{28}Si were
measured using an energy vs time-of-flight approach. The measurements were conducted
at Michigan State University's National Superconducting Cyclotron Laboratory using
the ReA3 facility. The measurements explored the behavior of fusion for both closed
neutron-shell nuclei as well as open neutron-shell nuclei. The measured fusion excitation
functions were compared to theoretical models showing the importance of both accurate
density distributions and dynamics in fusion.

As part of this experimental effort, high-quality ^{28}Si targets with reduced oxygen
content were also produced. Fabrication of these isotopically enriched, self-supporting
targets is detailed. These thin foils were characterized using a quartz crystal monitor,
X-ray photoelectron spectroscopy, and Rutherford back-scattering. In preparation for
future experiments near the neutron dripline, a new detector for measuring fusion was
developed. The detector, MuSIC@Indiana, was designed and constructed with several

unique features which allow for accurate and efficient measurement of the fusion excitation function at low beam intensities. MuSIC@Indiana was commissioned by the measurement of the $^{18}O+^{12}C$ fusion excitation function at the University of Notre Dame's Nuclear Science Laboratory's 10 MV Tandem Accelerator. An advanced data analysis technique, which improved upon the resolution presently achievable with MuSIC-type detectors, was successfully demonstrated with this dataset. This new analytic technique substantially enhances the impact of MuSIC-type measurements of fusion.

<div style="text-align: right;">

_____

Romualdo T. deSouza, Ph.D., Chair

_____

Charles J. Horowitz, Ph.D.

_____

Caroline C. Jarrold, Ph.D.

_____

Liang-Shi Li, Ph.D.

</div>

Contents

List of Figures

List of Tables

Abbreviations

AT-TPC	Active Target-Time Projection Chamber
CC	Coupled Channels
CN	Compound Nucleus
CSA	Charge Sensitive Amplifier
DC-TDHF	Density Constrained-Time Dependent Hartree Fock
DHB	Dirac-Hartree-Bogoliubov
DHFB	Dirac-Hartree-Fock-Bogoliubov
ER	Evaporation Residue
ETOF	Energy vs Time-Of-Flight
FRIB	Facility for Rare Isotope Beams
GANIL	Grand Accélérateur National d'Ions Lourds
GHS	Gas Handling System
GRB	Gamma Ray Burst
INTEGRAL	International Gamma-Ray Astrophysics Laboratory
LDM	Liquid Drop Model
LIGO	Laser Interferometer Gravitational-wave Observatory
MCP	Microchannel plate
MuSIC	Multi-Sampling Ionization Chamber
NSCL	National Superconducting Cyclotron Laboratory
PCB	Printed Circuit Board
QCM	Quartz Crystal Monitor
RIPD	Rare Ion Purity Detector
RGA	Residual Gas Analyzer
RBS	Rutherford Back-Scattering
RMF-SP	Relativistic Mean Field-São Paulo
SPP	São Paulo Potential
SBD	Surface Barrier Detector

TDHF	**T**ime **D**ependent **H**artree **F**ock
TFA	**T**iming **F**ilter **A**mplifier
TOF	**T**ime-**O**f-**F**light
XPS	**X**-ray **P**hotoelectron **S**pectroscopy

Chapter 1

Fusion of neutron-rich nuclei

1.1 Fundamental nuclear science

The structure and reactions of neutron-rich isotopes has been identified as a topic of immediate interest to the nuclear science community [1]. Nuclear properties such as binding energies, shapes, and energy levels have been both well-measured and well-modeled for most nuclei at and near the valley of β-stability [2]. As nuclei stray from stability, unusual properties can emerge. A well-known example of this is the large size of the ^{11}Li halo nucleus which has a neutron halo extending out to the size of ^{208}Pb resulting in an rms matter radius similar to ^{48}Ca [3]. A valuable measurement for understanding nuclear matter far from stability is the total fusion cross-section. Measurement of fusion near the Coulomb barrier provides access to information both on the static structure of the fusing nuclei as well as dynamical deformation that occurs during the reaction [4, 5, 6, 7]. Measurement of these properties provides a rigorous test to modeling of nuclear structure and works towards a comprehensive theory of all nuclei.

New facilities, like the Facility for Rare Isotope Beams (FRIB) will offer the opportunity to study the properties of these exotic nuclei [8]. Figure 1.1 shows a schematic of the FRIB accelerator. FRIB consists of a linear accelerator that accelerates a primary beam from an ion source up to 200 MeV/u onto a target producing an array of rare isotopes. Separation techniques allow the isotopes of interest to be isolated and then sent to experimental halls for measurements. FRIB will have the ability to produce over 1000 unique nuclei, many of which will be far from stability. The ability of FRIB to produce isotopes never before measured provides the opportunity for exploration into the nuclear *terra incognita.*

1
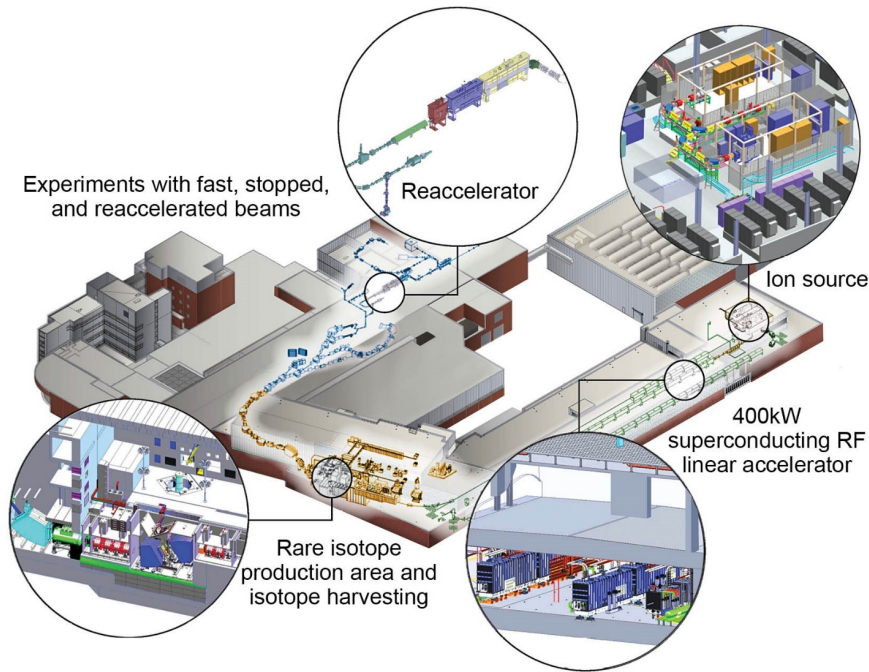
FIGURE 1.1: Schematic of the FRIB accelerator.

1.2 Neutron-rich environments

1.2.1 r-process nucleosynthesis

Understanding the structure and reactions of neutron-rich isotopes is directly tied to the understanding of several astrophysical phenomena. One of the foremost topics of nuclear science is the understanding of the creation of the chemical elements through the process known as nucleosynthesis. The main pathways of nucleosynthesis were initially identified in 1957 through the work of Burbidge, Burbidge, Fowler, and Hoyle [9]. The majority of the universe's hydrogen and helium along with a minor amount of lithium was produced in the first three minutes of the Big Bang. The rest of the lithium, along with the light elements beryllium and boron, are continuously being synthesized in the interstellar medium through collisions between nuclei and cosmic rays. The remaining elements are formed in nuclear reactions related to the stellar life-cycle.
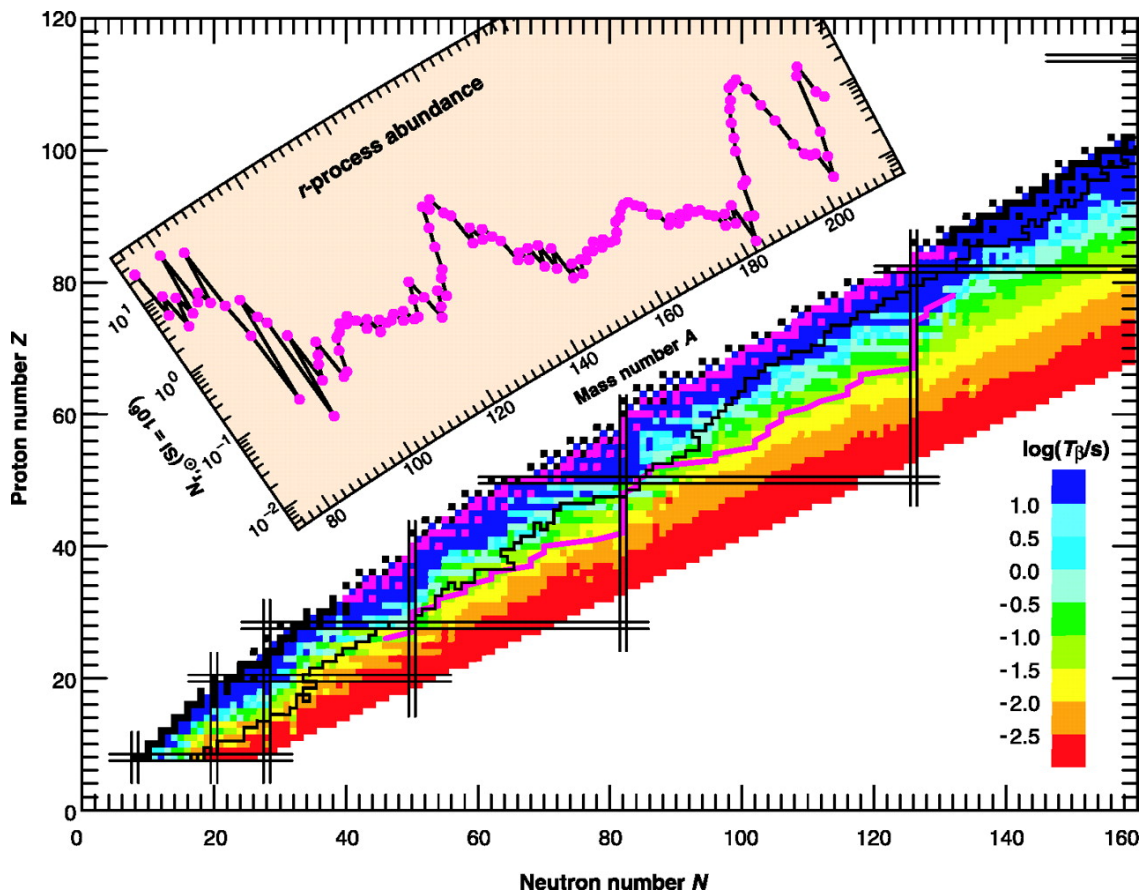
FIGURE 1.2: The Chart of the Nuclides. The inset shows isotopic abundances for heavier mass nuclides related to the r-process. Figure taken from [10].

Most of the life cycle of a star is spent fusing successively heavier elements beginning first with hydrogen. Upon reaching iron, the binding energy per nucleon reaches a maximum and fusion of heavier elements is no longer energetically favorable. Elements heavier than iron (A $\geq$ 60) are formed via neutron-capture. The two main processes governing heavy-element nucleosynthesis are known as the slow neutron-capture process (s-process) and the rapid neutron-capture process (r-process). In both these capture processes, a heavy 'seed' nucleus captures a neutron and then subsequently undergoes β^- decay to a higher atomic number. Successive occurrence of this process leads to the formation of the elements with A $\geq$ 60. In both the s-process and the r-process, the neutron capture process competes with β^- decay. The β^- decay lifetimes, τ_β, which range from milliseconds

3

to hours set the timescale for determining the pathway of neutron capture. Figure 1.2 presents the Chart of the Nuclides colored according to τ_β. As nuclei become increasingly neutron-rich and move away from stability, τ_β decreases quickly. Conversely, the neutron capture timescale, τ_n, depends primarily on the density of neutrons in the environment. In the s-process, which occurs at low neutron density, the neutron capture timescale τ_n is long relative to τ_β meaning a nucleus is likely to undergo β^- decay prior to capturing an additional neutron. Because of this the s-process is responsible for synthesis of mid-mass elements close to the valley of β-stabilty up to bismuth [2].

Figure 1.3 shows a zoomed-in portion of the Chart of the Nuclides with the pathways of the s-process and r-process visualized by the blue and red arrows, respectively. As shown by the blue arrows, the s-process is restricted from synthesizing nuclei away from stability by β^- decay. Conversely, in the r-process multiple neutron captures can happen prior to a β^- decay due to the high neutron density. The r-process requires a neutron density of $\sim 10^{28}$ neutrons/m^3 indicating a heavily neutron-rich environment is necessary [11]. Such high-density neutron environments can only be transient. After the high neutron density is no longer present, the extremely neutron-rich nuclei which have been formed will decay back to stability. Through the initial production of nuclei far from stability the r-process synthesizes the heaviest elements and neutron-rich isotopes. The inset of Figure 1.2 shows the abundance pattern for purported r-process nuclei.

It has long been known that approximately half of all nuclei for elements heavier than iron are produced via the r-process [9], but it remained unclear whether the r-process occurs predominantly in core-collapse supernovae or compact binary mergers [13, 14]. The discussion of the primary location for r-process nucleosynthesis has recently been brought back to the forefront of nuclear science with the beginning of the era of gravitational wave astronomy. On August 17 2017 the Laser Interferometer Gravitational-wave Observatory (LIGO) network [15] in conjunction with the Virgo gravitational-wave
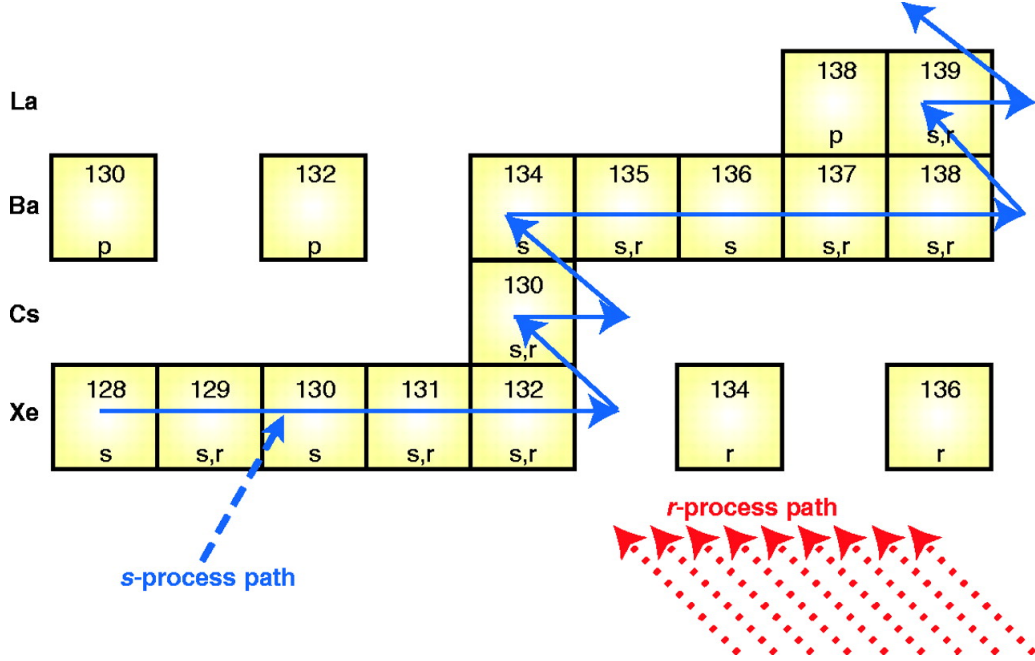
FIGURE 1.3: Schematic showing the s-process and r-process. Figure taken from [12].

observatory [16] recorded gravitational waves from a binary neutron star merger [17]. The coincident gamma-ray burst (GRB), GRB 170817A, was observed independently by the Fermi Gamma-ray Burst Monitor and the International Gamma-Ray Astrophysics Laboratory (INTEGRAL) [18, 19]. The subsequent optical transient from the event, which was observed over the following weeks, was consistent with significant production of r-process elements [20]. This observation of the red-shift of the optical spectrum signaled binary neutron star mergers as a significant, possibly primary, site of r-process nucleosynthesis.

1.2.2 Accreting neutron stars

Other neutron-rich environments of interest are accreting neutron stars. A neutron star is the remnant core following a supernova explosion [21]. With a typical radius of ~10 km and a mass of ~1.4 solar masses, a neutron star can achieve densities greater

than the density of atomic nuclei ($2\text{x}10^{14}$ g/cm^3) [22]. True to its name, a neutron star is largely composed of neutrons. The structure of a neutron star is complex depending principally on the density which ranges from $1\text{x}10^6$ g/cm^3 at the surface to $7\text{x}10^{14}$ g/cm^3 in the interior. In the outer crust, structures known as 'nuclear pasta' with interesting properties exist [23, 24]. Their unique composition of primarily neutrons combined with their extremely high density makes neutron stars a fascinating environment of neutron-rich material.

Neutron stars can exist in binary systems with other celestial bodies including main sequence stars which are primarily composed of hydrogen. In such binary systems, hydrogen from the companion star is slowly accreted onto the surface of the neutron star. There hydrogen is processed into helium. Continued accretion and fusion causes the temperature to rise finally resulting in thermonuclear runaway. This releases a burst of 10^{38} ergs of energy observed as a bright x-ray flash lasting $\sim$10 seconds [25]. The cycle of accretion and release is cyclical giving these types of systems the name 'pulsars'.

Some neutron star binary systems produce more energetic x-ray 'superbursts' at irregular intervals. Superbursts can last from 2 to 12 hours and release $\sim$$10^{42}$ ergs of energy. The origins of these energetic x-ray superbursts is not fully understood but are thought to involve the ignition of ^{12}C+^{12}C [26]. However, due to the higher Coulomb barrier relative to hydrogen or helium, carbon fusion requires a temperature of at least $5\text{x}10^8$ K. The surface temperature of neutron stars is 2 orders of magnitude lower at $\sim$$3\text{x}10^6$ K, which is too low for fusion of ^{12}C to consistently occur. A proposed solution to this inconsistency is the fusion of neutron-rich isotopes on the outer crust of the neutron star acting to ignite the ^{12}C+^{12}C fusion. Theoretical calculations have shown the fusion of neutron-rich isotopes of heavier nuclei to be enhanced relative to their β-stable counterparts [27]. This fusion of neutron-rich heavier nuclei has been hypothesized to provide a heat source triggering the x-ray superbursts.

The understanding of neutron-rich matter is particularly important to understanding both the formation of the heavy elements in the r-process [28] and the fusion of neutron-rich nuclei in neutron stars. The nuclei involved in the s-process are typically close to stability and readily accessible for terrestrial studies. Consequently, the cross-sections for nuclei involved in the s-process are better understood than the r-process [29]. Next generation radioactive beam facilities now enable measurement of fusion for unavailable nuclei. A particularly useful strategy is measurement along an isotopic chain of increasingly neutron-rich nuclei. By uncovering trends related to neutron richness, the behavior of the most exotic nuclei can be predicted.

Chapter 2

Fusion models

2.1 Modeling the isolated nucleus

The initial structure of the atomic nucleus was proposed by Ernest Rutherford in 1911 following the results of the Geiger-Marsden gold foil experiment [30]. The experimenters observed deflection of α particles to large angles passing through the gold foil suggesting a concentration of positive charge at the center of the atom. With the discovery of the neutron in 1932 by Chadwick [31], the physical picture of the nucleus was modified to account for both constituents of a nucleus namely protons and neutrons [32, 33, 34, 35]. Additional experimental evidence required expanding the theoretical perspective in order to describe the quantal structure of the nucleus. To present theoretical models of fusion it is necessary to briefly describe two of these fundamental nuclear models: the liquid drop model and the nuclear shell model.

2.1.1 Liquid drop model

An extremely useful description of the nucleus that accounts for its binding comes from modeling the nucleus as an incompressible, uniformly-charged liquid drop. This liquid drop model (LDM) describes the nucleus in a macroscopic way and does not account for single particle interactions between nucleons in the nucleus. In the LDM, the binding energy of a nucleus (E_b) is given according to the Bethe-Weizsacker formula (also called the semi-empirical mass formula):

$$E_b(Z, A) = C_1 A - C_2 A^{2/3} - C_3 \frac{Z^2}{A^{1/3}} - C_4 \frac{(A - 2Z)^2}{A} + \delta(A, Z) \qquad (2.1)$$

The first term is known as the volume term. Each nucleon contributes to the total binding energy via the strong nuclear force and this term therefore depends on the total number of nucleons in a nucleus (A). It is empirically known, consistent with the saturative nature of the nuclear strong force, that the nuclear radius, R, is proportional to $A^{1/3}$. Therefore, the volume is: $V_{sphere} = \frac{4}{3}\pi R^3 \propto A$. Due to its linear dependence on A, the first term of the LDM is therefore referred to as the volume term. The empirically-determined value of the constant C_1 is related to the strength of the strong nuclear force.

The second term accounts for the presence of the nuclear surface. Nucleons at the surface are less tightly bound as they are not fully surrounded by other nucleons. Because of the relationship between R and A, we can take the surface area to be: $SA_{sphere} = 4\pi R^2 \propto A^{2/3}$.

The third term accounts for the repulsive Coulomb force experienced between protons. The Coulomb energy for a sphere is written as $E_C = \frac{3Z^2 e^2}{5R}$ where Z is the atomic number of the nucleus. Substituting for R, $E_C \propto \frac{Z^2}{A^{1/3}}$.

The fourth term, known as the symmetry term, reflects decreased binding due to an asymmetry between the number of protons and neutrons in a specific nuclide understood as the quantal nature of the two-component nuclear droplet. This term comes from the discrete states occupied by both neutrons and protons in the nucleus and the Pauli principle which says that each nucleon has to occupy its own unique state. In a perfectly symmetric nucleus (N=Z) the protons and neutrons will occupy the lowest possible states. As a nucleus becomes more asymmetric, the occupation of higher energy levels by the surplus neutrons or protons reduces the binding of the nucleus. This reduction in binding is proportional to $\frac{(A-2Z)^2}{A}$.

The fifth term represents the increased stability which comes from fully paired spins between nucleons. This term can be either attractive or repulsive depending on the atomic
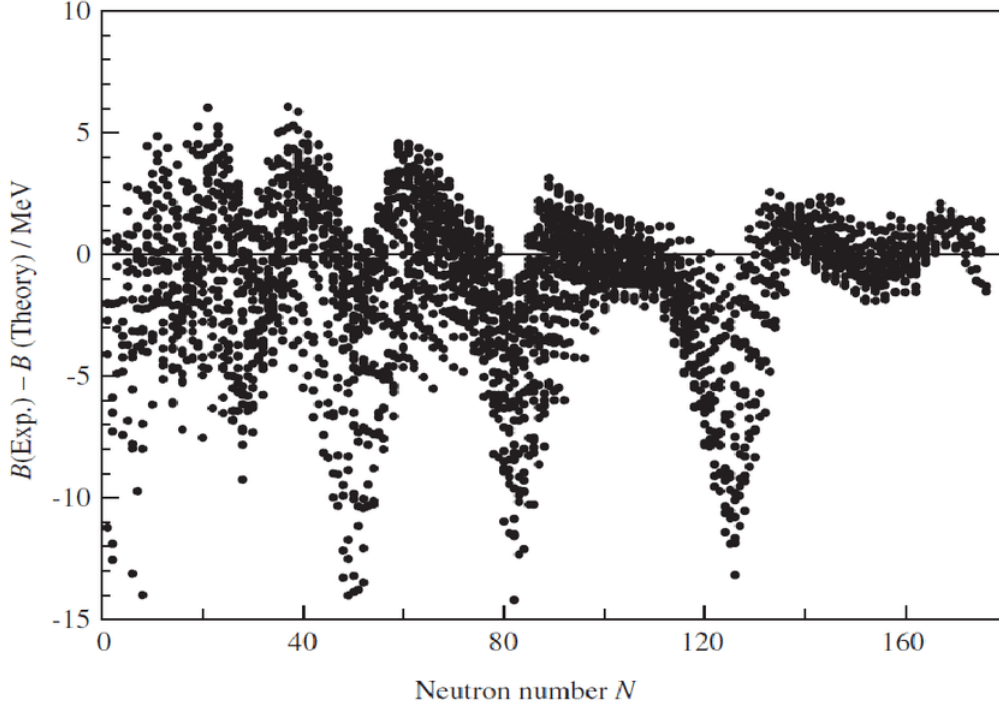
FIGURE 2.1: The deviation between the liquid drop model and experimental binding energies. Figure taken from [36].

numbers and neutron numbers of the nucleus. For odd-A nuclei, the pairing term is zero. For nuclei with even Z and even N (even-even) δ is positive (enhanced binding) and for odd-odd nuclei δ is negative (reduced binding). The values of the constants C_x are determined empirically in order to fit measured binding energies. Other, more complex descriptions of the nucleus as a liquid drop beyond the Bethe-Weizsacker formula have been introduced but are of lesser magnitude and therefore negligible in their impact on fusion.

2.1.2   Shell model

Figure 2.1 shows the deviation between the LDM and experimentally measured binding energies as a function of neutron number. Enhanced binding beyond the LDM is manifested at specific 'magic numbers'. These specific neutron numbers correspond

to nuclear shell closures. Nuclei at these numbers exhibit stronger binding analogous to the high ionization energy and decreased reactivity of the noble gases. The shell model describes the behavior of individual nucleons in a confining potential [37]. Inclusion of strong spin-orbit coupling is necessary to properly reproduce the observed shell structure. Other evidence for shell structure exists beyond the enhanced binding at these particular N and Z values including:

1. Large elemental abundances at shell closures.

2. Termination of naturally occurring radioactive series at a shell closure.

3. Reduced neutron absorption cross-sections for isotopes with a closed neutron-shell.

4. Maximum of the neutron separation energy for closed-shell isotopes followed by a sharp decrease for the next heavier isotope.

5. Near-zero electric quadrupole moments for closed-shell nuclei.

6. Large energy difference between the nuclear ground state and first excited state for closed-shell nuclei as compared to open-shell nuclei.

2.2 Static fusion models

When considering the fusion of two nuclei, it is helpful to build up a description with terms of increasing complexity. A reasonable starting point is to attempt to describe fusion simply using the LDM. However as is seen even for isolated nuclei, the LDM does not provide an adequate picture to fully account for observed experimental results. In addition to the LDM, the shell model can be added to the physical description of fusion. The influence of the nuclear shell structure on fusion will be the focus of this thesis. Other terms beyond the LDM and shell structure can have strong effects on the fusion

cross-section. Both the LDM and the shell model are built around describing the isolated nucleus. As two nuclei fuse however, they can undergo dynamic deformations which can drastically influence the barrier to fusion and the fusion cross-section. There are several approaches to modeling these dynamic deformations that will be described in this chapter. The influence of dynamic deformations is explored in Chapter 4. Other terms may influence the fusion cross-section. For example, many-body correlations, such as clustering, can manifest during the fusion process. This thesis focuses on measurement of fusion with mid-mass nuclei where the influence of such correlations will be reduced. As such, the effects of these terms are not explored in this thesis..

2.2.1 Overview of the fusion barrier

Modeling two nuclei as they react requires knowledge of the ground state and possibly excited state configurations of the isolated nuclei as well as their interaction. As the two nuclei approach each other, their interaction is governed by the internuclear potential. Two of the fundamental forces are relevant for nucleus-nucleus interactions: the electromagnetic force and the strong nuclear force. Only the protons are affected by the electromagnetic force which affects the approaching nuclei via the repulsive Coulomb potential of the form:

$$V_C(r) = \frac{Z_1 Z_2 e^2}{r} \tag{2.2}$$

V_C is given simply by the interaction of two point charges of charge Z_1 and Z_2 at a distance r. When the two nuclei are relatively far apart (non-overlapping) the point Coulomb approximation is valid.

At close range, the protons and neutrons of the two nuclei will interact via the strong nuclear force. This force results in an attractive nuclear potential:

$$V_N(r) = \frac{-V_0}{1 + e^{(r-R_0)/A}} \tag{2.3}$$

Here, V_N is approximated using a Wood-Saxon potential where V_0 is the depth of the attractive potential well, r is the distance between the two nuclei, R_0 is the sum radii of the isolated nuclei, and a is a parameter which defines the diffuseness of the potential.

In addition to these two potentials which stem from fundamental forces, for non-central collisions the internuclear potential contains an additional term: the centrifugal potential. This potential acts to increase the barrier and is dependent upon the angular momenta of the colliding nuclei. This potential is given by the form:

$$V_l(r) = \frac{\hbar^2 l(l+1)}{2\mu r^2} \tag{2.4}$$

Where l is the angular momentum and μ is the reduced mass. The total potential, V_T, is the sum of these three terms:

$$V_T(r) = V_C(r) + V_N(r) + V_l(r) \tag{2.5}$$

An example of the internuclear potential is presented in Figure 2.2 for ^{9}Be+^{208}Pb. Figure 2.2a shows separately the three component terms which make up V_T. The Coulomb term, V_C, is shown as the solid green line and the nuclear term, V_N, is shown as the solid red line. Three values of angular momentum, $l = 30$, 60, and 90, are shown as the dashed lines. In Figure 2.2b the total potential for these values of angular momentum as well as $l = 0$ are shown. It can clearly be seen that larger angular momentum in the system yields a higher barrier and a smaller potential pocket.
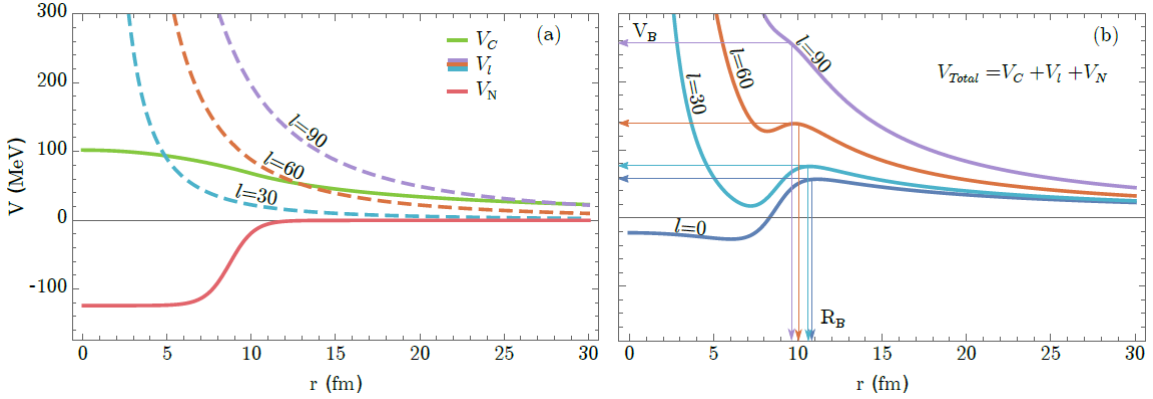
FIGURE 2.2: The internuclear potential for ^{9}Be+^{208}Pb. Panel (a) shows the contributions to the total potential from Coulomb (V_C), (nuclear) V_N, and (centrifugal) V_l. Panel (b) shows the sum of these components to give the total potential. Figure taken from [38].

There are several methods to calculate the fusion cross-section using the potential. The simplest way is to treat the two nuclei as static objects, meaning the potential between them is unchanged throughout the fusion process. This simple model is known as the one-dimensional barrier penetration model (1D-BPM) [39].

Classically, the cross-section for the scattering of the two nuclei can be considered as concentric rings with radii equal to integer values of the reduced de Broglie wavelength, λ [40]. For a given l-wave, the cross-sectional area is:

$$\sigma_l = (2l + 1)\pi \lambda^2 \tag{2.6}$$

When quantum mechanics is considered, the transmission probability of the incoming wave, T_l, must be taken into account. The semi-classical expression for the partial cross-section then becomes:

$$\sigma_l = (2l + 1)\pi \lambda^2 T_l \tag{2.7}$$

To calculate the total fusion cross-section, the cross-section for each partial wave is

summed. As the transmission probability for each l-wave will have an energy dependence, the total fusion cross-section will also have an energy dependence. The total fusion cross-section is therefore given as the sum over all l-waves including the associated energy-dependent transmission probabilities [41]:

$$\sigma_{fus}(E) = \pi \lambdabar^2 \sum_{l=0}^{\infty} (2l+1) T_l(E) \tag{2.8}$$

The transmission probabilities can be found by approximating the total barrier, V_T, as an inverted parabola with height V_B and width $\hbar\omega$. Transmission through this barrier can be solved analytically with the solutions given by the Hill-Wheeler formula [42]:

$$T_l(E) = \frac{1}{1 + exp[\frac{2\pi}{\hbar\omega}(V_B - E)]} \tag{2.9}$$

The total fusion cross-section is then given by:

$$\sigma_{fus}(E) = \pi \lambdabar^2 \sum_{l=0}^{\infty} \frac{2l+1}{1 + exp[\frac{2\pi}{\hbar\omega}(V_B - E)]} \tag{2.10}$$

The potential parameters are typically calculated using an Akyuz-Winther formalism [43] but they can also be chosen in order to match experimental cross-sections measured far above the barrier where the cross-section is determined by the geometric size of the nuclei [44, 45, 46]. This model does not include any dynamics. As access to dynamical collective modes would lower the barrier particularly at lower energies, this model often underpredicts fusion cross-sections at sub-barrier energies [47].

2.2.2   São Paulo model and relativistic mean field approach

The São Paulo (SP) model provides a means to calculate the fusion cross-section in a parameter free way [48]. The São Paulo model is based on the effects of the Pauli

nonlocality and utilizes a double folding potential, V_F, which is a function of the distance between the nuclei, r [49, 50]:

$$V_F(r) = \int \rho_1(r_1)\rho_2(r_2)v(r - r_1 + r_2)dr_1 dr_2 \qquad (2.11)$$

The key element of the folding potential is the nuclear density distributions, ρ_x, which depend on the nuclear radii, r_x. The folding potential can be obtained by use of systematics for the density distribution of the two nuclei [51] or from more fundamental calculations of the density (relativistic mean field). V_F is modified by the relative local velocity between the two nuclei, v, by the factor e^{-4v^2/c^2}. For the near-barrier fusion reactions considered in this thesis the modification due to the relative local velocity is negligible.

A common way to calculate the nuclear density distributions is to use a relativistic mean field (RMF) approach [52]. RMF theory is built upon three basic assumptions:

1. Nucleons act like point-like particles.

2. Lorentz invariance must be adhered to.

3. Strict causality is obeyed.

In RMF theory the nucleus is treated as a quantum mechanical many-body system of fermions interacting via two-body interactions. This interaction occurs through an exchange of mesons between two nucleons described by a relativistic Lagrangian. The parameters of this Lagrangian, such as the number of mesons, their masses, and their coupling constants, are empirically determined to reproduce experimental data in many nucleon systems. Ultimately, this approach determines the ground state properties of a nucleus including the ground state binding energy, charge radius, and nucleon density distributions.

16

Once the nucleon density distributions have been determined by RMF, they can be used in the São Paulo folding potential. The nuclear potential produced by RMF-SP calculations is much deeper and more diffuse than the Woods-Saxon potential used in the 1D-BPM (Equation 2.3) which causes the total potential, V_T, to be much deeper at close distances. This has implications for calculating the cross-section at sub-barrier energies where the São Paulo barrier is narrower than the Wood-Saxon barrier. As with the 1D-BPM, the São Paulo method calculates the fusion cross-section using Equation 2.10.

2.2.3 Dirac-Hartree-Bogoliubov

RMF theory has been successfully used to describe the ground-state properties of nuclei near the stability line. However, for these calculations the pairing interaction is often neglected. For nuclei near the drip-line where the Fermi level is close to the continuum, the coupling between bound and continuum states should be taken into account explicitly [53]. Dirac-Hartree-Fock-Bogoliubov (DHFB) theory was developed [54] to provide a more precise relativistic description of pairing correlations and subsequently used to calculate nuclear density distributions [55, 56]. These DHFB calculations, however, were observed to be inconsistent with nonrelativistic calculations [57].

The Dirac-Hartree-Bogoliubov (DHB) model was developed as a direct extension of DHFB where the exchange term is neglected but the Dirac structure of the pairing interaction is retained [53]. Figure 2.3 shows a table comparing the experimental binding energies and ground state deformations for several isotopes of krypton and strontium to the DHB calculated values. Good agreement between the calculated values and the experimental values is observed over a wide range of masses.

TABLE II. Binding energies and ground state deformations of the even isotopes of Kr and Sr for c_{pair}=0.58.

| | Kr | | | | | Sr | | | |
| | B.E. | | β | | | B.E. | | β | |
A	DHB	Expt.	DHB	M-N	A	DHB	Expt.	DHB	M-N
72	−604.25	−607.11	−0.32	−0.35	76	−635.48	−638.08	0.49	0.42
74	−629.51	−631.28	−0.30	0.40	78	−661.70*	−663.01	−0.17 (0.47)	0.42
76	−653.51*	−654.23	−0.20 (0.00)	0.40	80	−686.41	−686.28	0.00	0.05
78	−675.86	−675.55	0.00	−0.23	82	−709.43	−708.13	0.00	0.05
80	−696.75	−695.43	0.00	0.06	84	−730.94	−728.90	0.00	0.05
82	−716.19	−714.27	0.00	0.07	86	−750.99	−748.92	0.00	0.05
84	−734.19	−732.26	0.00	0.06	88	−769.17	−768.46	0.00	0.05
86	−750.29	−749.23	0.00	0.05	90	−782.74	−782.63	0.00	0.05
88	−762.20	−761.80	0.00	0.06	92	−795.15*	−795.75	−0.12 (0.10)	0.08
90	−773.08*	−773.21	−0.14 (0.14)	0.16	94	−807.22	−807.81	−0.18	0.26
92	−783.63*	−783.22	−0.27 (0.20)	0.23	96	−818.67	−818.10	−0.23	0.34
94	−793.59	−791.76	−0.29	0.31	98	−829.36	−827.87	−0.26	0.36
96	−802.77	−799.95	−0.16	0.34	100	−839.29	−837.62	−0.25	0.37

FIGURE 2.3: Table comparing DHB calculated binding energies and ground state deformations to experimental values for isotopes of Kr and Sr. Figure taken from [53].

The DHB model can make subtle modifications to the nuclear surface, extending and modifying the nuclear density. These changes, particularly at the tail of the density distribution, can have a large impact on the fusion cross-section despite their small magnitude. This is particularly true for near- and sub-barrier energies where fusion is particularly sensitive to the tails of the proton and neutron density distributions which govern the initial interaction between the two nuclei.

2.3 Dynamic fusion models

2.3.1 Coupled-channels approach

Simple barrier penetration models for fusion perform reasonably well in describing the fusion of light stable nuclei, but consistently underpredict the fusion cross-section for

heavier and more exotic systems particularly below the barrier. Such models approximate the fusing nuclei as rigid objects which only interact elastically so the only variable in the reaction is the nuclear separation distance. In reality, the fusing nuclei are complex objects which can follow non-elastic channels (including inelastic excitations and transfer) during the fusion process.

In a static fusion model, the fusing nuclei are essentially frozen in their ground state configurations. At near-barrier energies, however, where the two nuclei approach each other adiabatically, single-particle excitations and particle transfers can play an important role prior to fusion [58]. The coupled-channels (CC) approach provides a framework for considering the coupling to intrinsic nuclear intrinsic degrees of freedom including low-lying excited states and nucleon transfer processes.

Several assumptions are made in the CC approach. First, non-collective excitations and giant resonances are ignored and only low-lying collective modes are considered. Second, the low-lying excited states which are considered are taken to be the same as the isolated nucleus, without accounting for any changes in states that occur as the nuclei deform during fusion. Third, the nuclei are approximated as either rigid rotors or harmonic oscillators depending on which picture more appropriately describes the experimentally observed states of the isolated nuclei. The coupled channels approach has been realized in several model codes [59, 60, 61].

Figure 2.4 shows experimental fusion cross-sections for ^{16}O+^{154}Sm and ^{58}Ni+^{58}Ni. Compared to the experimental data are calculations for inert nuclei shown as the blue-dashed line and labeled 'single-channel'. These calculations clearly underpredict the measured fusion cross-section. For the left panel, the red line shows CC calculations which include coupling to rotational bands in ^{154}Sm. For the ^{58}Ni+^{58}Ni reaction in the right panel, quadrupole excitations up to the double phonon states are taken into account.
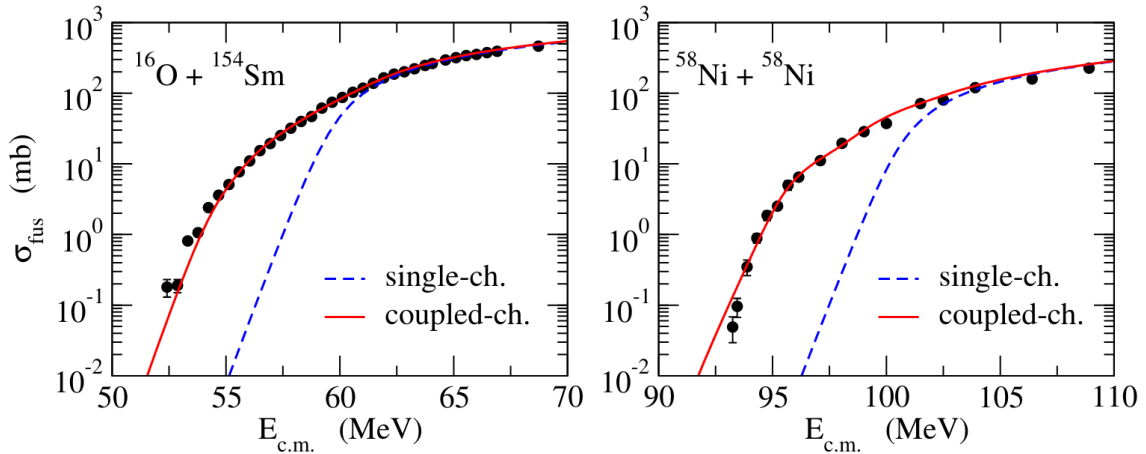
FIGURE 2.4: Fusion cross-sections for ^{16}O+^{154}Sm (left panel) and ^{58}Ni+^{58}Ni (right panel). Experimental data are from [62] (left panel) and [63] (right panel). Figure taken from [64].

In both instances, the CC calculations provide a reasonable description of the data and are a vast improvement over static calculations at below-barrier energies.

2.3.2 Time-dependent Hartree Fock approach

An alternate approach in describing nuclear dynamics in heavy-ion reactions is the time-dependent Hartree-Fock (TDHF) method. In contrast to the static fusion models discussed in Section 2.2 and even to coupled-channel calculations, this theory provides a fully microscopic theory of large amplitude collective motion to the fusion process. TDHF treats the nuclei as a many-body problem, allowing for collective motion through a time-dependent nuclear energy-density functional [65]. Because the TDHF approach calculates dynamics on a mean field level it does not have to identify specific channels including surface excitations and nucleon transfer. For exotic nuclei this is a great advantage over CC calculations as the levels of the exotic nucleus may not be known. TDHF has been consistently shown to reproduce experimental results [66, 67, 68], however a major

limitation to the semi-classical TDHF approach is the inability to calculate fusion cross-sections below the barrier.

To overcome this problem, a density-constrained TDHF (DC-TDHF) theory was developed. DC-TDHF employs a density constraint to provide a microscopic description of the formation of shape resonances in light systems [69]. In the DC-TDHF approach, the TDHF time evolution proceeds uninhibitedly. At certain times or internuclear distances, the instantaneous TDHF density is used to perform a static Hartree-Fock energy minimization while constraining both the proton and neutron density distributions via the instantaneous TDHF densities. This allows the single-particle wave-functions to re-arrange themselves so as to minimize the total energy while remaining within the density constraint [67, 68]. The interaction potentials calculated by DC-TDHF incorporate entrance channel effects such as neck formation, particle exchange, internal excitations, and deformations [70]. DC-TDHF only takes as its input the Skyrme effective nucleon-nucleon interaction with no adjustable parameters [67, 68].

Figure 2.5 shows the DC-TDHF calculated fusion cross-sections for $^{16}O+^{16}O$, $^{16}O+^{24}O$, $^{24}O+^{24}O$, and $^{16}O+^{28}O$ along with experimentally measured $^{16}O+^{16}O$ data. Good agreement is observed between the DC-TDHF calculated cross-sections and the experimental data. The calculations with neutron-rich oxygen provide some interesting results. The addition of 8 extra neutrons to one of the reacting nuclei ($^{16}O+^{24}O$) causes an enhancement to the fusion cross-section when compared to the symmetric $^{16}O+^{16}O$ excitation function. This result can be understood as the extension of the neutron-density distribution which lowers the fusion barrier. This effect persists when adding additional neutrons to the same nucleus; the most asymmetric collision $^{16}O+^{28}O$ has the largest cross-sections of the shown systems. However, adding an 8 additional neutrons to the projectile to make the reaction $^{24}O+^{24}O$ causes a reduction in the cross-section nearly to the level of the stable counterpart. This reduction is understood as being due to the presence of a repulsive
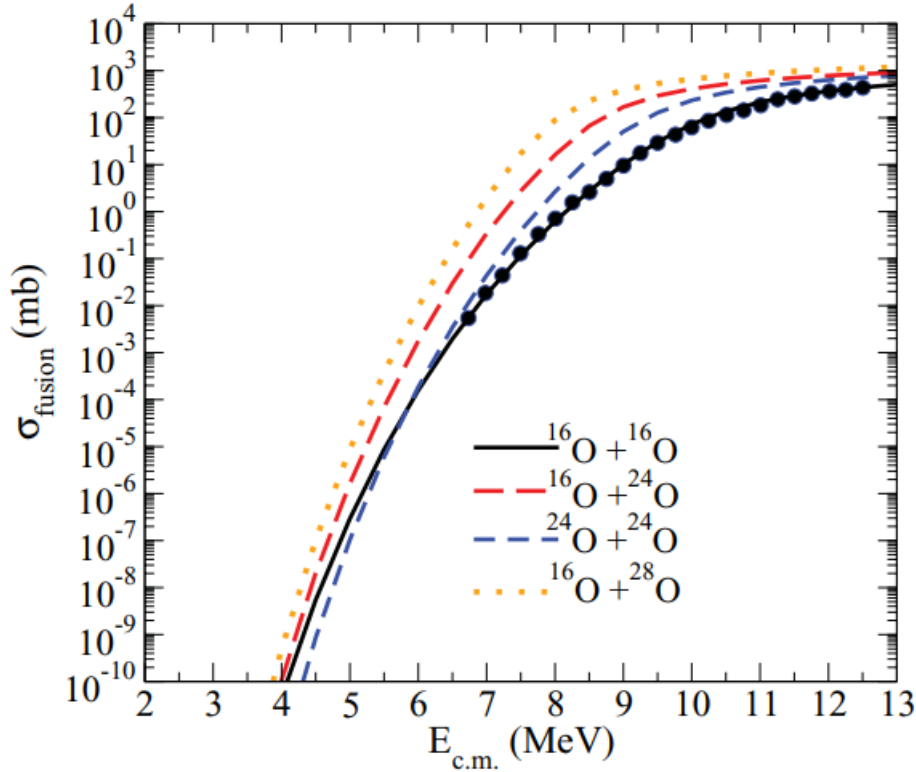
FIGURE 2.5: Cross-sections for various oxygen isotopes calculated using DC-TDHF. The experimental data points shown as the closed circles are from [71]. Figure taken from [70].

Pauli potential between the two nuclei [67, 72, 73].

The predictions of these theoretical models further motivate experimental measurements for neutron-rich isotopes. Do neutron-rich nuclei undergo fusion as predicted by static or dynamic models? At what point do reaction dynamics become important? Is fusion enhanced or suppressed for neutron-rich nuclei relative to stable nuclei? How does this enhancement or suppression depend on the energy relative to the fusion barrier? Such experimental measurements are now possible at a new generation of radioactive beam facilities that promise to make previously inaccessible nuclei available for the first time [74, 75, 76]. The availability of neutron-rich beams at such facilities allows the systematic exploration of fusion for an isotopic chain of neutron-rich nuclei [4, 5, 6, 7, 77].

Chapter 3

Experimental methods

Nuclear reactions are characterized by the outcome of the reaction which depends upon the energy and impact parameter of the reaction. A visual summary of these outcomes is shown in Figure 3.1. At large impact parameters, the two reacting nuclei interact only through the Coulomb force and the projectile nucleus elastically scatters from the target nucleus. If the two nuclei collide at a smaller impact parameter the strong nuclear force becomes involved in the reaction and other outcomes become possible. When the two nuclei interact at a range smaller than the sum of the projectile and target radii, then a nucleon in either the projectile or target may be excited to an unoccupied energy state. If the nucleon does not leave the nucleus, then the projectile is inelastically scattered and will have less energy than before the reaction. If the excited nucleon(s) leaves the projectile or target then a direct reaction occurs. A direct reaction can result in one or a few nucleons being transferred or ejected from the projectile or target. These reactions are known as transfer and knockout reactions respectively. More central impact parameters result in deep-inelastic scattering. In this case a dinuclear system is formed by the projectile and target and a substantial amount of charge and mass is exchanged while the projectile's kinetic energy is dissipated before the dinuclear system separates into two product nuclei.

For yet more central collisions, a single compound nucleus (CN) is formed which is the amalgamation of the projectile and target nuclei. At energies near the Coulomb barrier, the CN de-excites via the emission of γ rays and light particles (in particular protons, neutrons, and α particles). These reactions are designated fusion-evaporation reactions. The residual nucleus which remains after particle evaporation is known as the evaporation
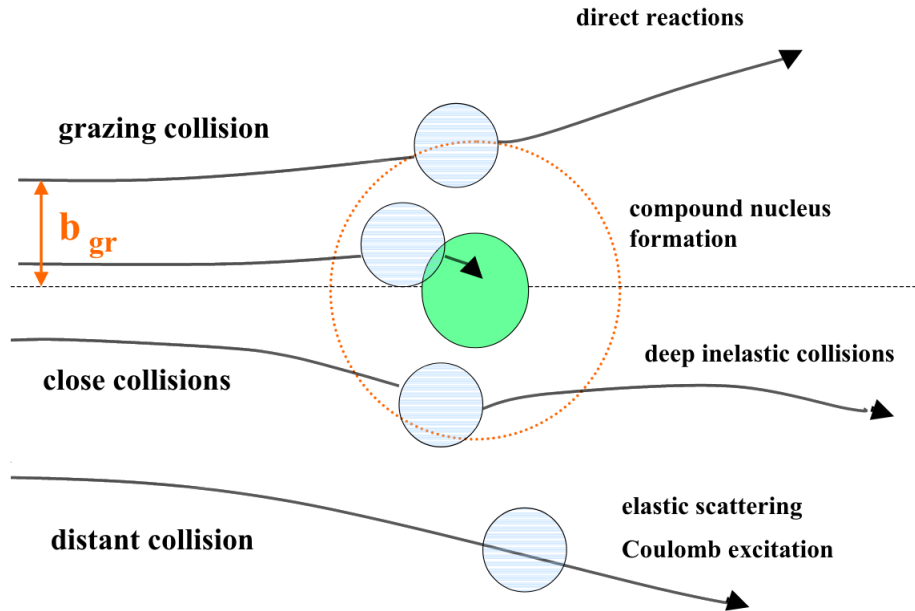
FIGURE 3.1: Diagram of nuclear reaction outcomes based on impact parameter. Figure taken from [78].

residue (ER). The decay of the CN into the ER occurs on the timescale of 10^{-15}-10^{-21}s. This thesis focuses on measurement and understanding of fusion-evaporation reactions of neutron-rich nuclei.

3.1 Measuring fusion with thin targets

3.1.1 ΔE-E measurements

Fusion reactions are studied through either the direct or indirect identification of fusion evaporation residues. Evaporation residues can be identified by detecting the decay γ-radiation characteristic of the evaporation residue or through direct ER detection. Detection of ERs typically requires that targets be 'thin' so that the ER can exit the target with sufficient energy to be detected. Use of a thin target also means that the beam only

loses a small amount of energy in the target allowing the energy at which the fusion occurs to be known precisely.

One of the common methods of identifying fusion in thin target measurements is known as the ΔE-E method. In this technique a telescope consisting of two detectors, a thin transmission detector and a thick stop detector, arranged in a stack is used. The energy loss of a particle (ΔE/Δx) which passes through a medium is given by:

$$\frac{\Delta E}{\Delta x} \propto \frac{Z^2 A}{E}$$

where Z is the particle's atomic number, A is the particle's mass number, and E is the particle's kinetic energy. A particle's identity can thus be determined by making a measure of its energy loss with this two-detector telescope. Because ΔE/Δx depends on Z^2 two incident particles with different atomic numbers can be distinguished. Any particle which traverses the first detector in the stack deposits an energy, ΔE, in the transmission detector before depositing its remaining energy, E-ΔE, into the stop detector. By plotting ΔE vs E, nuclei of different Z can be properly identified and heavier fusion ERs can be distinguished from beam scattering events. A major limitation to this approach is the fact that residues must have enough energy to leave the target *and* penetrate the transmission detector. A modified version of this technique is described in the development and implementation of MuSIC@Indiana presented in Chapter 6.

3.1.2   Energy vs Time-of-Flight measurements

An alternate technique for identification of fusion using thin targets is the direct detection of ERs through energy vs time-of-flight measurements (ETOF). In this method, a particle's mass is determined by both its energy and the time it takes to transverse

a fixed distance. The expression for the kinetic energy (E) of a particle can then be rearranged to yield an expression for its mass (m):

$$E = \frac{1}{2}m\frac{d^2}{t^2} \Rightarrow m \propto Et^2$$

where t is its time-of-flight (TOF) to traverse a fixed distance (d). This technique was used for measuring the fusion of ^{36,44}Ar,^{41,45}K+^{16}O,^{28}Si in experiment E17002 and will be the focus of this chapter.

A simple diagram showing how fusion can be identified through ETOF is presented in Figure 3.2. In this approach, the beam impinges on a target which is contained inside of a start timing detector. This detector records the time at which the beam interacts with the target. If fusion occurs, a compound nucleus will be formed and subsequently de-excite through the emission of light charged particles (primarily protons and α particles) and neutrons. The emission of these light particles imparts a transverse momentum to the evaporation residue away from the beam axis. Stop detectors, which measure energy and time, can then be placed downstream of the target in an orientation which allows the majority of unreacted beam to pass through while maintaining a good efficiency for detecting the evaporation residues. The beam which is elastically or inelastically scattered into a stop detector is distinguished from ERs by the energy recorded in the stop detector and the TOF between the start detector and the stop detector. An example ETOF spectrum from the measurement of ^{18}O+^{12}C [79] is shown in Figure 3.3. The major feature of the spectrum is the intense peak of elastically scattered ^{18}O beam appearing at E = 34 MeV and TOF = 10 ns. Extending down from this peak to lower energy and higher TOF is a tail of inelastically scattered beam. To the right of the scattered beam towards higher mass the island of ERs can be clearly distinguished.

26
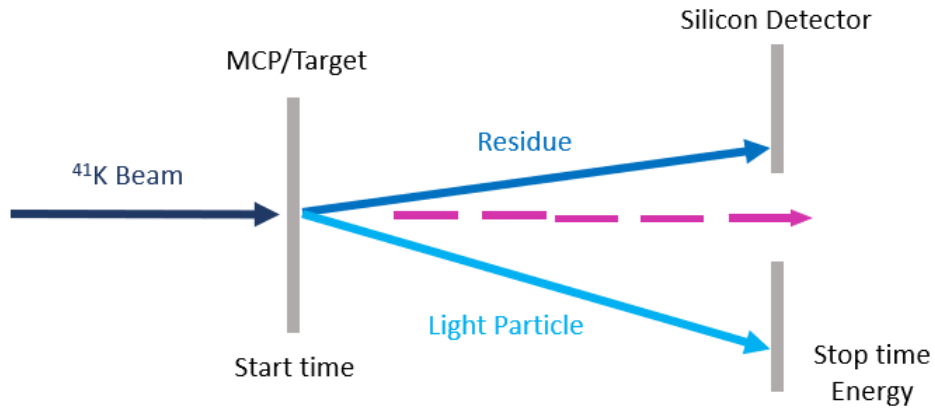
FIGURE 3.2: Diagram of the ETOF experimental technique.
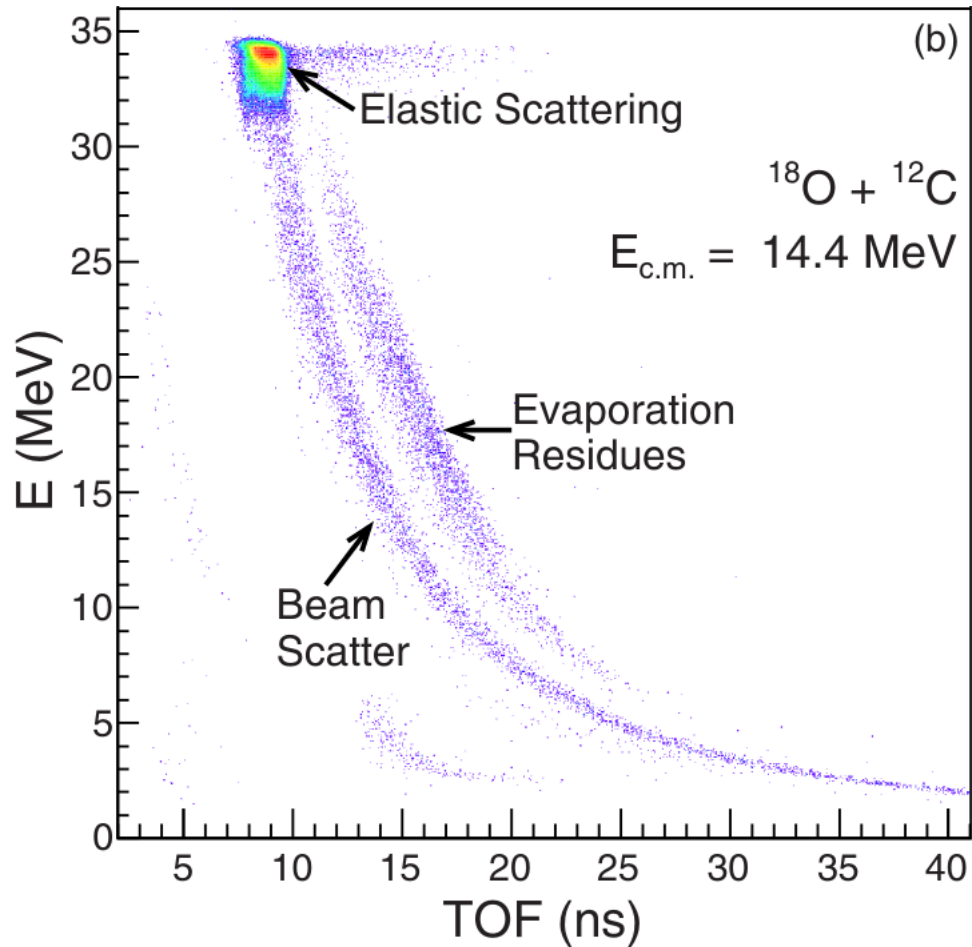
FIGURE 3.3: Experimental ETOF spectrum from the measurement of $^{18}O+^{12}C$. The island of fusion evaporation residues can be clearly seen separated from the ^{18}O beam scatter. Figure taken from [79].

27
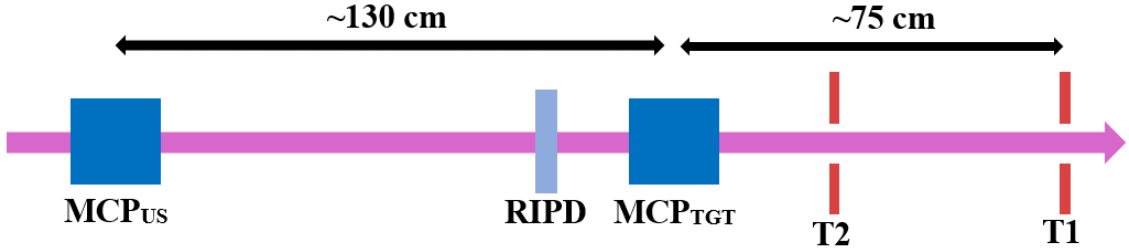
FIGURE 3.4: Schematic of the experimental setup used in E17002 (presented in Chapter 4). The distances from the target foil to T1 and T2 are 75.45 cm and 22.25 cm, respectively.

Figure 3.4 schematically depicts the experimental ETOF setup used in E17002. The beam first passes through an E×B microchannel plate (MCP) detector [80]. The E×B MCP design has been implemented in previous ETOF experiments to minimize the amount of material in the beam path in an effort to minimize scattering into the downstream silicon detectors [81]. E17002 measured the fusion cross-section for several radioactive isotopes which required identification of contaminant ions in the beam. To distinguish the ions of interest from contaminants in the beam, the beam is passed through the Rare Ion Purity Detector (RIPD). RIPD is an axial-field ionization chamber that allows for particle identification on an event-by-event basis using ΔE-TOF [82]. RIPD is designed to have fast timing for a gas detector which allows the detector to be used at beam rates up to 3×10^5 particles/s [82]. After passing through RIPD, the beam passes through another E×B MCP detector. The secondary emission foil in this E×B detector serves as the target for the reaction of interest.

Downstream of the target foil, evaporation residues are detected in two annular silicon detectors designated T1 and T2. Both silicon detectors used in the experiment were the S9 design from Micron Semiconductor. The S9 design is an annular detector that is segmented into 16 pie-like segments on its ohmic side and 8 concentric rings on its junction side. A central hole in the detector allows unreacted beam to pass through

minimizing radiation damage to the detector. The segmentation provides a measurement of θ and ϕ for the detected particle. The S9 detectors are nominally 300 μm thick. This thickness more than suffices to stop the highest-energy evaporation residues produced in the fusion reaction. The detector has a thin entrance window of just 0.1-0.2 μm Si equivalent which is thin enough to allow the lowest-energy evaporation residues to be detected. The ability to detect low-energy residues is a distinct advantage of ETOF over ΔE-E.

The procedure for creating ETOF spectra from the raw data is outlined in Ref. [83]. Once the ERs have been identified using the ETOF 2D spectrum, the fusion cross-section can be calculated using:

$$\sigma_{fusion} = \frac{N_{ER}}{(N_{beam} * t * \epsilon_{ER})}$$

In the above equation σ_{fusion} is the cross-section for fusion, N_{ER} is the number of evaporation residues, N_{beam} is the number of beam particles, t is the target thickness, and ϵ_{ER} is the geometric efficiency. As the majority of beam particles are not measured in the silicon detectors, the beam must be counted without using the ETOF data. N_{beam} is determined via a coincident measurement between the two MCP detectors. The target thickness can be determined in several ways. Measurement techniques of the target thickness are discussed in greater detail in Chapter 5.

In order to calculate the geometric efficiency, ϵ_{ER}, the statistical model code EVAPOR [84] is used. EVAPOR simulates the decay of the compound nucleus for the desired nuclear reaction using a Hauser-Feshbach formalism to describe the de-excitation. The code provides the angular and energy distributions for the de-excitation products (both residues and light particles). These evaporation residue angular distributions together with the positions of the T1 and T2 detectors determines the geometric efficiency. Figure 3.5 shows a residue angular distribution that is representative of all the different reactions measured in experiment E17002. The angular distribution of all the fusion products is
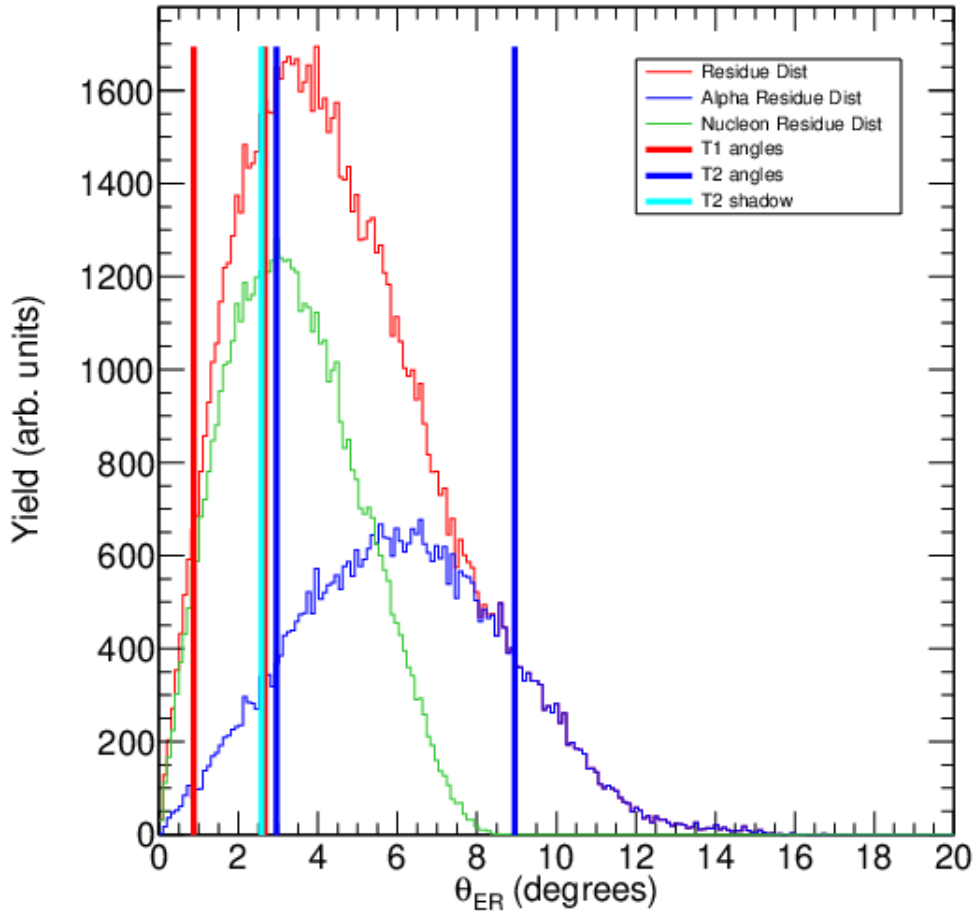
FIGURE 3.5: Angular distribution from EVAPOR for ^{36}Ar + ^{28}Si at $E_{lab} = 80$ MeV. This distribution is representative of the distributions for all systems and all energies measured during E17002.

presented as the red histogram. It extends from zero degrees (the beam axis) to a maximum angle of approximately sixteen degrees. This distribution can be understood as being comprised of two subsets of events. The first subset are evaporation residues produced through the de-excitation of only nucleons (protons or neutrons). The angular distribution associated with these events is presented as the green histogram. The second subset of events are decays involving emission of at least one α-particle. This distribution is presented as the blue histogram. The emission of an α-particle is typically associated

with a larger transverse momentum of the ER, hence a larger angle. The angular coverage for T1 and T2 are represented by the vertical lines. The line labeled 'T2 shadow' represents the angle which is blocked due to inactive silicon in the central hole of the T2 detector. For the T1 and T2 distances used in E17002, the geometric efficiency was between 78-84% for all isotopes in the measured energy range.

3.2   Measuring fusion with thick targets

3.2.1   Gamma-ray measurements

Another way to identify evaporation residues is by detecting their unique decay pathways. When the compound nucleus has de-excited to an evaporation residue, the ER will still retain some amount of internal excitation which will be emitted as γ rays. Each nucleus has its own characteristic γ rays and so by measuring this radiation the specific exit channels of the reaction can be identified. Multiple states may be populated in an ER, and so the branching ratios between the states for each ER must be known to properly extract the fusion cross-section.

Because γ rays are highly penetrating radiation, thicker targets can be employed which allows reactions with smaller cross-sections to be measured. This technique has previously been used in the measurement of fusion [71] and is particularly valuable for understanding astrophysical reactions which occur at sub-barrier energies and microbarn cross-sections. However, because this approach requires knowledge of the decay properties of the fusion ERs, this technique is difficult to use for reactions with neutron-rich nuclei where ERs may be far from stability and the states may be unknown.

31

3.2.2 MuSIC detector overview

The techniques described in the previous sections are well-established and work well particularly for beam intensities above 10^4 particles/s. Beams of the most exotic N/Z nuclei however, dictated by their short half-lives, are only available at low-intensity. The low-intensity of these radioactive beams suggests a thick-target approach as an effective means for measuring cross-sections. The potential for using γ ray measurements is limited when considering these nuclei due to the uncertainty related to the unknown single-particle levels in the neutron-rich residues.

In recent years, active thick-target measurements have gained visibility in low-energy nuclear physics with the increasing use of time-projection chambers [85, 86, 87, 88, 89, 90]. In an active target detector, most often a gas detector, the detector gas functions both as the target as well as the means of detection. However, use of these powerful and complex detectors, often rate-limited in their readout, is not warranted for all measurements. Experiments focused at measuring the total fusion cross-section can make use of a simpler approach. A particularly simple active, thick-target detector suitable for fusions is a Multi-Sampling Ionization Chamber (MuSIC).

MuSIC detectors are transverse-field, Frisch-gridded ionization chambers with segmented anodes [91]. The segmentation of the anode transverse to the beam direction allows the energy loss of a particle traversing the detector to be measured as a function of its position along the beam axis. For a single incident particle the measurement of the collective ΔE values measured in a MuSIC detector is referred to as a 'trace'. As it traverses the detector, the beam loses energy in the detector gas at a rate characterized by its specific ionization. If a fusion event occurs at a given position the compound nucleus formed is higher in atomic number and mass number than the incoming beam. At energies near and below the fusion barrier, excitation of the compound nucleus is modest,

32

E*= 30-50 MeV, and consequently light-particle de-excitation of the compound nucleus results in an evaporation residue with atomic and mass number that are also higher than those of the beam. The ERs can thus be identified by a marked increase in energy deposit (ΔE) due to their increased atomic and mass number. The segmentation of the anode means fusion events are associated with discrete locations (and therefore discrete energies) inside the detector. MuSIC detectors are intrinsically efficient as they measure multiple points on an excitation function for a single incident beam energy and provide an angle-integrated measurement of the fusion cross-section.

While MuSIC detectors were originally developed for use in high-energy heavy-ion experiments [91, 92, 93], more recently their use has been extended to low energy nuclear reactions namely the measurement of the fusion excitation function for $^{10-15}$C+^{12}C [77, 94], ^{17}F+^{12}C [95], and ^{17}O+^{12}C [96]. These measurements have shown the viability of MuSIC detectors in reproducing fusion results from thin target measurements as well as extending isotopic chains to neutron-rich nuclei as shown for the reaction of ^{X}C+^{12}C in Figure 3.6.

Additionally, MuSIC detectors have been utilized for studies of (α,n)/(α,p) reactions [98, 99]. Figure 3.7 demonstrates the ability of MuSIC detectors to reproduce results for (α,n) reactions measured via direct neutron detection. It is nicely shown that the MuSIC data matches the literature cross-sections at the overlapping energies. However, Figure 3.7 also demonstrates a disadvantage to measuring reactions with MuSIC detectors. Because each event of interest is assigned to an anode, the energy at which that reaction occurs is constrained only by the energy of the beam at the front and back of each anode. This energy loss is dependent upon the size of the anode and the gas pressure being used but is often several MeV in the lab reference frame. This leads to wide energy error bars and loss of fine structure in a measured excitation function as is clearly evident in Figure 3.7. The same phenomenon is observed for fusion measurements. Wide energy error bars are
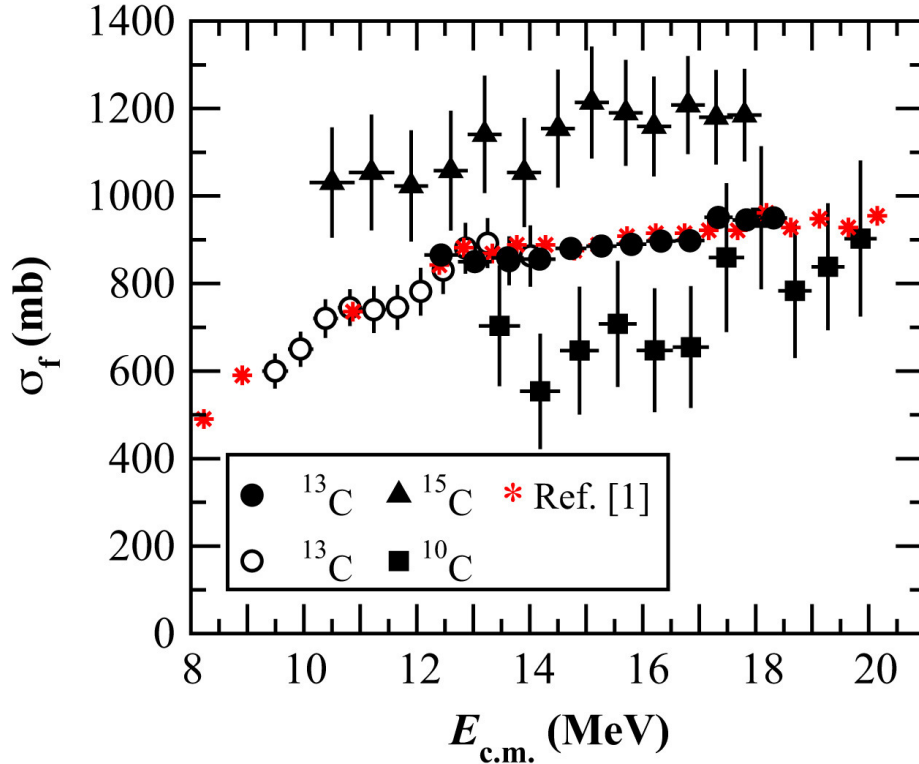
FIGURE 3.6: Fusion excitation functions of ^{10,13,15}C$+^{12}$C measured using a MuSIC detector. Figure taken from [94]. The excitation function in red labeled as 'Ref. [1]' in the legend is from [97].

observed for the fusion measurements in Figure 3.6 but have significantly less impact on the measurement as the excitation function is relatively smooth in this energy region.

Despite this inherent limitation, MuSIC detectors also have advantages over thin-target measurement techniques. One significant benefit to the MuSIC technique is that MuSIC detectors operate best at low-intensities ($< 10^5$ particles/s) where the beam rate does not have a significant effect on the performance of the detector gas. This makes the technique complimentary to ETOF and ΔE-E measurements which are valuable for making high-resolution measurements when beam rates are high. In contrast to the thin-target approach where the incident beam energy must be changed, MuSIC detectors allow measurement of multiple points on the excitation function simultaneously [94].
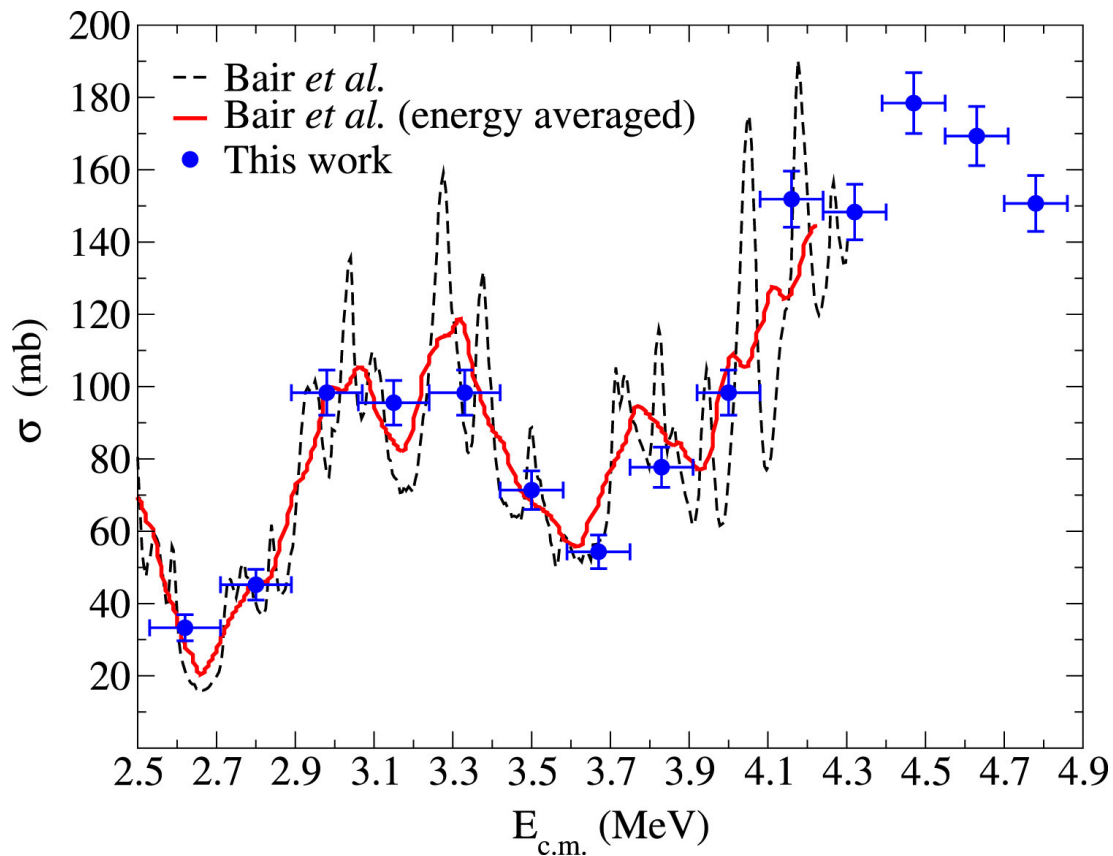
FIGURE 3.7: Cross-section of the $^{17}O(\alpha,n)^{20}Ne$ reaction as measured using a MuSIC detector and reported in [99]. The dataset labeled 'This work' in blue is from [99] and the data sets labeled 'Bair et al.' in red and black are from [100].

This ability is what allows MuSIC detectors to efficiently measure excitation functions for beams at rates $\sim 10^3$ particles/s.

MuSIC detectors hold other advantages over thin-target measurements beyond being able to measure at lower beam rates. Thin-target measurements are often performed with limited angular coverage due to the geometry of the detectors used in identifying the fusion via either ΔE-E [97, 101] or ETOF [81] techniques. Extraction of the fusion cross-section thus requires integration of the angle and energy distributions for the individual heavy products introducing an uncertainty into the total extracted fusion cross-section. As MuSIC detectors have 100% detection efficiency, the use of a MuSIC detector provides a direct integrated measure of the fusion cross-section. Additionally, MuSIC detectors

are self-normalizing since the incident beam is detected by the same detector along with the reaction products. These characteristics make MuSIC detectors an efficient means for measuring fusion excitation functions for neutron-rich nuclei when the beam intensity is limited.

In preparation for measurements of fusion of highly neutron-rich nuclei, a MuSIC detector (MuSIC@Indiana) was designed, constructed, and tested. The details of the construction and commissioning with $^{18}O+^{12}C$ is presented in Chapter 6. Development of a new analysis technique to localize the position of fusion within a MuSIC detector consequently reducing the energy uncertainty in the excitation function is described.

3.3 Fusion measurements

3.3.1 Re-accelerated radioactive beams at ReA3

The measurement of $^{39,41,45}K$ and $^{36,44}Ar + ^{28}Si$ (E17002) was carried out at Michigan State University National Superconducting Cyclotron Laboratory (NSCL) ReA3 hall. The radioactive beams were produced using projectile fragmentation at the NSCL's coupled cyclotron facility. In E17002 a primary beam of ^{48}Ca at 140 MeV/A was accelerated onto a Be production target. At these energies the collision of the projectile and target nuclei fragments the projectile producing a broad spectrum of product nuclei with exotic N/Z ratios. These forward going reaction products were filtered by a magnetic separator to provide the beam of interest. This separator at NSCL is designated the A1900 fragment separator [102].

Figure 3.8 shows a schematic diagram of the path of the radioactive beam after being produced by projectile fragmentation. After separation by the A1900, the beam was transported and directed onto a linear gas cell, as shown in Figure 3.8. This cell
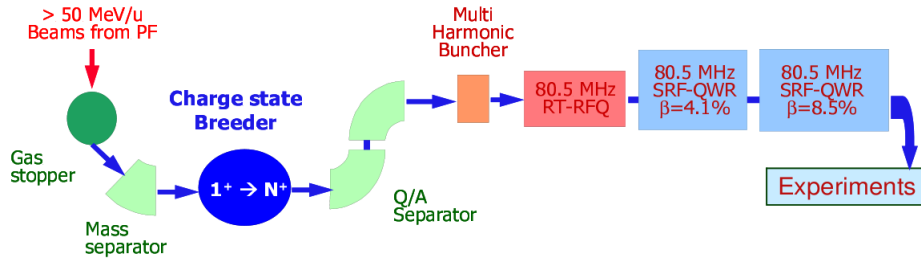
FIGURE 3.8: Schematic of the ReA3 accelerator at NSCL. Figure taken from [103].

was used to thermalize the beam from the high energies needed for fragmentation. The thermalized ionzed were then extracted from the gas stopper and mass separated before being passed through a charge breeder creating n^+ charge state ions. The ions were subsequently sent through a charge state (Q/A) separator where an optimal Q/A was selected in order to reduce beam contaminants. From here, the ions entered the ReA3 linear re-accelerator where they were accelerated to 2-3 MeV/A with a radio frequency of 80.5 MHz. Using a re-accelerated beam provides advantages in that the beam energy can be easily changed and the beam can be focused on the target. The beam delivered to the experiment had a beam spot of ∼4 mm diameter. For the stable beams measured in E17002, an ion source directly fed the charge breeder. The results of these measurements are presented in Chapter 4.

3.3.2 Stable beams at Notre Dame

The commissioning of MuSIC@Indiana took place at the University of Notre Dame's FN Tandem Van de Graaff accelerator. A beam of negative ions was created using an ion source and then accelerated toward a stripper foil at positive potential situated at the center of the tandem. Removal of electrons by the carbon stripper foil produces a positive ion which is accelerated away from the stripper foil and toward the end of the

accelerator. The beam is analyzed by charge/mass using a 90° dipole analyzing magnet before being transported to the experimental setup.

The beam used for the commissioning was ^{18}O delivered into the experimental setup at a rates between 10^3-10^5 particles/s to measure fusion in ^{18}O+^{12}C. To calibrate the detector beams of ^{19}F, ^{23}Na, ^{24,26}Mg, ^{27}Al, and ^{28}Si were also used. The results of the MuSIC@Indiana commissioning are discussed in further detail in Chapter 6.

Chapter 4

Measurement of ^{36,44}Ar,^{41,45}K+^{16}O,^{28}Si

Enhancement of the fusion cross-section for neutron-rich nuclei, driven by their extended neutron density distributions, is a topic of considerable experimental and theoretical interest [104, 105]. Theoretical calculations of the fusion of oxygen isotopes using a density-constrained TDHF approach found an enhancement of fusion for the asymmetric system ^{24}O + ^{16}O as compared to ^{16}O + ^{16}O and the São Paulo model [70]. This enhancement can be plainly understood as neutron transfer between the projectile and target which modifies the potential between the nuclei and lowers the barrier. Interestingly, fusion of nuclei at the limit of stability, namely ^{24}O + ^{24}O, are however suppressed relative to ^{24}O + ^{16}O. This suppression cannot be explained by the simple picture in which additional neutrons act to continuously reduce the barrier and enhance fusion. A more intricate description of neutron-rich nuclei is required to understand these results. Recent experimental measurements provide evidence that presence of one additional neutron gives rise to a large fusion enhancement due to either the presence of a one-neutron halo (^{15}C) [106] or a single unpaired neutron (^{19}O) [5].

Similar results have been seen in mid-mass neutron-rich systems. Early investigation of fusion in Ni + Ni observed an increase in the sub-barrier fusion cross-section associated with the presence of valence neutrons and proposed neutron exchange as one possible process responsible [107]. However, examination of Ca + Ca collisions reveals that neutron-richness of the colliding nuclei alone is not the only factor impacting the fusion probability. While a ^{48}Ca projectile manifests a larger fusion cross-section with a ^{40}Ca target as compared to a ^{40}Ca projectile [108], fusion of ^{48}Ca + ^{48}Ca is suppressed below the barrier [109].

In order to expand upon the reactions of mid-mass nuclei away from β-stability, the Indiana University group has investigated near-barrier fusion for isotopic chains of neutron-rich nuclei. The specific goal of this research is to understand the role of nuclear structure and dynamics on fusion as a function of neutron number. Initial measurements of the fusion excitation functions for ^{39,47}K + ^{28}Si [4] revealed that the neutron-rich isotope manifests an enhanced fusion cross-section relative to the stable isotope. Figure 4.1 shows the experimental cross-sections for fusion of ^{47}K + ^{28}Si and ^{39}K + ^{28}Si in panels (a) and (b), respectively. The experimental data was parameterized using a functional form that describes the penetration of an inverted barrier (labeled 'Wong' in Figure 4.1) [110]. Also presented are cross-sections calculated using the São Paulo model and RMF frozen density distributions [48]. A clear discrepancy between the calculated and measured excitation functions is observed at below-barrier energies.

Panel (c) shows the ratio of the Wong fits for radioactive isotope compared to the stable isotope. The sub-barrier enhancement of ^{47}K can be clearly seen. The data is also compared with coupled-channels (CCFULL) calculations which incorporate coupling to the excited states of the nuclei [58]. Inclusion of only the excited states in CCFULL, labeled 'dynamical deformation' in the figure, failed to reproduce the experimental data. With inclusion of neutron transfer into the CCFULL calculations, the experimental fusion enhancement of the neutron-rich ^{47}K can be described.

In an effort to expand fusion measurements along the potassium isotopic chain, experiment E17002 was conducted at Michigan State University National Superconducting Cyclotron Laboratory's (NSCL) ReA3 reaccelerator hall. Experiment E17002, which measured the near-barrier excitation functions of ^{41,45}K on a ^{28}Si target using an energy vs time-of-flight (ETOF) approach, is described in the following sections. The goal of measuring fusion for these isotopes was to provide additional data along the potassium isotopic chain while probing fusion away from the N=20 and N=28 closed neutron-shells.
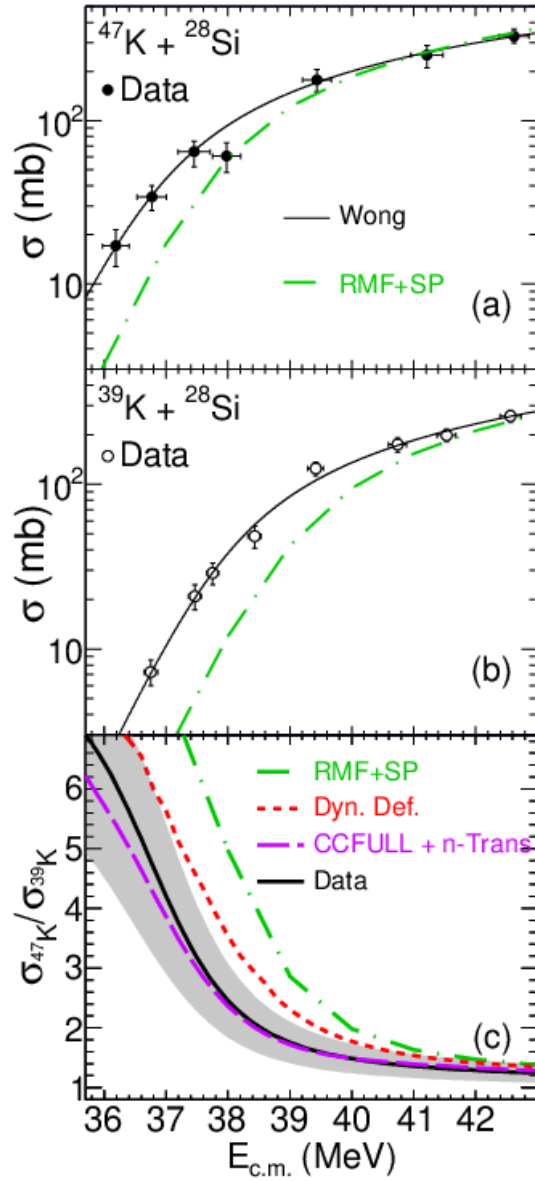
FIGURE 4.1: Experimental fusion excitation functions for ^{47}K+^{28}Si (panel a) and ^{39}K+^{28}Si (panel b) with comparison to a static model for fusion (RMF-SP). The ratio of the two excitation functions using the Wong formalism is shown in panel c along with comparison to RMF-SP and dynamical models for fusion (Dyn. Def. and CCFULL+n-Trans). Figure taken from [4].

41

Additionally, the excitation functions for ^{36,44}Ar + ^{28}Si were also measured during E17002 in an effort to understand the effect of the unpaired proton in K by measuring similar reactions in which the neutrons and protons are paired in both the projectile and target. Experimental cross-sections for reaction of each projectile on contaminant ^{16}O in the target were also measured.

4.1 ^{36,44}Ar,^{39,41,45,47}K+^{16}O

4.1.1 K,Ar + ^{16}O excitation functions

The ^{28}Si targets used in E17002 contained significant amounts ($\sim$40%) of oxygen contamination. While the presence of the oxygen acted as a background to the intended measurement on ^{28}Si, residues from the two reactions were able to be distinguished. Details of the residue identification are given in Chapter 3 and efforts to reduce the oxygen contamination are described in Chapter 5. Despite the unintended presence of the oxygen in the target, the additional cross-sections provide the opportunity to probe fusion of the projectile nuclei on a fully-paired, closed-shell target.

Presented in Figure 4.2a are the fusion excitation functions for ^{39,45,47}K + ^{16}O. As expected, based on the presence of eight additional neutrons, ^{47}K exhibits a larger fusion cross-section than ^{39}K. The additional neutrons in ^{47}K should not only correspond to a larger size for the nucleus (cross-section) but should also be associated with a stronger attractive potential moving the excitation function towards lower $E_{C.M.}$. Interestingly, ^{45}K has an even larger cross-section than ^{47}K despite having two fewer neutrons. Without consideration of shell effects one might expect that fewer neutrons should result in a weaker attractive potential and consequently a diminished fusion cross-section. The excitation function for ^{41}K + ^{16}O is not shown in this figure for clarity.
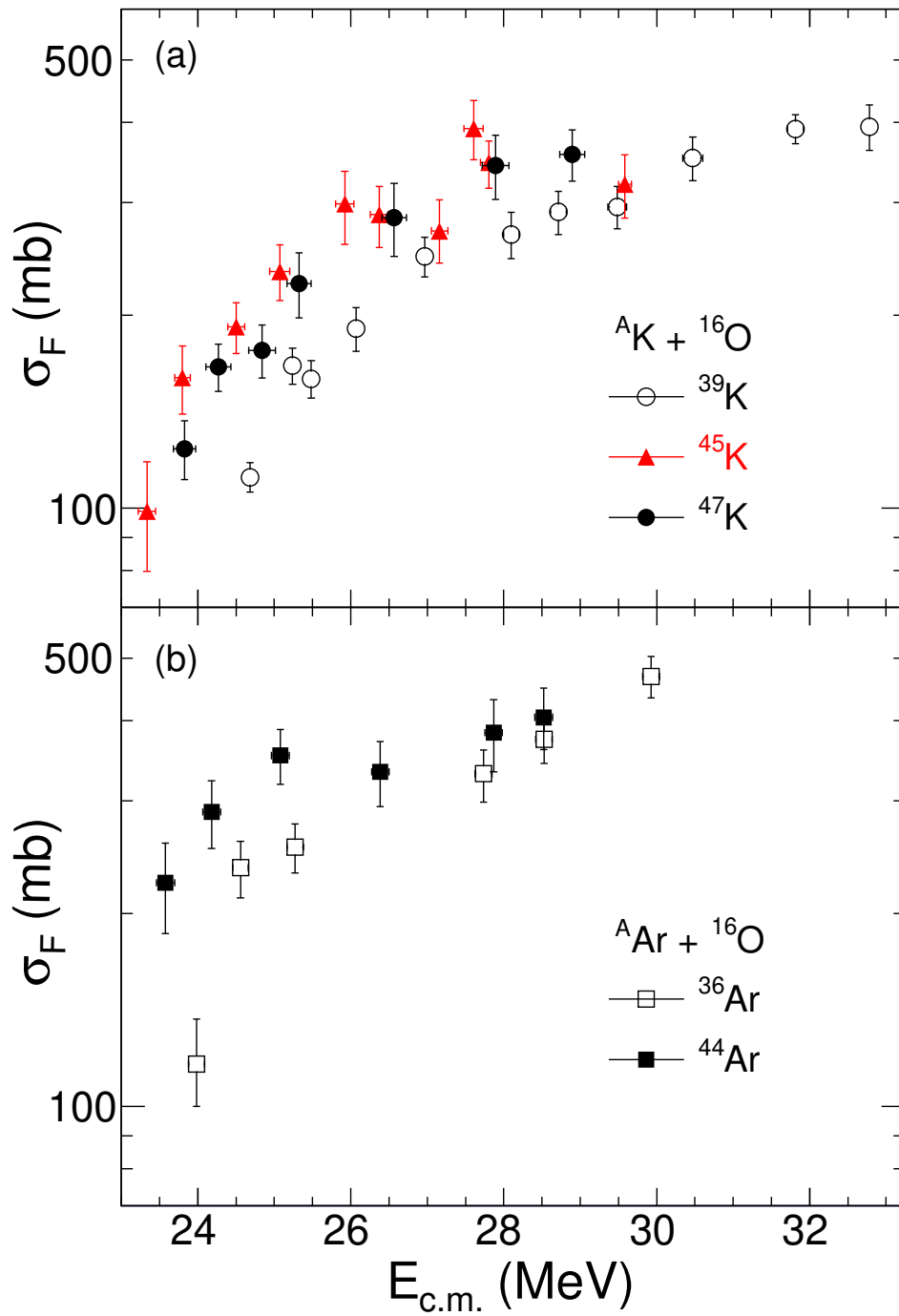
FIGURE 4.2: Comparison of the fusion excitation functions for ^{39,45,47}K$+^{16}$O (upper panel) and ^{36,44}Ar$+^{16}$O (lower panel).

43
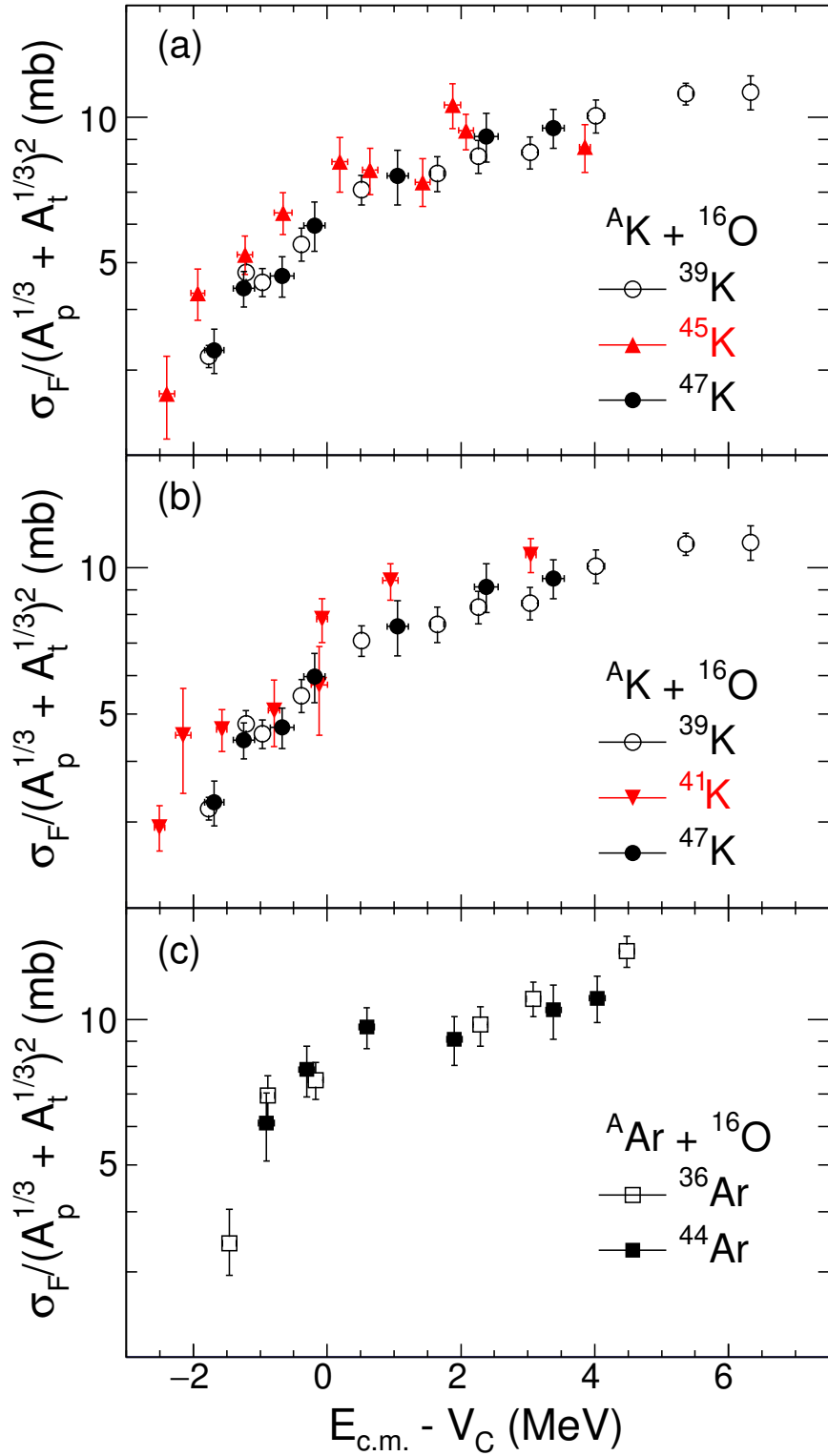
FIGURE 4.3: Comparison of the reduced fusion excitation functions for ^{39,41,45,47}K and ^{36,44}Ar on a ^{16}O target.

In Figure 4.2b the fusion excitation functions for ^{36,44}Ar are examined. This comparison also involves a difference of eight neutrons, as in the case of ^{39,47}K, but does not involve the closed shells of N=20 and N=28. For $E_{C.M.} < 26$ MeV the neutron-rich ^{44}Ar exhibits a larger cross-section. For $E_{C.M.} > 26$ MeV however the cross-section is essentially the same for ^{44}Ar and ^{36}Ar.

An effective means of comparing the fusion excitation function for different systems is the use of the reduced excitation function [111]. To calculate the reduced excitation function the fusion cross-section σ_F has been scaled by the quantity $(A_P^{1/3} + A_T^{1/3})^2$ and its dependence on the incident energy is examined relative to the Coulomb barrier. The Coulomb barrier, V_C, is taken as $V_C=1.44Z_PZ_T/(1.4(A_P^{1/3} + A_T^{1/3}))$. This scaling accounts for the systematic size and Coulomb barrier effects expected. This simple accounting of the Coulomb barrier does not include dependence of the charge radii on neutron number for the potassium isotopes recently reported [112]. Use of the simple prescription suffices as significant interpenetration of the charge distribution would be required for the impact of changes in the charge distribution to be manifested. The reduced excitation functions are compared in Figure 4.3.

When compared in this manner, ^{39}K and ^{47}K with their closed N=20 and N=28 shells exhibit essentially the same reduced fusion cross-section. This indicates that the increased cross-section for ^{47}K as compared to ^{39}K is effectively due to the larger ground-state size of the ^{47}K nucleus. In contrast to this result, a larger reduced fusion cross-section is evident for fusion of the open-shell ^{45}K (N=26). Thus, the systematic $A^{1/3}$ increase in size does not explain the ^{45}K fusion cross-section. It is interesting to note that this increased cross-section occurs close to and below the barrier. For $0 \leq (E_{C.M.}-V_C) \leq 2$ MeV, one observes a suppression in the reduced fusion cross-section. Similar structure in fusion excitation functions has been associated with resonance behavior in lighter systems [113]. The highest energy point for ^{45}K is consistent with the reduced cross-section of ^{39}K and

^{47}K, well below the expectation based upon extrapolation of the reduced cross-section from lower energies.

The reduced excitation function for ^{41}K is compared with those of the closed-shell ^{39,47}K nuclei in Figure 4.3b. As in the case of ^{45}K, the reduced fusion excitation function for ^{41}K is larger than that of the closed-shell nuclei. Remarkably, the presence of just two neutrons beyond the closed N=20 shell is sufficient to cause this increase.

In Figure 4.3c the reduced fusion excitation functions for ^{36}Ar and ^{44}Ar are presented. For these nuclei the reduced excitation functions are essentially the same within the measurement uncertainties. The similarity of the reduced excitation functions for ^{39}K and ^{47}K, two closed-shell nuclei, or ^{36}Ar and ^{44}Ar, two open-shell nuclei, demonstrates the effectiveness of the reduced excitation function in accounting for the systematic size effect on fusion due to addition of neutrons in an isotopic chain. The difference observed in the reduced excitation function for ^{41}K and ^{45}K in comparing an open-shell with two closed-shell nuclei is therefore significant. It is essential to note that this comparison is valid when none of the analyzed isotopes exhibit large collectivity. Although some of the nuclei presented are neutron-rich, they are not weakly-bound nuclei. Consequently, the fusion cross-sections should not be significantly affected by either breakup or collectivity of these nuclei in the energy region investigated.

4.1.2 Comparison with systematic and DHB density distributions

The simplest description of fusion is through the interaction of the density distributions of the two interacting nuclei. If the interaction between the nuclei is non-adiabatic (i.e. described by the sudden approximation) it is sufficient to consider the ground-state density distributions. To investigate whether the observed fusion excitation functions can

be described by the interaction of the ground-state density distributions of the projectile and target nuclei, the São Paulo model was used.

As a first approach to describing the observed data the São Paulo potential systematic was used. The São Paulo potential systematic [50] is the potential associated with matter densities described by a two-parameter Fermi-Dirac distribution with radius $R_0 = (1.31A^{1/3} - 0.81)$ fm and matter diffuseness $a = 0.56$ fm. This systematic was derived from the available experimental data for the charge distributions extracted from electron scattering and DHB calculations for many nuclei. As such, it provides a general description in which structural effects have been averaged over. The SPP systematic was used for the real part of the optical potential with a Woods-Saxon form used for the imaginary part with a depth of 50.0 MeV, reduced radius of 1.06 fm, and diffuseness of 0.20 fm for the one-channel calculations. Such a potential has been used in many CC calculations and their results successfully compare with experimental data [114, 115, 116, 116, 117].

Presented in Figure 4.4 (dashed lines) are the predicted matter density distributions for the K and Ar isotopes, using the SPP systematic. All these distributions have a smooth Fermi-Dirac shape with a central density of $\sim$0.16 nucleons/fm^3. These smooth distributions reflect, in essence, the one-body mean-field nature of the nuclei considered and do not manifest nuclear structure associated with two-body correlations.

To calculate more accurate matter density distributions which include two-body correlations we performed DHB density calculations [53]. The correlations in the DHB calculations of the present work are limited to surface-pairing correlations. These correlations can make subtle modifications to the nuclear surface, extending and modifying the nuclear density. The details of these mean-field calculations using an axially-symmetric self-consistent approximation are reported in Ref. [118]. The resulting matter distributions are shown in Figure 4.4 as the solid lines. Evident in the DHB matter distributions

is a double-humped structure, a manifestation of the shell structure. For ^{39}K the dominant peak is located at lower values of R. With increasing neutron number the density of this inner peak decreases until at ^{47}K the outer peak is the dominant peak in density. A similar trend is observed between ^{36}Ar and ^{44}Ar although for these nuclei the inner peak remains the larger peak. As the fusion of two nuclei is typically viewed as sensitive to the tails of the matter distribution, an expanded view of this region is shown in the insets of Figure 4.4. It is noteworthy that the tails of the matter distributions are quite similar although the DHB distributions are *slightly* less extended than the systematics.

Displayed in Figure 4.5 are the proton and neutron density distributions predicted by the DHB model. One observes that addition of neutrons to ^{39}K influences not only the neutron but also significantly impacts the proton density distribution. As the peak in neutron density situated at large R increases in magnitude, the proton peak situated at large R also increases in magnitude. As the total number of protons is constant, this increase is correlated with a decrease in the value of the central proton density. This outward displacement of the proton density by additional neutrons can be thought of as the resistance of nuclei to polarization of the ground state. This behavior has previously been noted in relativistic mean-field calculations for neutron-rich oxygen isotopes and reflects the n-p interaction via the strong force [119]. Close examination of this outward pull of the valence neutrons on the core (N≤20) neutrons as compared to the core protons reveals that the protons experience a larger outward pull. This difference can be interpreted as a repulsion between the valence neutrons and the core neutrons due to the Pauli exclusion principle. Similar behavior is also observed for the Ar isotopes.

Using the DHB matter distributions for both the projectile and ^{16}O target nuclei, the São Paulo Potential was generated and used to calculate the fusion cross-section. The theoretical predictions are compared with the experimental data in Figure 4.6. In addition to the cross-sections resulting from the DHB matter densities (solid lines) the
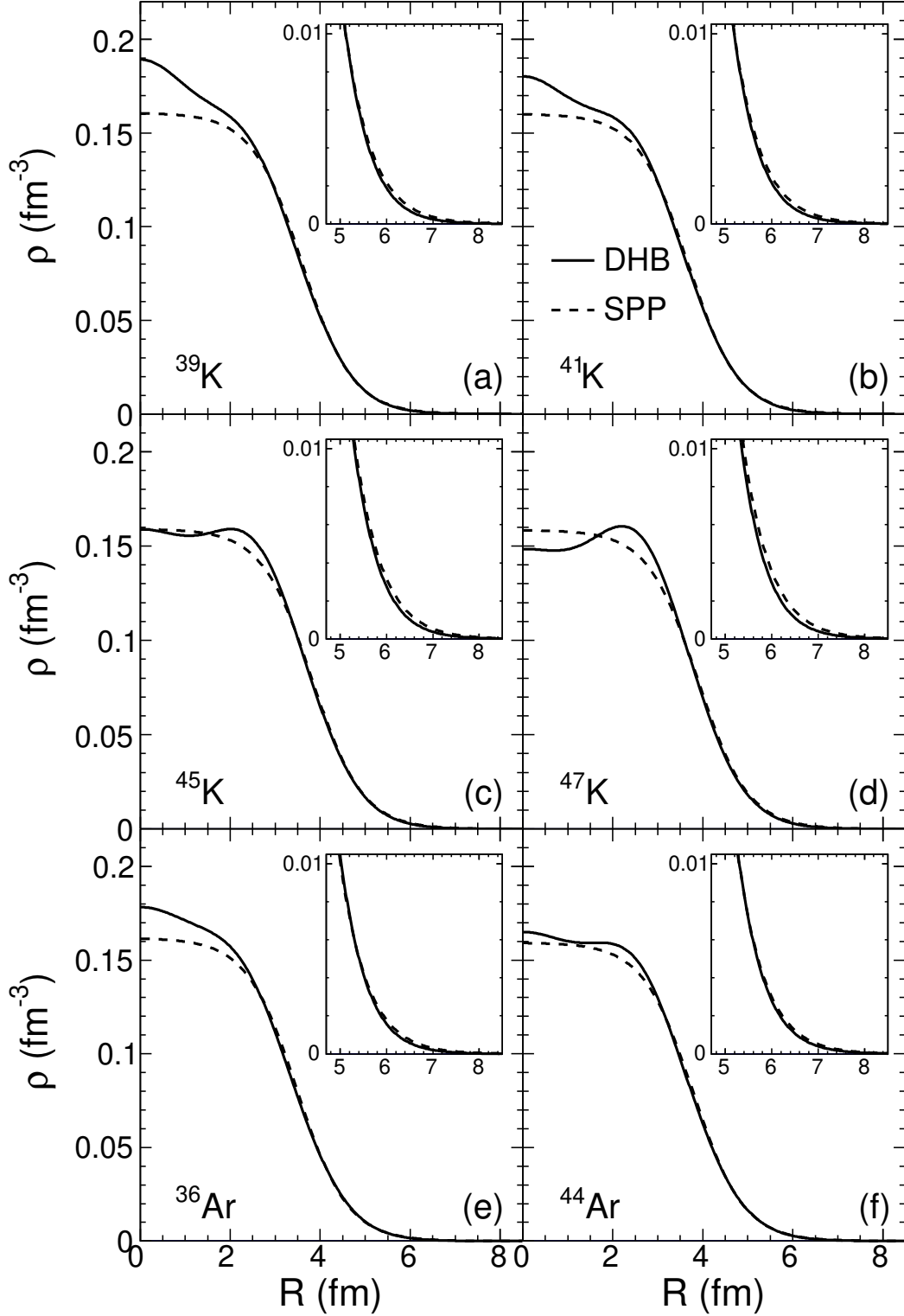
FIGURE 4.4: Comparison of the matter density distributions given by the systematics that is typically used within the São-Paulo fusion model with the density distributions predicted by Dirac Hartree Bogoliubov (DHB) calculations. Shown in the insets are the tails of the matter distributions.
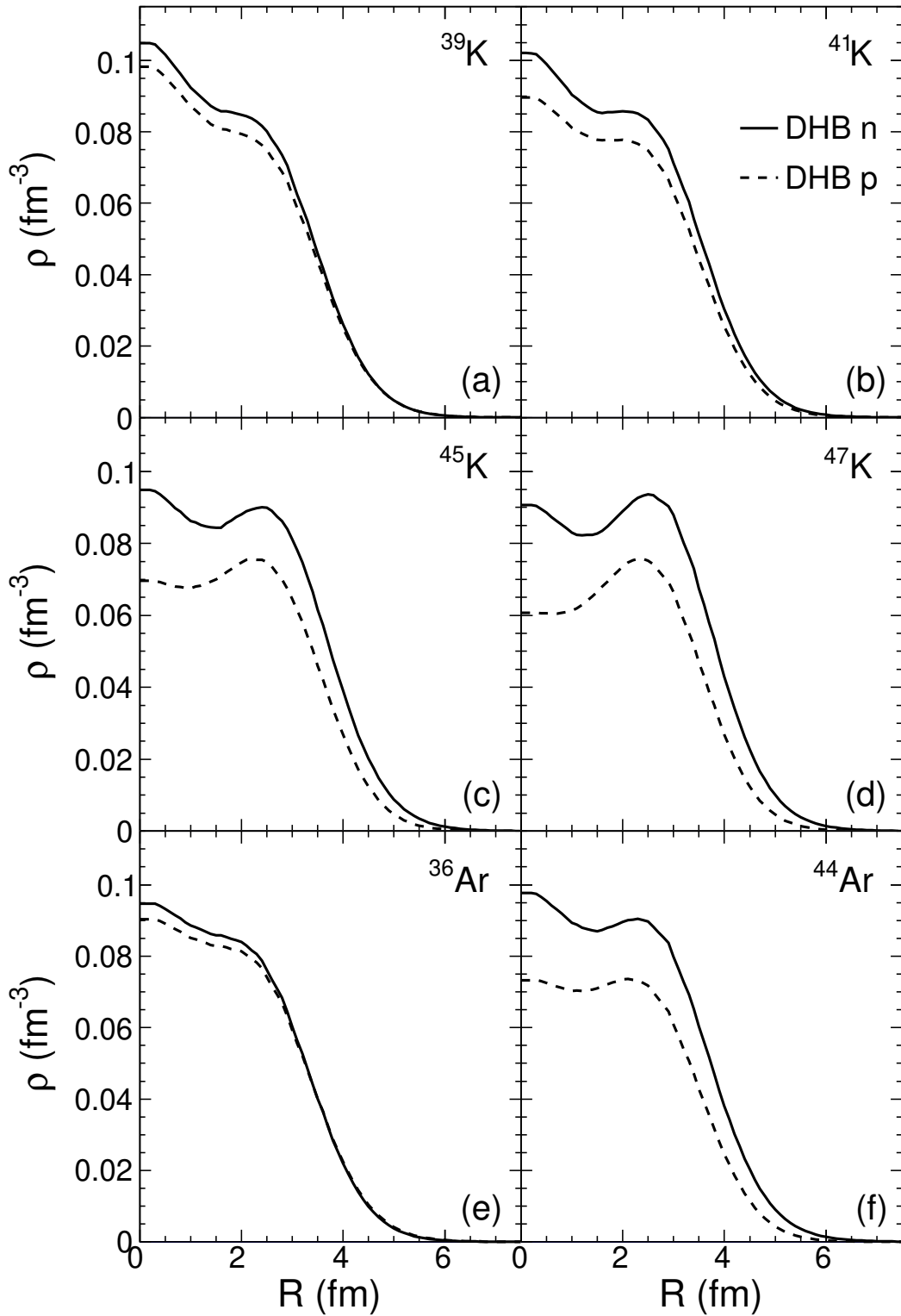
FIGURE 4.5: Density distributions of protons (dashed) and neutrons (solid) for K and Ar isotopes predicted by the DHB calculations.

cross-sections associated with the systematic densities are also shown (dashed lines). In all cases use of the DHB densities results in a significant reduction of the fusion cross-section as compared to the systematics. This reduction is apparent over the entire energy interval considered. The similarity of the tail of the density distribution for both the DHB and systematics suggests that the change in the cross-section is due to the difference in the interior part of the density distribution. Further theoretical work to reproduce these data are needed to confirm this conclusion.

Comparison of the theoretical predictions with the experimental excitation functions is revealing. For the open neutron-shell isotopes [41,45]K, the theoretical model with the DHB densities provides a reasonable prediction of the excitation function particularly for the lower energies. However, in the case of the closed neutron-shell [47]K and particularly for [39]K, the model overpredicts the measured cross-sections. This overprediction for the case of the closed-shell nuclei might suggest that the ground-state configurations at the saddle point that result in fusion are more compact than the ground-state DHB calculations indicate. Alternatively, it might signal that higher order correlations, not present in the DHB calculations are more important for these closed neutron-shell nuclei. In the case of the [36,44]Ar nuclei the agreement is intermediate between that of the open-shell and closed-shell K isotopes.

The fact that the São-Paulo fusion model using the DHB densities *overpredicts* the experimental data is also significant. Coupling to low-lying collective modes acts to increase the fusion cross-section. Given that the ground-state calculation already overpredicts the measured cross-section, the excitation of low-lying collective modes can be ruled out. The largest discrepancy is observed for the closed neutron-shells at N=20 and N=28. Presumably these closed-shell nuclei are the least likely to undergo collective excitations. The persistence of shell effects at the saddle point reflects the low intrinsic excitation of the saddle configuration.
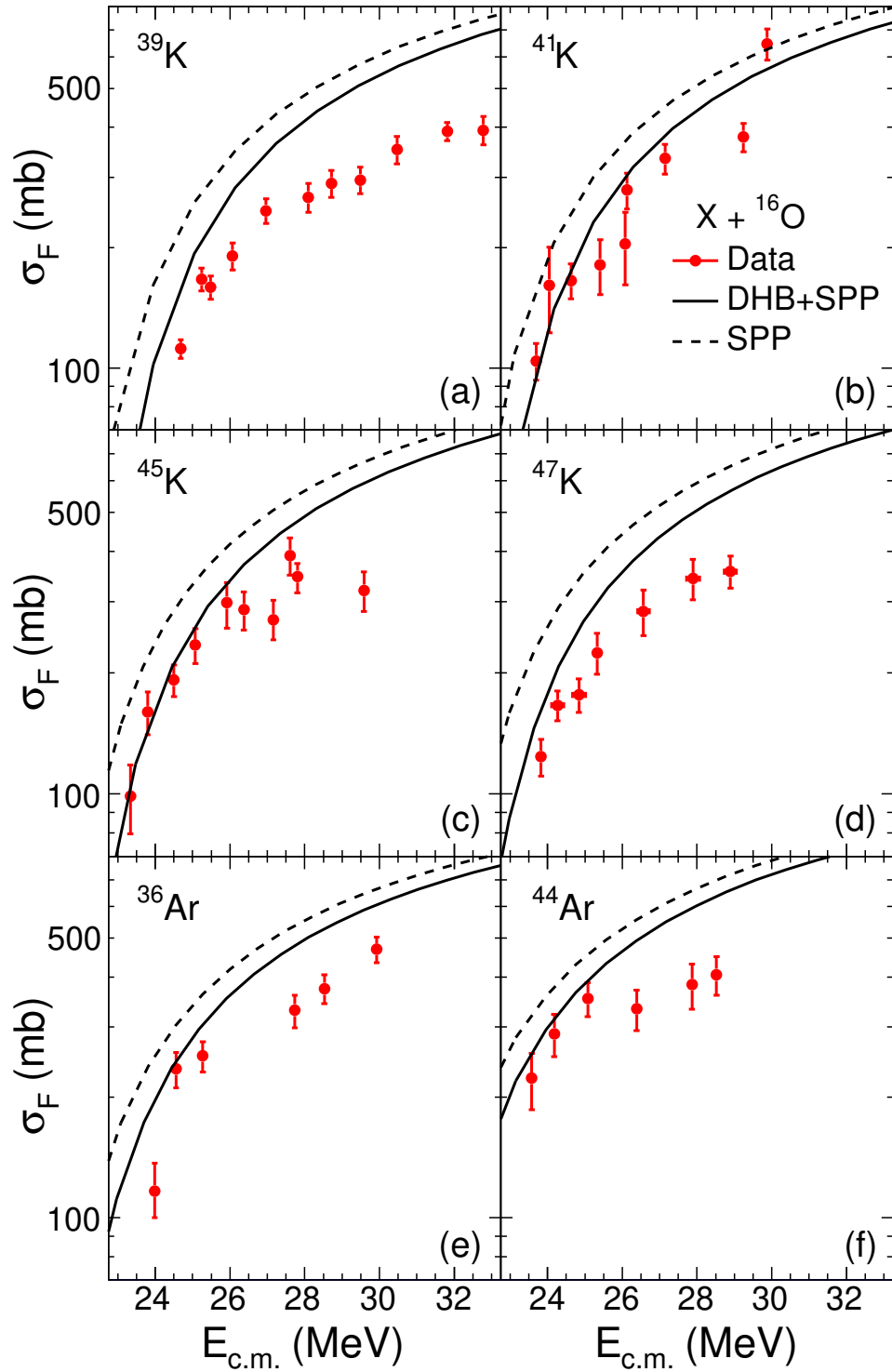
FIGURE 4.6: Comparison of the experimental cross-sections with the predictions of the São Paulo model using DHB densities as well as densities from systematics.

4.2 ^{36,44}Ar,^{39,41,45,47}K+^{28}Si

4.2.1 K,Ar + ^{28}Si excitation functions

The ^{16}O contamination of the ^{28}Si targets in E17002 did not prohibit the measurement of the cross-section on the intended target. Figure 4.7 presents the raw cross-sections for the measured nuclei on ^{28}Si. The excitation functions for ^{41,45}K (measured in E17002) are shown in Figure 4.7a alongside the previously measured excitation functions of ^{39,47}K. At energies above E$_{C.M.}$=40 MeV, the ^{41,45}K excitation functions overlap significantly with the excitation function for ^{47}K and are above the excitation function for ^{39}K. Even without accounting for size and barrier differences, this indicates an enhancement of the open-shell nuclei as compared to the closed-shell counterparts and matches the results from the reaction of these isotopes on an oxygen target. At center-of-mass energies below 40 MeV, the enhancement for ^{41,45}K increases even to cross-sections larger than those of ^{47}K. Figure 4.7b shows the raw excitation functions for ^{36,44}Ar with the excitation functions of ^{39,47}K shown for reference. A similar trend is observed as with the open-shell potassium nuclei. The argon isotopes show a small enhancement at higher energies with the enhancement increasing at energies below the Coulomb barrier. It is difficult to draw any stronger conclusions about the argon isotopes because of the difference in Coulomb barriers between argon and potassium.

To account for the differences in size and barrier for the various measured nuclei, the reduced excitation function was calculated. The reduced excitation function was created in the same method that was used for reaction on the oxygen in Section 4.1.1. Presented in Figure 4.8a are the reduced fusion excitation functions for ^{39,41,45,47}K + ^{28}Si. For all the systems shown, as expected, the reduced fusion cross-section largely converge at energies above the barrier. A small increase in the cross-section of ^{41}K is observed relative to the other isotopes at above barrier energies in alignment with the results seen

53
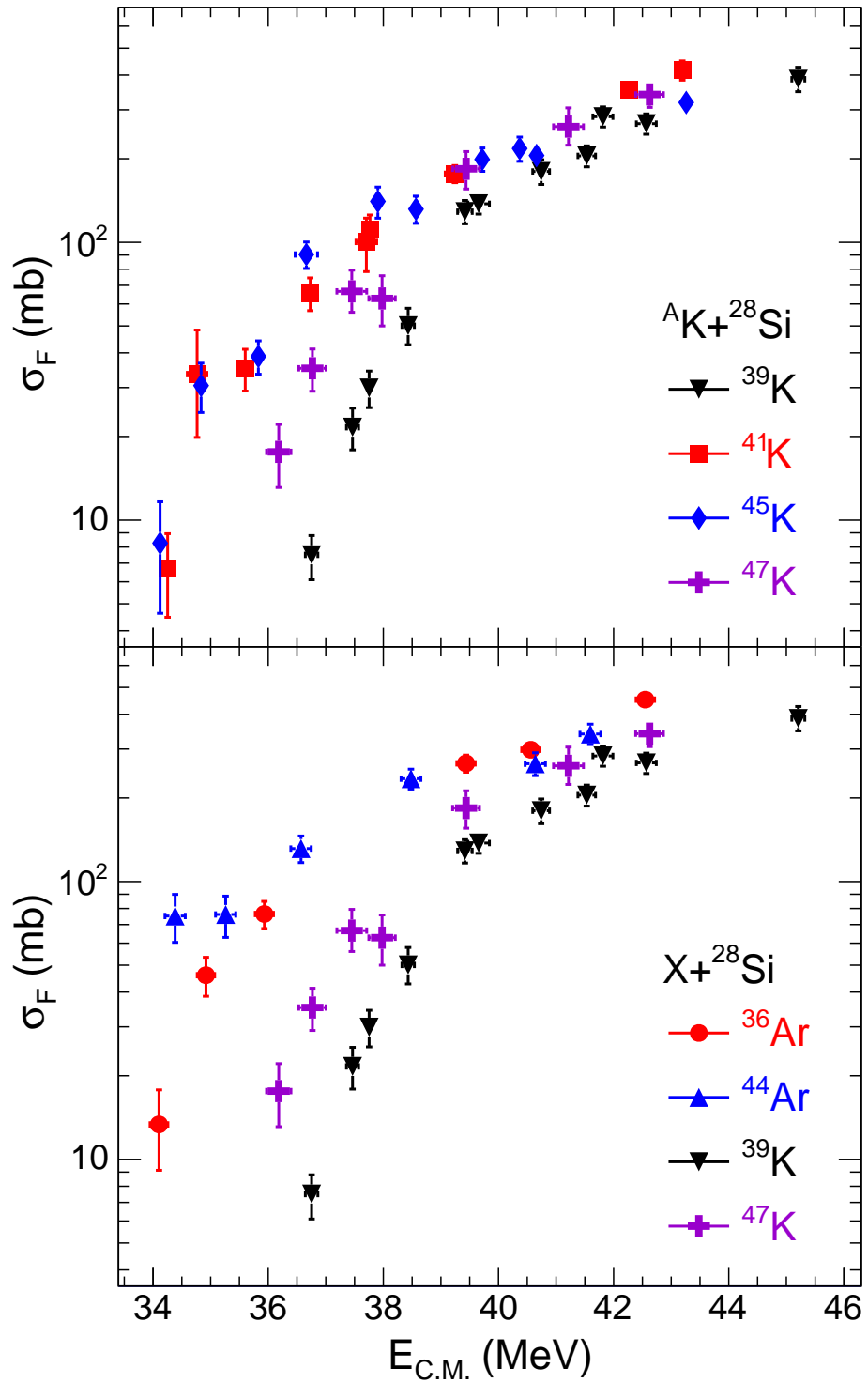
FIGURE 4.7: The measured fusion excitation functions for X+^{28}Si. The ^{39}K and ^{47}K excitation functions are provided as reference in both panel (a) and panel (b).
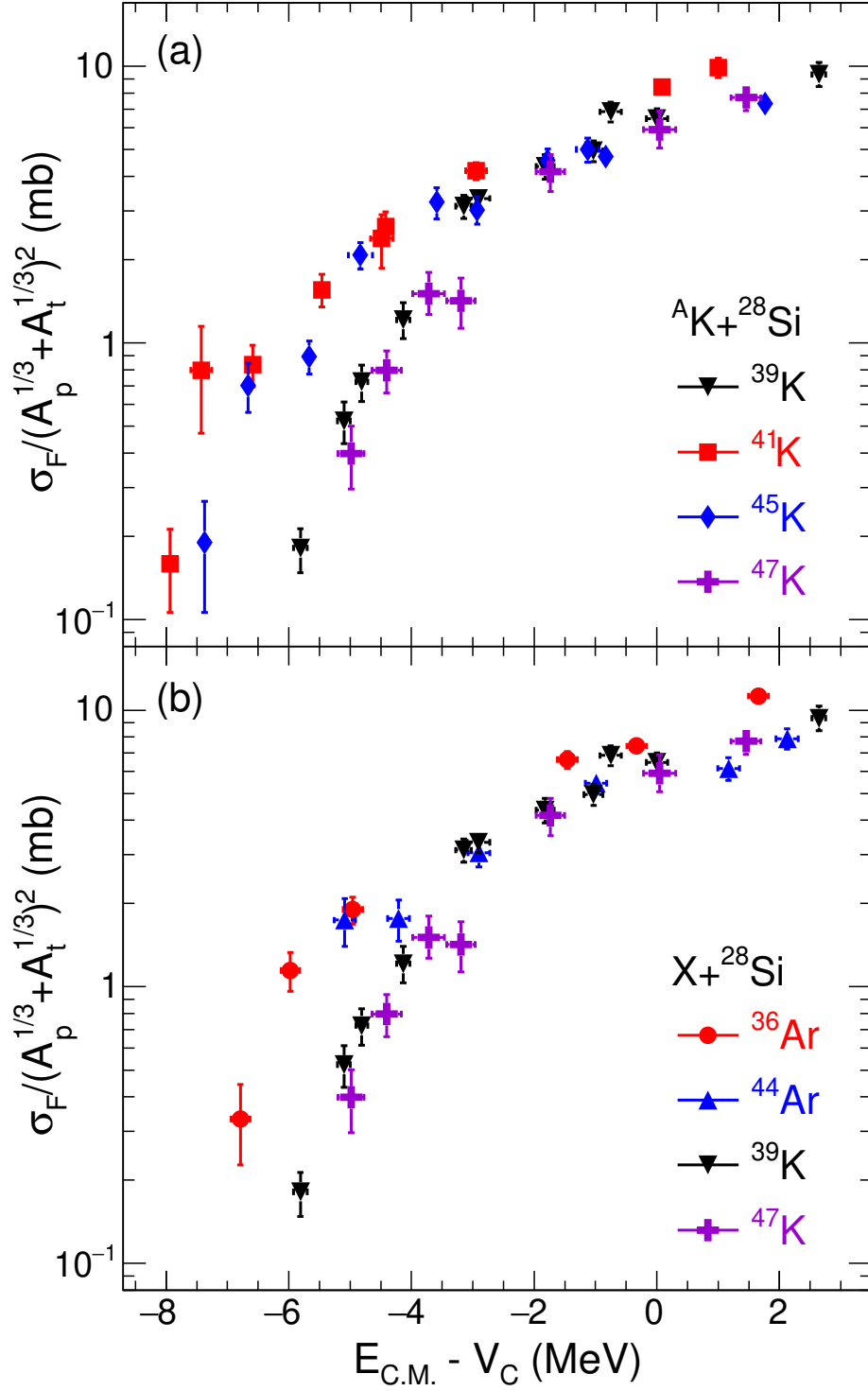
FIGURE 4.8: Comparison of the reduced fusion excitation functions for X+^{28}Si. The ^{39}K and ^{47}K excitation functions are provided as reference in both panel (a) and panel (b).

for reaction on oxygen. Below the barrier however, significant differences are apparent between the different systems. At sub-barrier energies the data clearly organizes itself into two groups: one associated with ^{39}K and ^{47}K (closed neutron-shells) and the other with ^{41}K and ^{45}K (open neutron-shells). The ^{39}K and ^{47}K projectiles with their closed N=20 and N=28 shells respectively manifest essentially the same reduced fusion cross-section. This similarity of the reduced fusion cross-section indicates that the density distributions, relevant to fusion, for the two closed-shell K isotopes are similar when scaled by $A^{1/3}$. In contrast to this result, a larger reduced fusion cross-section is evident for fusion of the open-shell ^{41}K (N=22) and ^{45}K (N=26). This increase is independent of the systematic $A^{1/3}$ increase in size. The same enhancement at sub-barrier energies is observed for the open-shell ^{36,44}Ar nuclei as compared to the closed-shell K isotopes in Figure 4.8b. It is interesting to note that this difference in cross-section increases as one goes below the barrier. This result suggests that the tail of the neutron density distribution for the open-shell nuclei differs from that of the closed-shell nuclei at the saddle point.

Presented in Figure 4.9 are the reduced fusion excitation functions grouped by their proximity to the N=20 and N=28 shells. In Figure 4.9a one observes that both ^{36}Ar and ^{41}K exhibit similar excitation functions with a marked enhancement of the reduced fusion cross-section as compared to the closed-shell ^{39}K (N=20). Apparently, the presence of two holes below the closed-shell (^{36}Ar) is effectively the same as the presence of two particles above the closed-shell (^{41}K) in determining the reduced fusion cross-section. A similar enhancement in the reduced fusion cross-section is observed at the N=28 shell for the presence of two holes with ^{44}Ar and ^{45}K as compared to ^{47}K. The agreement between the open-shell argon and potassium nuclei around both the N=20 (^{36}Ar and ^{41}K) and N=28 (^{44}Ar and ^{45}K) seems to indicate that the unpaired proton in potassium has little effect on fusion in the measured energy range.
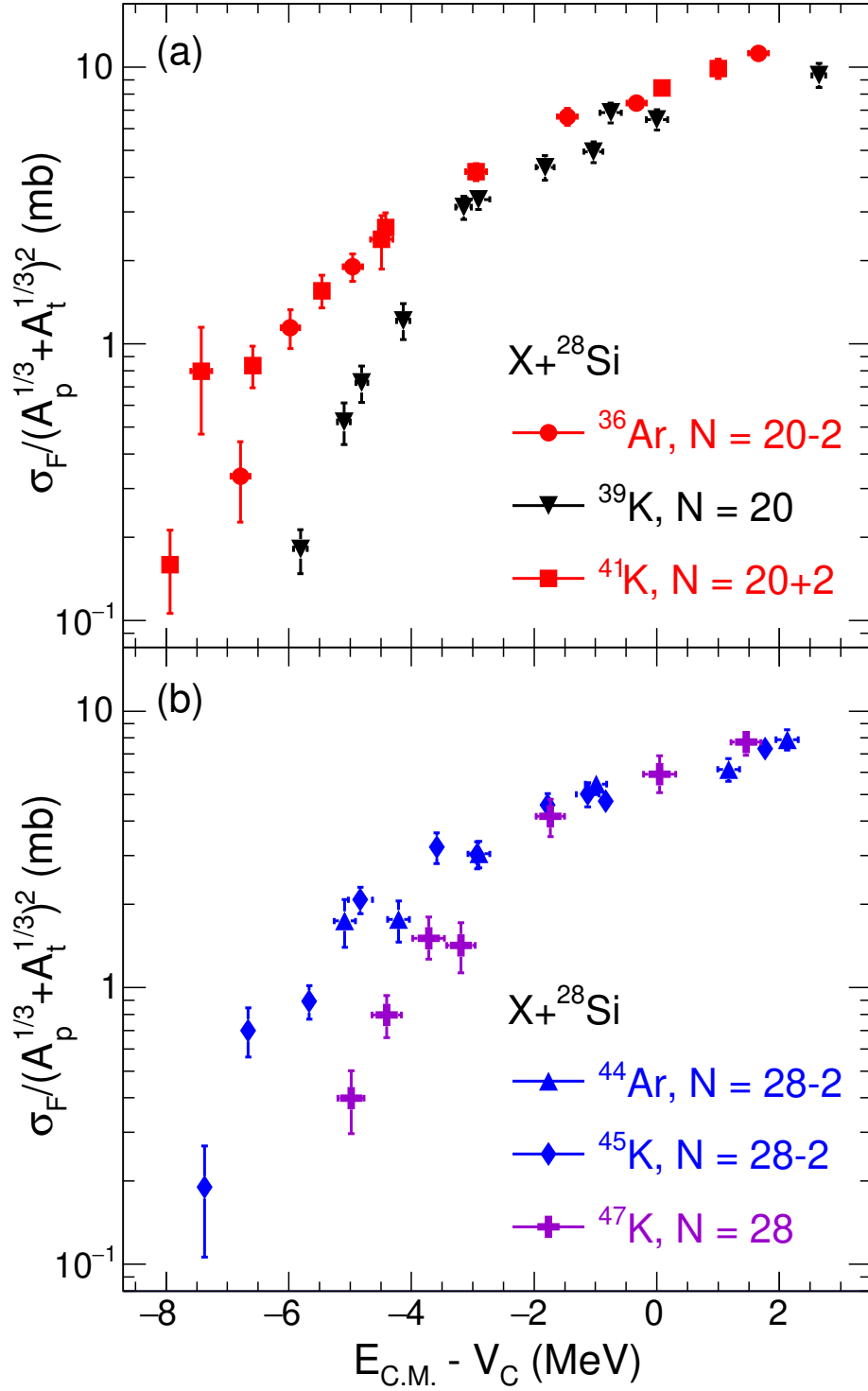
FIGURE 4.9: Reduced excitation functions for the measured systems. Panel (a) shows the systems closest to the N=20 shell closure. Panel (b) shows the systems closest to the N=28 shell closure.

4.2.2 Comparison of reaction on ^{16}O vs ^{28}Si

Use of the reduced excitation functions allows for direct comparison of the excitation functions of ^{39,41,45,47}K and ^{36,44}Ar on ^{16}O and ^{28}Si targets. The dependence of the reduced cross-section on the above-barrier energy, $E_{C.M.}$-V_C, is shown in Figure 4.10. In contrast to the O target which probes essentially the above-barrier regime, the Si target enables examination of the regime from just above to below the barrier. In the energy interval probed by both targets, -2 MeV $\leq E_{C.M.}$-$V_C \leq$ 2 MeV, the excitation functions are in reasonable agreement. Particularly at energies above the Coulomb barrier, the two sets of excitation functions are almost entirely overlapping. For the lowest measured oxygen energies a slight dip in the X+^{16}O excitation functions can be observed. This is most notable for ^{36}Ar. This decrease in cross-section at below-barrier energies could be caused by the increased binding of the closed proton (Z=8) and neutron (N=8) shells of ^{16}O. As is observed for the below-barrier measurements on ^{28}Si, fusion with a closed-shell projectile (^{39,47}K) is significantly suppressed relative to open-shell projectiles (^{41,45}K). It is reasonable to believe that the same is true for closed-shell and open-shell targets. However, this dip is only observed in the lowest energy point of the oxygen excitation function and any stronger conclusion about a deviation between the oxygen and silicon excitation functions would require measurement of the fusion cross-sections at lower energies.

The agreement of the reduced excitation functions above the barrier shows that the difference between the oxygen and silicon targets is appropriately accounted for by scaling for the system size and Coulomb difference. The complementary nature of the measurement with the two targets is important as the above-barrier region is primarily sensitive to the effective size of the fusing system while the sub-barrier cross-section is sensitive to the height of the effective fusion barrier and its penetrability (thickness). An increasing number of neutrons along an isotopic chain should result in an extended neutron density distribution and consequently an increased attractive potential with little

58
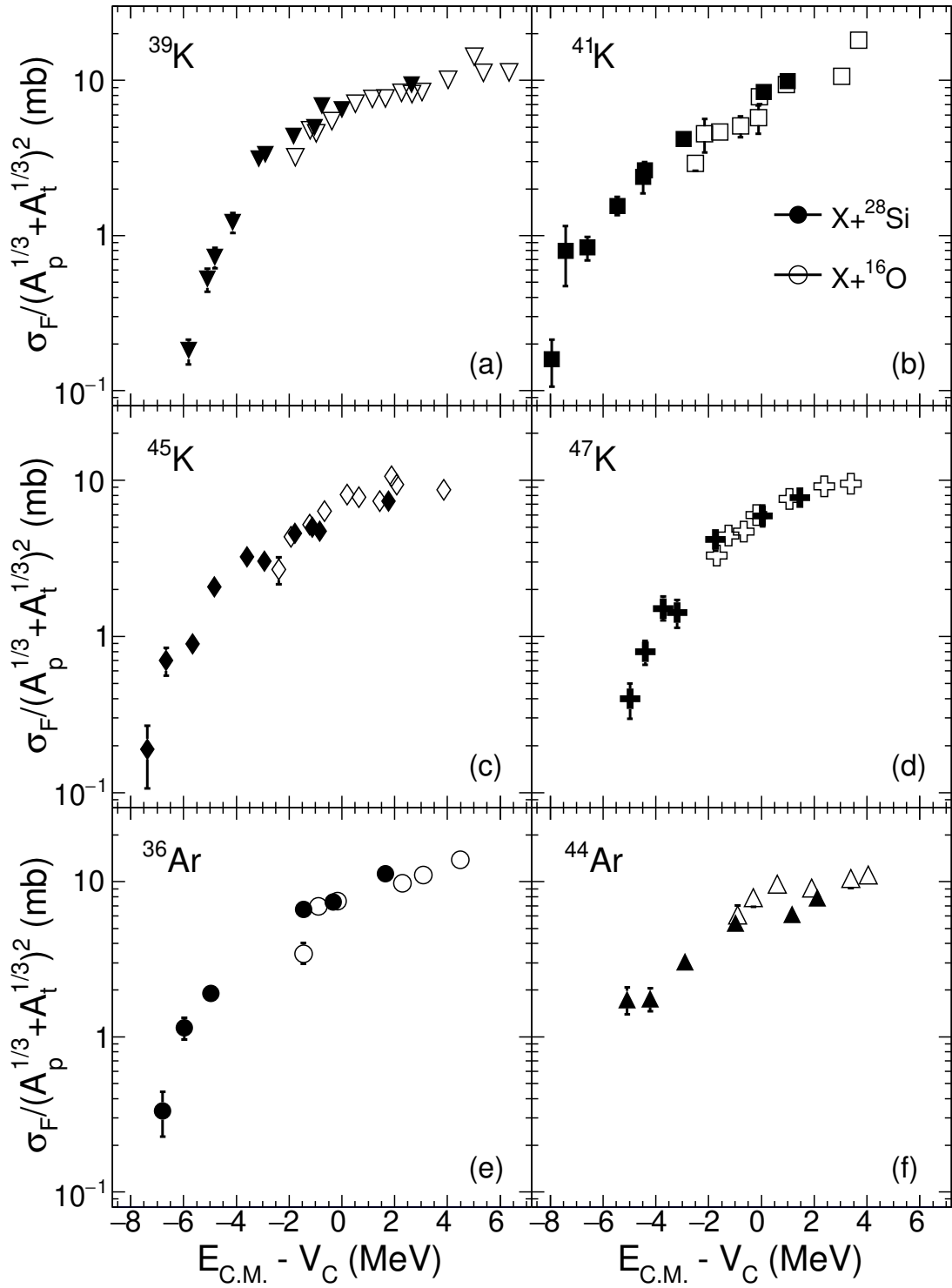
FIGURE 4.10: Dependence of the reduced excitation function on the above-barrier energy, $E_{C.M.}\text{-}V_C$, for both ^{16}O and ^{28}Si targets.

change to the repulsive Coulomb potential [51]. This increased attractive potential should result in a reduction of the fusion barrier and consequently an increase in the near- and sub-barrier fusion cross-section.

4.2.3 Comparison with static and dynamic calculations

To investigate whether the observed fusion excitation functions can be described by the interaction of the density distributions of the projectile and target nuclei, the São Paulo model was used to calculate the fusion excitation functions. The calculations for reaction on an oxygen target (Section 4.1.2) demonstrated the sensitivity of the fusion cross-section to accurate ground-state density distributions. As such, the same DHB calculations [53] were performed which provide reasonably accurate matter density distributions including two-body correlations.

Using the ground-state DHB matter distributions for both the projectile and ^{28}Si target nuclei, the São Paulo Potential was generated and used to calculate the fusion cross-section. These theoretical predictions are represented by the dashed lines and labeled 'DHB-OC' in Figure 4.11. Comparison of the theoretical predictions with the experimental excitation functions is revealing. For the closed neutron-shell isotopes ^{39,47}K, the DHB-OC (ground-state) calculations provide a reasonable prediction of the excitation function over the entire energy interval measured, although the theory lies slightly below the experimental data particularly in the sub-barrier regime. However, in the case of the open neutron-shell ^{41}K and ^{45}K and ^{36}Ar, the model dramatically under-predicts the measured cross-sections. This under-prediction for the case of the open-shell nuclei suggests that the ground-state configurations alone are insufficient in describing the measured cross-sections. In the case of ^{44}Ar insufficient data exists at low energy to draw a definitive conclusion.
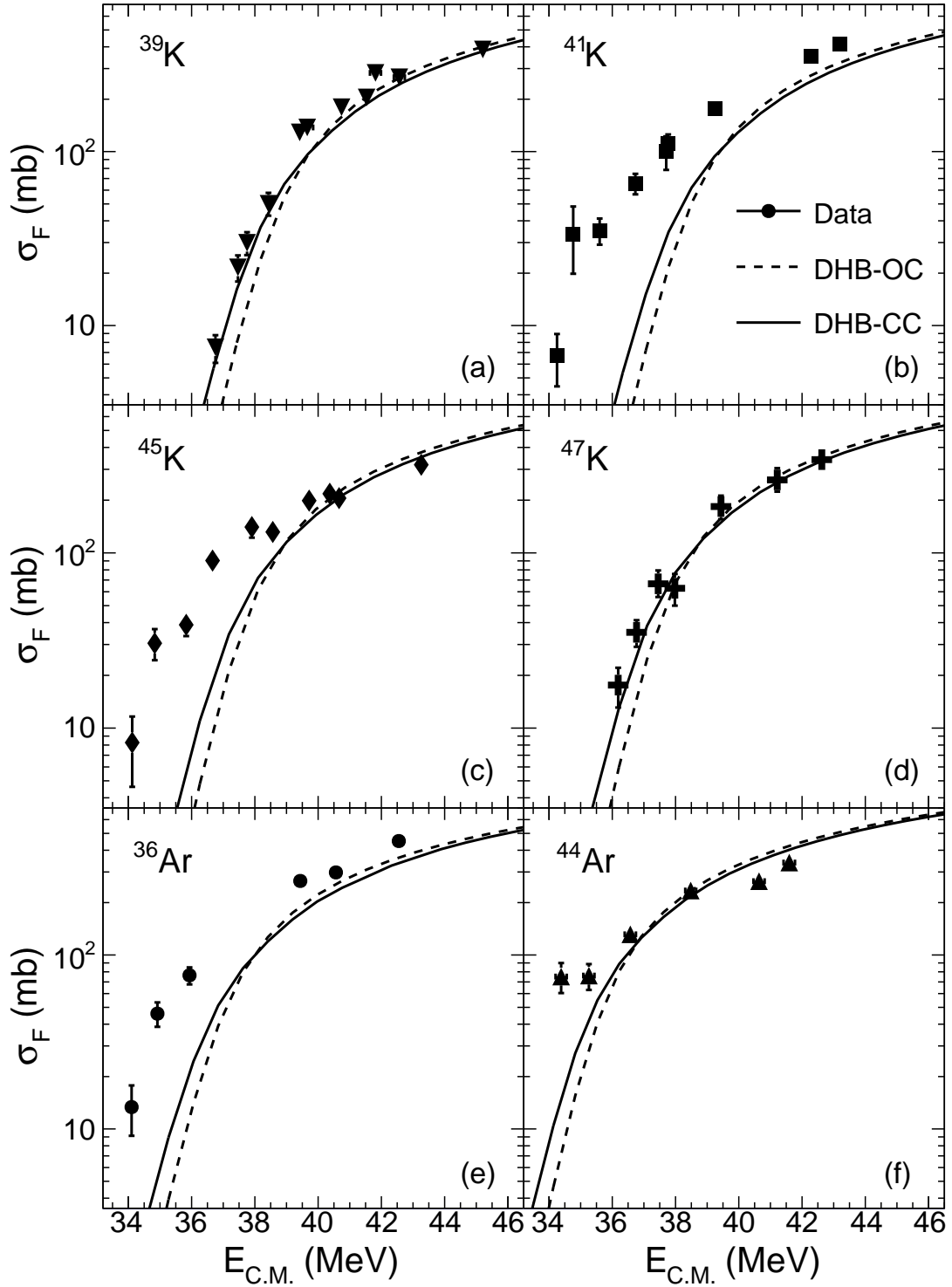
FIGURE 4.11: Comparison of the experimental cross-sections with the predictions of the São Paulo model using DHB densities. Both One-Channel (DHB-OC) and Coupled-Channel (DHB-CC) calculations were considered.

In an attempt to improve the calculations, excited states were included using coupled-channels. As coupling to low-lying collective modes acts to increase the fusion cross-section [120, 121, 122], coupled-channels calculations were performed to investigate the extent to which the presence of low-lying states increases the fusion cross-section. The 1.779 MeV, 2^+ and 4.618 MeV, 4^+ first states of the target were considered. The coupling to the low-lying projectiles states did not produce a considerable effect on the fusion cross section. To account for the couplings between the low-lying states the transition probabilities were taken from Ref. [123].

The results of the CC calculations are shown in Figure 4.11 as solid lines labeled 'DHB-CC'. In the case of the closed-shell nuclei (^{39}K and ^{47}K), inclusion of the excitations considered provides a good description of the fusion cross-section. For these nuclei the DHB-CC calculations improve upon the DHB-OC calculations below the barrier and provide a good description of the data. However, in the case of the open-shell nuclei the experimental data are significantly enhanced relative to the CC calculations. It is particularly interesting to note that the magnitude of the enhancement is much larger than the increase due to the inclusion of inelastic excitation in the CC calculations. A more thorough theoretical description is necessary in order to explain the observed excitation functions.

Chapter 5

Target foil production and characterization

5.1 Need for isotopically-enriched ^{28}Si target foils

The Indiana University fusion group has successfully measured the fusion excitation function for multiple beams and targets using an ETOF approach [4, 5, 79]. During the measurement of ^{39,47}K + ^{28}Si, oxygen present in the silicon target provided a source of background for the identification of the fusion ERs. Fusion of projectile nuclei with oxygen resulted in fusion products that needed to be distinguished from the products resulting from fusion of projectile nuclei with silicon. The presence of fusion ERs from reaction on contaminant ^{16}O in the target is clearly seen in Figure 5.1 as a second fusion ER island. Although the fusion products from the two reactions are separable, the need to separate the contaminant residues from the residues of interest introduces a background to the measurement of the intended experimental fusion cross-section. Within this thesis it has been shown that the cross-section from fusion of the beam on the contaminant oxygen is able to be extracted independently and with minimal interference to the cross-section from fusion on silicon. While this resulted in a valuable measurement, the oxygen which was present during both E15505 (^{39,47}K + ^{28}Si) and E17002 (^{41,45}K/^{36,44}Ar + ^{28}Si) could be a major source of error in future experiments. In particular, a larger fraction of oxygen in the target or a shorter time-of-flight in the ETOF experimental setup could cause the contaminant to interfere with the intended measurement. Consequently, production of isotopically-enriched ^{28}Si targets was designated a high priority for future experiments.

Several techniques have been previously used to fabricate silicon targets [124, 125]. To produce silicon foils with minimal oxygen contamination the vapor deposition approach

63
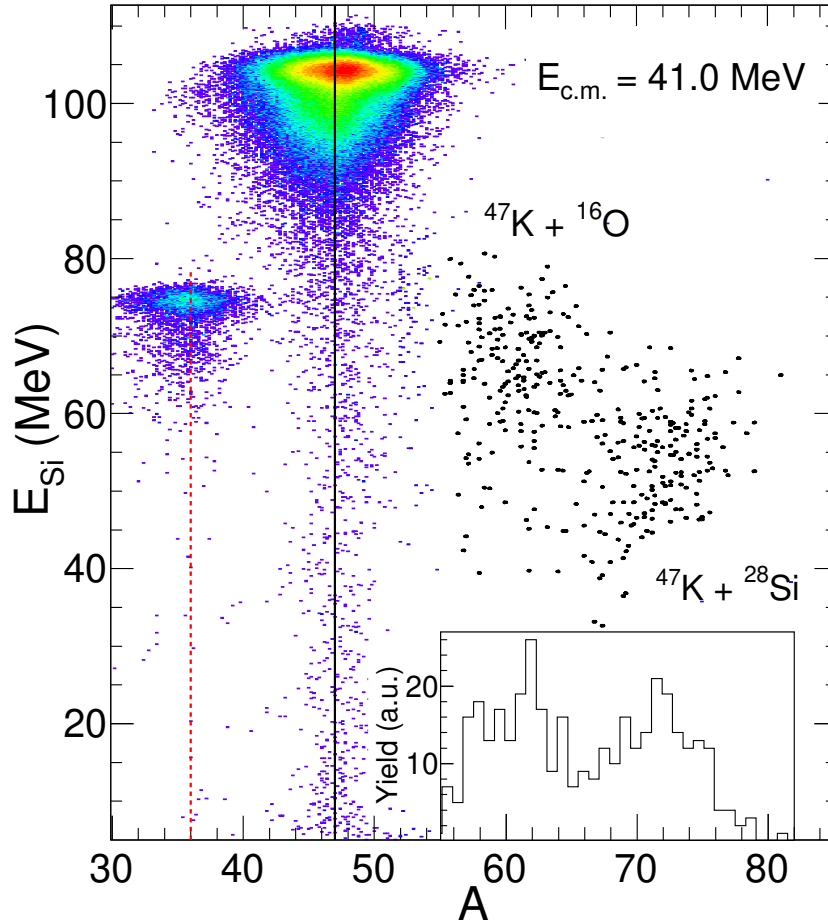
FIGURE 5.1: An EA spectrum taken from [4]. The two largest features are the scattering lines from the ^{47}K beam and the ^{36}Ar beam contaminant. Two clear ER islands are visible to masses higher than the ^{47}K scatter line - one from fusion on the intended ^{28}Si target and one from fusion on contaminant ^{16}O in the target.

[124] was employed. Following construction of an electron beam (e-beam) vapor deposition system, the device was commissioned and the evaporation procedure was optimized using ^{nat}Si. Subsequently, isotopically-enriched ^{28}Si foils intended for upcoming fusion experiments were produced. Several independent measurements were used to characterize the foils. Foil thickness was determined by using α-particle energy loss measurements through the foils (α-gauge), as well as Rutherford backscattering (RBS) measurements. In order to assess the elemental purity of the foils, both RBS and X-ray photoelectron spectroscopy (XPS) were utilized. Characterization of the foils using the above techniques

64

showed them to consist of 87-90% silicon with an effective thickness of $\sim$220 μg/cm^2. Details of the e-beam vapor deposition system constructed, its use in producing silicon targets, and the characterization of the targets produced are presented below.

5.2   Electron beam source and vacuum chamber

The constructed e-beam vapor deposition system uses the Ferrotec/Temescal Model 1CK Convertible Electron Beam Turret Source as its central element. This e-beam source is capable of providing a beam of up to 10 keV electrons with an emission current up to 1.5 A (10 kW maximum). For all evaporations described, the filament was operated at a maximum current setting of 300 mA. The electron beam produced by the filament is accelerated and deflected by 270° before striking the sample placed in a copper crucible. To separate the evaporant from the copper crucible a liner of either molybdenum or tantalum is typically used. The crucible has 4 pockets which allows vapor deposition of up to four materials without venting the vacuum chamber. Additionally, the electron beam source has the ability to sweep the electron beam in two dimensions in order to provide even heating of the material in the crucible liner. The copper crucible is water cooled using a Haskris WW2 water chiller which allows circulation of 20°C water at a rate of 2.75 gpm.

Successful production of silicon foils with reduced oxygen content requires achieving a good vacuum (P $\sim$ 10^{-7} Torr) in the evaporation chamber prior to commencing the evaporation. In order to accomplish this, a stainless steel chamber was re-purposed to house the electron beam evaporation assembly as shown in Figure 5.2. Moreover, to provide a clean environment and facilitate attainment of a good vaccum, the chamber was professionally electropolished [126]. The chamber is pumped using an Edwards STP-603 turbomolecular pump (650 l/s N$_2$) backed by a Edwards nxDS15i scroll pump to maintain an oil-free environment. Following evacuation to P < 5 x 10^{-5} Torr, a CTI-8 cryopump
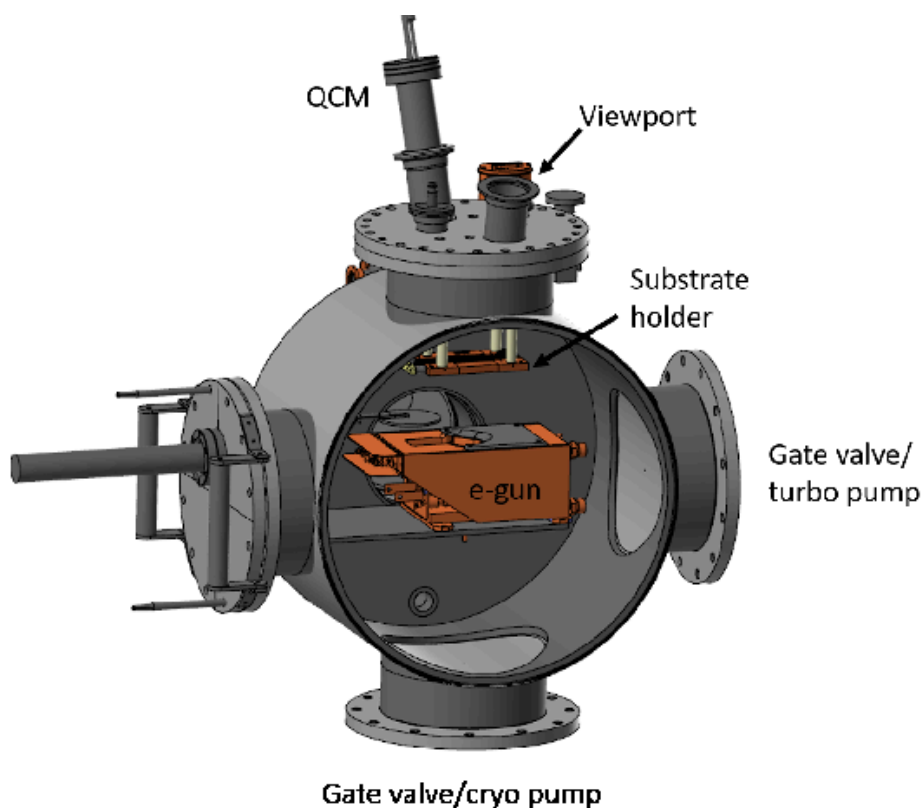
FIGURE 5.2: CAD drawing of the chamber housing the vapor deposition system. The large side flange used as the main access to the chamber is omitted.

(1500 l/s air) is used to further reduce the chamber pressure. During evaporation, to protect the turbopump from evaporated material, the gate valve at its entrance is closed and pumping is maintained using only the cryopump. The optimal base vacuum of the chamber is achieved by using a bake-out procedure which involved heating the chamber up to 130°C at vacuum for up to 72 hours. With baking, a pressure of 1.5×10^{-7} Torr is attained. The residual gas in the chamber following bake-out was assessed using a Stanford Research Systems RGA 200. The spectrum from the RGA is presented in Figure 5.3. The majority of the gas remaining in the chamber is hydrogen, carbon dioxide, water vapor, and nitrogen. The small peak at mass = 32 corresponds to oxygen and represents a partial pressure of approximately 1×10^{-9} Torr. Based upon the chamber total pressure, this corresponds to approximately 1% oxygen content in the residual chamber gas.

66
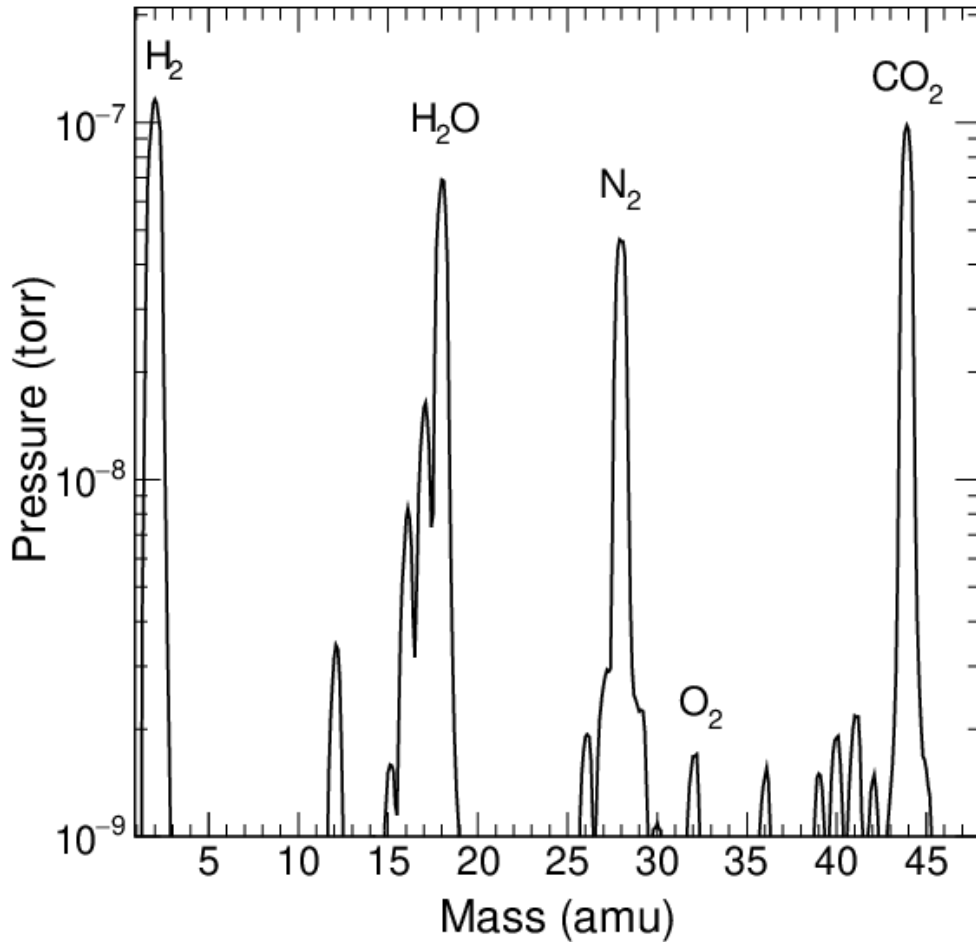
FIGURE 5.3: Mass spectrum of the residual gas in the evaporation chamber following bake-out.

The electron gun is mounted on an ISO200 flange facilitating its removal from the chamber if necessary. Mounted on the same flange as the electron gun is a stainless steel shutter. This shutter prevents deposition of evaporated material from the crucible during initial heating of the material. The shutter is operated from outside the chamber by manipulating a linear-motion vacuum feedthrough (Huntington L-2212-6). Access to the interior of the chamber is provided through the large side flange. This access is essential to mount and dismount the target substrate, clean the inside of the chamber, and resupply material to the crucible after each evaporation. The top flange provides a viewport through which the motion of the electron beam in the crucible pocket can be

observed during evaporation. It also provides feedthroughs for a quartz crystal monitor (QCM) used to monitor the deposition rate during evaporation. Additional feedthroughs allow heating and temperature monitoring of the copper substrate holder.

Heating of the substrate during evaporation allows relaxation of stress in the deposited material. Reduction of stress improves the ability of the foil to be subsequently released from the substrate while maintaining its structural integrity. The substrate holder is suspended from the top flange of the chamber with ceramic standoffs to provide electrical and thermal isolation between the heating block and the chamber. This substrate holder is a copper block with 1/8 in. diameter cylindrical channels. Ceramic tubes placed in these channels provided electrical isolation for the tantalum wire (99.9%) [127] which serves as the resistive heating element. Threaded through the ceramic tubes is 13 in. of Ta wire (0.25 mm diameter) with a resistance of 5 ohms. Application of a voltage of 16 V across the wire by a Tekpower TP3005P Programmable Power Supply results in a current that heats the copper block. The temperature of the substrate holder is monitored using a thermocouple. Substrates are mechanically attached to the substrate holder using 2 copper straps which screw into the block.

5.3 Silicon foil production

5.3.1 Substrate preparation

Two different substrates were used to produce silicon foils. Initial attempts used tungsten substrates as tungsten had been reported as optimal for the production of silicon targets [124]. Selection of tungsten as a substrate was justified by the close match of its coefficient of linear expansion (4.5 μm°C^{-1}) as compared to that of silicon (3.0 μm°C^{-1}) [128]. The tungsten substrates used were 1.0 in. x 3.0 in. in area and 0.009 in. thick. Prior to their use, to reduce surface roughness the tungsten substrates were electropolished.

Parameters for electropolishing the tungsten substrates were adjusted from parameters used in electropolishing tungsten Scanning Tunneling Microscope (STM) probes [129]. Tungsten substrates were submerged in a 0.25 M NaOH solution and electropolished for 5 minutes at a current density of 13.5 A/dm^2. Two 2 in. x 4 in. stainless steel plates placed on either side of the substrate served as cathodes. After electropolishing, the substrates were cleaned using an Alconox detergent bath and subsequently rinsed with de-ionized water.

Following initial work with tungsten substrates, the use of copper substrates was investigated. Copper had also been reported in the literature as a successful substrate for production of silicon foils [125]. The copper substrates used were the same area as the tungsten substrates with a thickness of 0.012 inches. Prior to evaporation, the copper substrates were electropolished following well-established procedures [130]. The electropolishing solution consisted of a well-mixed, aqueous solution of 50% phosphoric acid (H_3PO_4). Optimal electropolishing results were achieved by not stirring the solution during electropolishing. The copper substrates were electropolished for 15 minutes using a current density of 15 A/dm^2 and subsequently cleaned in the same manner as the tungsten substrates.

5.3.2 ^{nat}Si foil production

As procuring ^{28}Si-enriched material is challenging, the technique of producing high quality foils was developed using ^{nat}Si (^{28}Si = 92.2%, ^{29}Si = 4.7%, ^{30}Si = 3.1%). Prior to evaporation, the evaporation chamber was first evacuated to a pressure lower than 5 x 10^{-7} Torr and the copper substrate holder was heated to a temperature of 360°C. The Telemark 851 Quartz Crystal Monitor provided a measure of the deposition of material during evaporation.

The first step in preparing the substrate for deposition of silicon was the deposition of a release agent. Barium chloride ($BaCl_2$) with greater than 99% purity was used for this purpose. The $BaCl_2$ was first formed from a powder into 200 mg pellets using a DAKE 10,000 psi manual hydraulic press held at 1000 psi of pressure for 20s. Prior to loading, the $BaCl_2$ pellets were baked using a hot plate to reduce their water content. For each evaporation, a total of 12 pellets (2.4 g) of $BaCl_2$ were set into a molybdenum crucible liner and placed into one of the crucible pockets. To reduce the oxygen in the residual gas, titanium was used as an oxygen getter just prior to the silicon evaporation. Pellets of titanium [131] were placed in a graphite crucible liner which occupied a second crucible pocket. Lumps of 99.95% pure ^{nat}Si obtained from Sigma-Aldrich occupied a tantalum crucible liner in the third crucible position. Initial tests with natural silicon utilized ~3 g of material in the crucible liner. To aid in depositing more evenly onto the substrate, the materials were melted prior to evaporation. To accomplish melting of the $BaCl_2$ and silicon, the e-beam was operated in low power mode, 2% (20 W) and 5% (50 W) respectively.

The $BaCl_2$ was evaporated on the substrate using an e-beam evaporator power of 3.5% to achieve a rate of ~300 Å/s until a total of 75 kÅ was deposited as measured by the QCM. Following $BaCl_2$ deposition, the shutter was moved into place and the titanium was heated using 20% beam power to getter residual oxygen. The shutter was subsequently removed and silicon was deposited onto the substrate at an e-beam evaporator power of 35%. Foils corresponding to a deposition of ~9.5 kÅ on the substrate were fabricated. This corresponds to a thickness of ~220 μg/cm^2. At 35% beam power the rate of deposition was ~10 Å/s. Approximately 85 mg of material was used during each evaporation.

Following vapor deposition, the heating block was kept at a temperature around 360°C at a pressure $< 1 \times 10^{-6}$ Torr for 24 hours to anneal the foil. This annealing
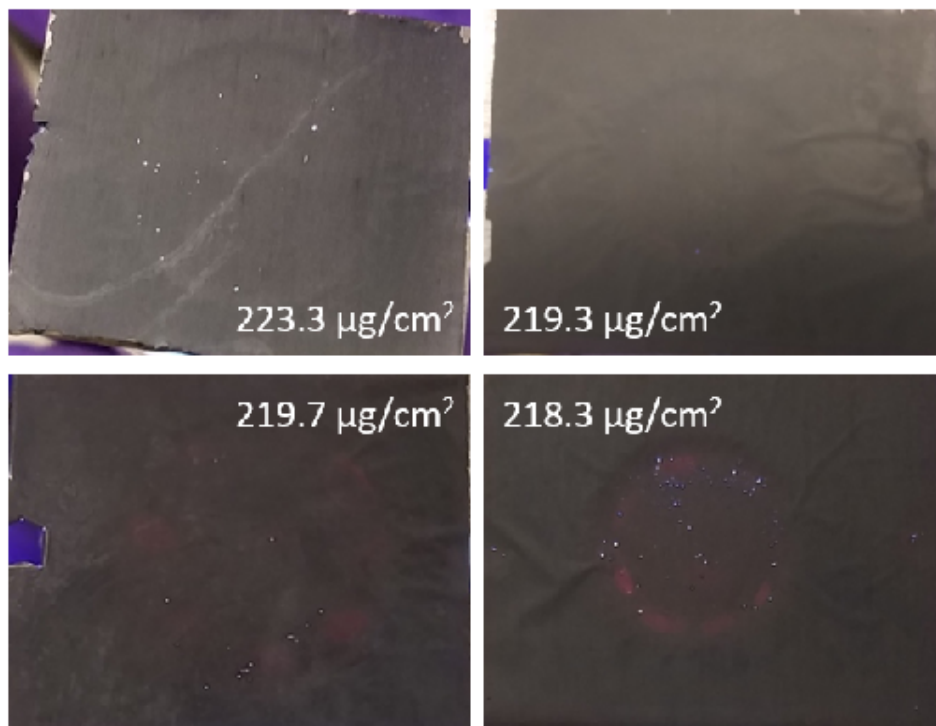
FIGURE 5.4:   Photographs of four silicon foils produced using the described procedure. The foils in the pictures are illuminated from the backside. Each foil is listed with its thickness as determined by the QCM.

process acts to reduce any stresses in the foils arising from the evaporation process. After the annealing process, the foil, substrate, and heating block were allowed to cool to 130°C in vacuum before venting the chamber using argon gas. The substrate was then removed from the chamber and interior of the chamber was wiped clean using de-ionized water followed by ethanol.

5.3.3   Floating and mounting foils

The foils produced had a silver, metallic appearance indicative of metallic silicon. The foils were released from the substrate using standard floating techniques onto the surface of de-ionized water. Upon release into the water, the foils sank to the bottom of the floating container. Foils were carefully manipulated to the surface of the water using

the mounting frames. Initial floating tests showed the foils curled tightly upon themselves making them unrecoverable. The annealing process previously described remediated the curling of the foils. A floating foil was lifted by hand onto an aluminum frame, (0.025 in. thick), which had a central hole with a diameter of either 10 or 15 mm. Foils fabricated on tungsten substrates disintegrated immediately during the floating process resulting in no useable targets. In contrast, foils produced on copper substrates were able to be successfully floated and mounted onto the frames. We hypothesize that, despite electropolishing, the surface of the tungsten substrates was rougher than the copper substrates and had a roughness comparable to the thickness of the foils deposited causing the observed fragility. Each copper substrate was able to provide foils onto a maximum of three frames. Figure 5.4 shows the metallic appearance of the foils. After mounting on frames when viewed with a light behind the foils, some small pinholes are visible as evident in Figure 5.4. Despite these pinholes, these foils have not exhibited any significant deterioration after being stored for several months in covered containers under ambient conditions.

5.3.4 ^{28}Si foil production

Following successful production of ^{nat}Si foils, the production of isotopically-enriched ^{28}Si foils was undertaken. Two grams of $> 99.8\%$ ^{28}Si was obtained from the National Isotope Development Center at Oak Ridge National Lab. The isotope used in this research was supplied by the Isotope Program within the Office of Nuclear Physics in the Department of Energy's Office of Science. To utilize less ^{28}Si starting material, a custom tungsten crucible liner with smaller capacity was fabricated. Other than the use of this small-capacity crucible liner, the production of isotopically-enriched ^{28}Si foils followed the same procedure as described for making ^{nat}Si foils. Due to their success rate in the

production of ^{nat}Si foils, copper substrates were used for the production of ^{28}Si foils. The procedure for floating and mounting the ^{28}Si foils onto frames was the same as ^{nat}Si foils.

TABLE 5.1: Thickness of silicon foils as characterized by QCM, α-gauge, and RBS measurements. All thicknesses are given in μg/cm^2.

Foil ID	Material	QCM	α	$\Delta_{\alpha-QCM}$	RBS
18	^{28}Si	218.8	-	-	-
19	^{28}Si	219.0	-	-	-
20	^{nat}Si	215.5	-	-	-
21	^{nat}Si	250.5	-	-	-
22	^{nat}Si	223.2	-	-	210
23	^{nat}Si	218.6	204.5	-6.5	299
24	^{nat}Si	218.3	223.9	2.6	-
25	^{nat}Si	217.4	228.9	5.3	-
26	^{nat}Si	218.0	221.2	1.5	-
27	^{nat}Si	219.4	220.8	0.6	-
29	^{nat}Si	219.3	205.5	-6.3	-
30	^{nat}Si	227.8	230.1	1.0	-
31	^{nat}Si	233.1	223.3	-4.2	-
32	^{nat}Si	292.6	285.5	-2.4	-
33	^{nat}Si	223.3	236.6	6.0	195
34	^{nat}Si	223.2	228.8	2.5	200
35	^{nat}Si	219.7	226.4	3.0	-
36	^{nat}Si	219.3	210.5	-4.0	-

5.4   Foil characterization

5.4.1   Foil thickness determination

Alpha-particle energy loss measurement   Although the foil thickness was monitored during evaporation using the QCM, additional measurements were made to corroborate the QCM thickness values. The foil thickness was gauged by measuring the energy loss incurred for α-particles of known energy traversing the foil. A spectroscopy-grade ^{148}Gd source (105 nCi) was used to provide 3.183 MeV α particles for these measurements. Alpha particles from the source were collimated by a 1.15 cm diameter aperture

before impinging on the foil. After passage through the foil the α-particles were detected in a silicon surface barrier detector (SBD; Ortec TD-40-300-75) collimated to 0.635 cm diameter. The energy of the α-particle was measured with and without the intervening foil. The SBD was calibrated using a 1.0 μCi ^{226}Ra source. The 950 $\mathring{A}$ dead layer was accounted for in the energy calibration of the SBD. All energy loss calculations were done using SRIM-2013 TRIM calculations [132]. The energy loss through a 220 μg/cm^2 foil is ~160 keV. The uncertainty in the determination of the centroid of the α-particle energy after traversing the foil is determined to be 2 keV (1.25%) which corresponds to a thickness uncertainty of 2.75 μg/cm^2. For the 13 foils for which both QCM and α-gauge measurements are available, the average thickness was measured to be 226.9 and 226.6 μg/cm^2, respectively. Note that the SRIM calculations did not account for any foil contaminants and, as such, provide an 'effective thickness' of Si. These values can be directly compared to those provided by the QCM as the QCM also does not account for foil contamination. The results of these measurements are given in Table 5.1. The matching results between the QCM and α-gauge measurements show the effectiveness of the QCM in measuring the thickness during evaporation while is necessary for producing foils of the desired thickness.

Rutherford backscattering measurements   Foil thickness was also determined using Rutherford backscattering (RBS) measurements. RBS measurements were conducted at Hope College's 1.7 MV Pelletron particle accelerator using 2.905 MeV α-particles. An experimental spectrum of the RBS data representative of the foils made in this work is shown in Figure 5.5. The most prominent feature of the spectrum is a wide peak ranging from 1300-1700 keV which corresponds to scattering from silicon nuclei. At lower energies, 700-1000 keV, the peak arising from scattering with oxygen nuclei is observed. The asymmetry in this peak indicates a non-uniform distribution of the oxygen through the foil. A gaussian-like peak appears at 2200 keV with a plateau on the high-energy

74
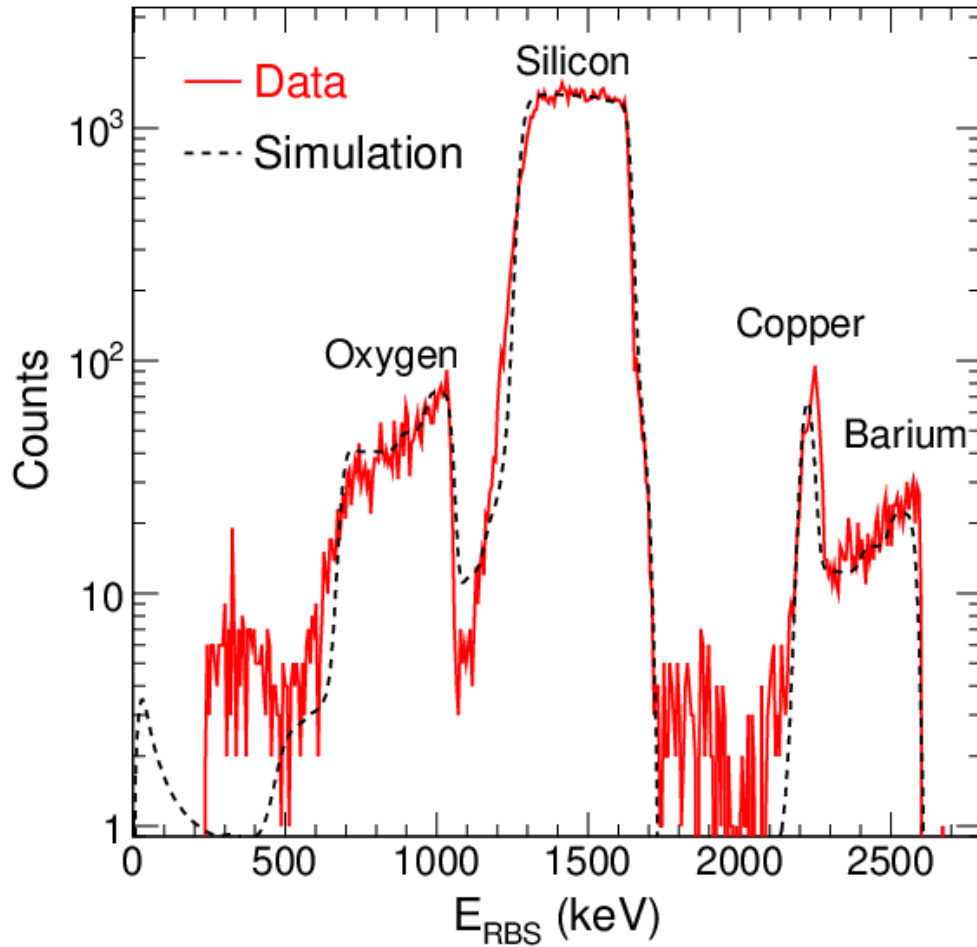
FIGURE 5.5: RBS spectrum for a ^{nat}Si foil. The red, solid line corresponds to data while the black, dashed line corresponds to a simulated spectrum.

side that extends past 2500 keV. Residual copper diffusing from the substrate into the foil is responsible for the peak while barium from the release agent is responsible for the plateau. All but one of the RBS thicknesses given in Table 5.1 are in reasonable agreement with the QCM and α-gauge values. The discrepant result for foil 23 is not presently understood.

5.4.2 Foil elemental abundance determination

Rutherford backscattering measurements In addition to providing information on the foil thickness, RBS provides information on the elemental abundances of a foil. A simulated RBS spectrum created using SIMNRA software [133] is shown in Figure 5.5 as a dashed curve superimposed on the RBS data. Simulated spectra account for variation in abundances through the foils by segmenting the foil into multiple layers of varying thicknesses and elemental abundances. The asymmetry of the oxygen peak in the RBS spectrum indicates an increased oxygen content at one surface of the foil. Analysis of the RBS data reveals that beyond this enhanced oxygen surface layer, in the bulk region of the foil, the silicon content is 90-95%. The copper and barium peaks seen in the RBS spectra indicated that each of these elements consituted less than 1% of the total abundance in each foil. The silicon abundance for each foil was calculated as the average silicon content over all layers in the foil, including the enhanced oxygen surface layer. A summary of silicon content for measured foils is given in Table 5.2. RBS measurements of elemental abundance is a critical tool for future foil production. While the results of Section 5.4.1 show that both QCM and α-gauge measurements could be used for final foil thickness determination (making RBS measurements redundant), RBS is the simplest *non-destructive* technique for determining the elemental abundance of target foils.

X-ray photoelectron spectroscopy measurements In order to provide an independent check of foil elemental purity, X-ray photoelectron spectroscopy was used. XPS measurements were taken using a PHI VersaProbe II X-ray Microprobe system in the Indiana University Nanoscale Characterization Facility. XPS is inherently a surface-measuring technique as the electrons which are removed must escape the sample in order to be measured. In contrast to RBS, XPS is a destructive technique but provides an alternative measurement method for corroborating the foil elemental abundances. To

aid in understanding bulk elemental abundances, the instrument allows for sputtering of argon ions onto samples thus providing elemental analysis as a function of depth. The effective depth is based upon the rate of ion sputtering and the thickness determination from the QCM and α-gauge measurements. At the surface of the foil, the argon ion is sputtered using 1 kV accelerating potential while in the bulk the accelerating potential is increased to 4 kV. As the ion sputtering rate is varied between the foil surface and the bulk, an uncertainty exists in the relative depth between these two regions. In assessing the elemental abundance in the bulk of the material the sputtering rate is held constant.

A representative foil depth profile is presented in Figure 5.6. A silicon oxide layer is clearly observed on the front side of the foil which contains a much higher oxygen content than the bulk foil, in qualitative agreement with the RBS results. This oxide layer extends for approximately 100 nm inside the foil. Beneath this layer of silicon oxide the film appears relatively uniform with a silicon abundance of 85-90%. The decrease in silicon abundance occuring around $\sim$0.95 μm corresponds to the back side of the foil. The spike in carbon abundance at this depth is a background signal originating from the mounting of the foil inside the XPS instrument. The carbon seen at the front of the foil is environmental carbon on the surface of the sample and is often observed in XPS measurements. The silicon abundances reported in Table 5.2 were calculated as the average abundance through the bulk foil, excluding the enhanced oxygen surface layers. The uncertainty in the relative depth between the surface and bulk layers prevents determination of the elemental abundance over the entire foil. Both the RBS and XPS measurements demonstrate the ability to produce silicon foils with silicon purity of 87-90%. The RBS and XPS results for foils 33 and 34 indicate the determination of the silicon content is consistent within $\sim$3%.

The measurement of the residual oxygen in the chamber shown in Figure 5.3 shows the oxygen only makes up $\sim$1% of the remaining gas in the chamber at the time of foil
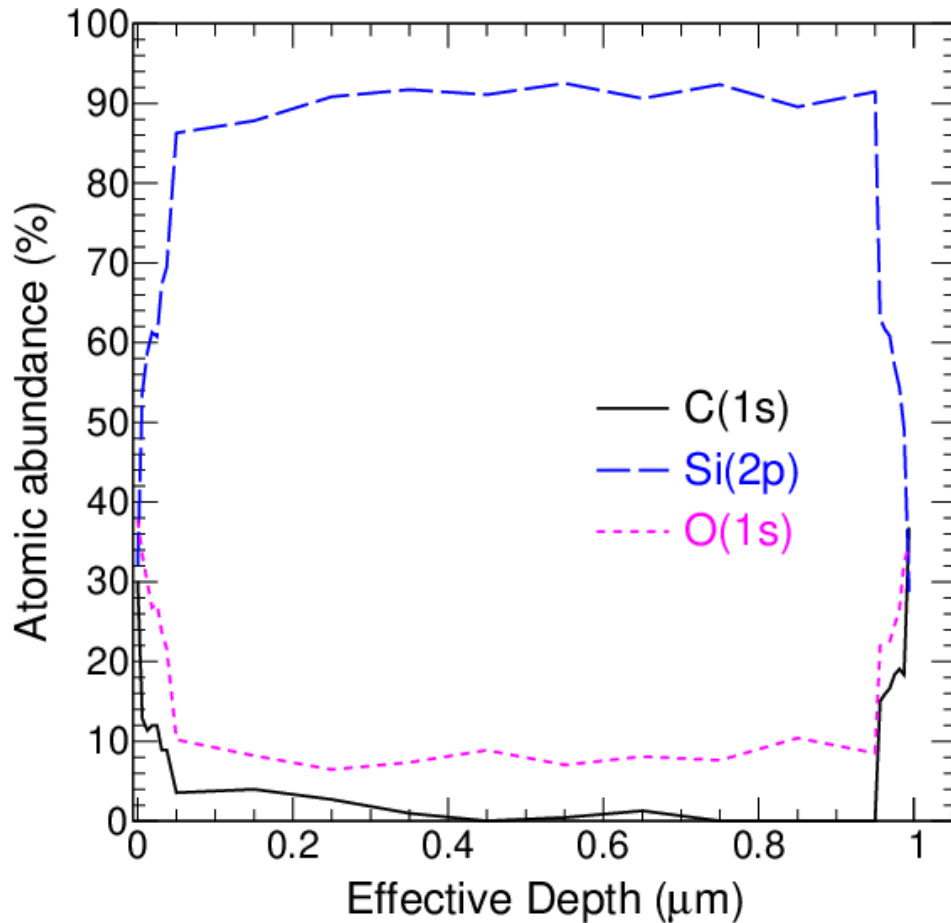
FIGURE 5.6: XPS depth profile for various elements in a ^{nat}Si foil. The effective depth is based upon the ion accelerating voltage and the depth determination from the QCM and α-gauge measurements.

production. If the oxygen present in the foils was coming entirely from the chamber's residual gas, it would be reasonable to assume an oxygen content of $\sim$1% in the foil bulk material. The elevated oxygen content in the bulk medium ($\sim$10%) suggests another source of oxygen is present in the chamber. One possibility for this source of oxygen is oxidation on the surface of the silicon material used to make the foils. It may be possible to reduce or eliminate this source of oxygen by reducing the silicon material prior to placing it inside the chamber. It is clear that further reduction in the chamber's base pressure would have little effect on reducing the foil oxygen content.

Several sets of foils have been produced and characterized using the methodology

78

TABLE 5.2: Assessment of foil silicon content via XPS and RBS.

Foil ID	Material	XPS %Si	RBS %Si
18	^{28}Si	88.5	-
20	^{nat}Si	87.3	-
22	^{nat}Si	-	87.57
23	^{nat}Si	-	89.44
27	^{nat}Si	89.6	-
33	^{nat}Si	90.4	89.34
34	^{nat}Si	86.8	89.75

described above. Experiment E20022 conducted at Michigan State University at the ReA3 linear accelerator in stand-alone configuration was the first experiment to use target foils made at Indiana University. E20022 measured fusion of ^{28,30,32}Si $+$ ^{28}Si using the ETOF method. The symmetric and nearly-symmetric reactions measured for this experiment required the flight path between the target and downstream detectors to be small in order to retain a high geometric efficiency. This shorter flight path as compared to previous experiments shortened the flight time of fusion evaporation residues and reduced the separation between the residue island from fusion on ^{28}Si and fusion on ^{16}O. This reduction in ability to discriminate reactions from Si and O necessitated using a target with as low an oxygen content as possible.

Chapter 6

MuSIC@Indiana

6.1 Design, construction, and commissioning

6.1.1 Design and construction of MuSIC@Indiana

The desire to measure the fusion excitation functions with beam rates less than $1\text{x}10^3$ particles/s necessitated the design and construction of an active target detector: MuSIC@Indiana. The overall design of MuSIC@Indiana is similar to other MuSIC detectors presently in use [77, 95, 99] but with several key differences. The active volume is formed by six printed circuit boards (PCBs) which together constitute a rectangular box. The top and bottom of the box serve as the anode and cathode respectively. Between the anode and cathode is a wire plane (50 μm diameter Au-W wires on a 1 mm pitch) that acts as a Frisch grid. A side view of MuSIC@Indiana indicating the anode-to-Frisch grid and Frisch grid-to-cathode spacings is presented in Figure 6.1. To provide a short collection time of the primary ionization produced by an incident ion, the detector was operated at a reduced electric field of $\sim$0.7 kV/cm/atm between the cathode and the Frisch grid. This field yields an electron drift velocity of $\sim$10 cm/μs in both CH_4 and CF_4 [134, 135]. A significantly higher reduced electric field between the Frisch grid and the anode ($\sim$1.4 kV/cm/atm) minimizes termination of electrons on the Frisch grid. Field shaping at the edges of the detector is accomplished using printed circuit boards with 1.613 mm strips and a center-to-center pitch of 3.226 mm. The shaping of the electric field by these printed circuit boards is different from other current MuSIC detectors which use parallel wires. The use of printed circuit boards simplifies the addition of a 30 mm diameter hole in the upstream and downstream PCBs. These holes allow the
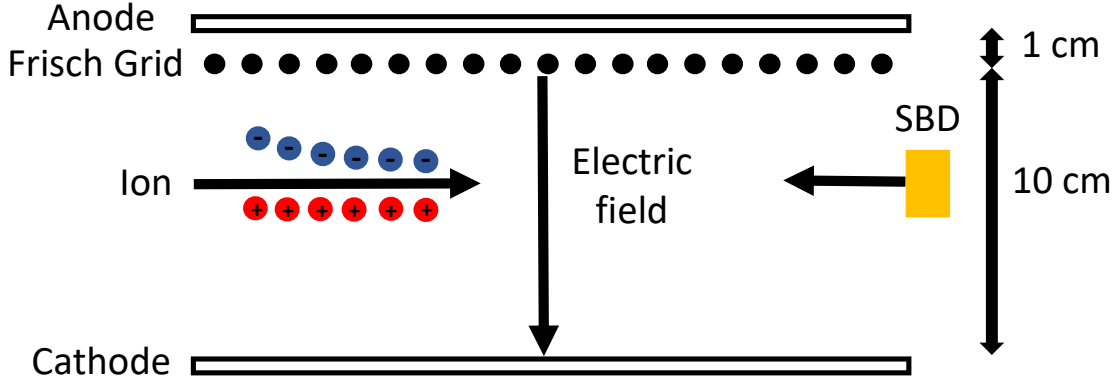
FIGURE 6.1: Schematic side view of MuSIC@Indiana. Insertion of the SBD from downstream into the active volume is also indicated.

beam to enter and exit the active volume of the detector. The hole in the downstream PCB also enables the precise insertion of a small silicon surface barrier detector (SBD) using a linear-motion vacuum feedthrough (Huntington L-2211-6). This ability to insert a SBD precisely into the active volume is critical in the calibration and operation of MuSIC@Indiana and makes MuSIC@Indiana unique among MuSIC detectors.

The dimensions of the active area of MuSIC@Indiana are indicated in Figure 6.2. MuSIC@Indiana is approximately twice as wide as other current MuSIC detectors [94]. The relatively large width of MuSIC@Indiana means the measurement of ER energy loss will have high efficiency even for reactions where ERs reach angles as large as 45°. The anode in MuSIC@Indiana is subdivided into 20 distinct segments along the beam direction. Further segmentation transverse to the beam direction provides the left (L0-L19) and right (R0-R19) geometry depicted in Figure 6.2. Each anode segment is 1.219 cm wide with a 0.031 cm inter-strip separation between anodes. This width for an anode segment along the beam direction was chosen to provide a sufficiently large ΔE signal to yield a good signal-to-noise ratio. When the detector is operated at P = 150 Torr of CH_4 gas, an incident ^{18}O ion with E_{lab} = 50 MeV deposits a ΔE of ~1.5 MeV for a single anode.
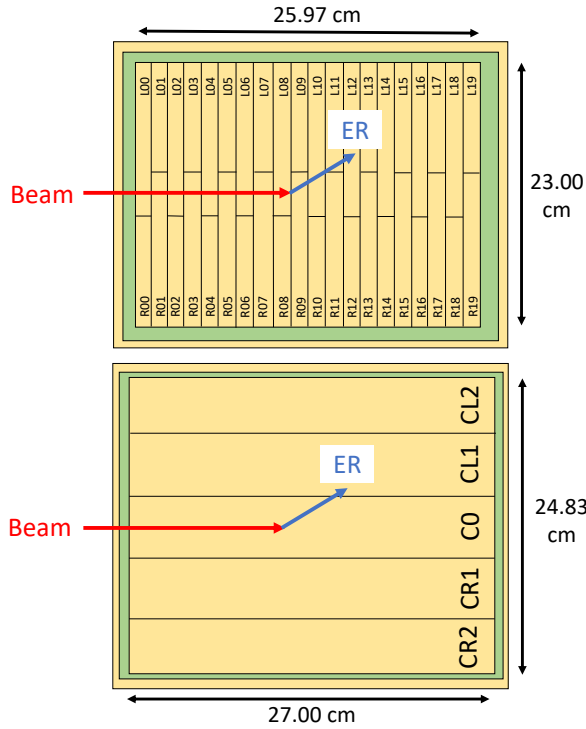
FIGURE 6.2: Schematic layout of the MuSIC@Indiana anode (top) and cathode (bottom). The dimensions given are for the active areas of the detector.

Anode 0 is used as a 'control anode' to reject fusion or scattering events from the beam on nuclei in the entrance window or gas prior to entering the detector active volume. For adjacent anode strips, left and right anode strips alternately overlap the 0° beam path by 1 cm as indicated in Figure 6.2. This left-right geometry has been successfully used in other MuSIC detectors [77] to distinguish fusion events from two-body scattering (discussed further in Section 6.1.3).

The cathode is divided into 5 strips which run parallel to the beam direction. These strips are labeled C0, CL1-2, and CR1-2 as illustrated in the schematic shown in Figure 6.2. The labels 'CL' and 'CR' on these strips correspond to the beam-left and beam-right cathode strips respectively. Segmentation of the cathode reduces its capacitance making the capacitance of each cathode strip comparable to an anode segment enabling a fast response for the sensing of the electron motion away from the cathode.

82
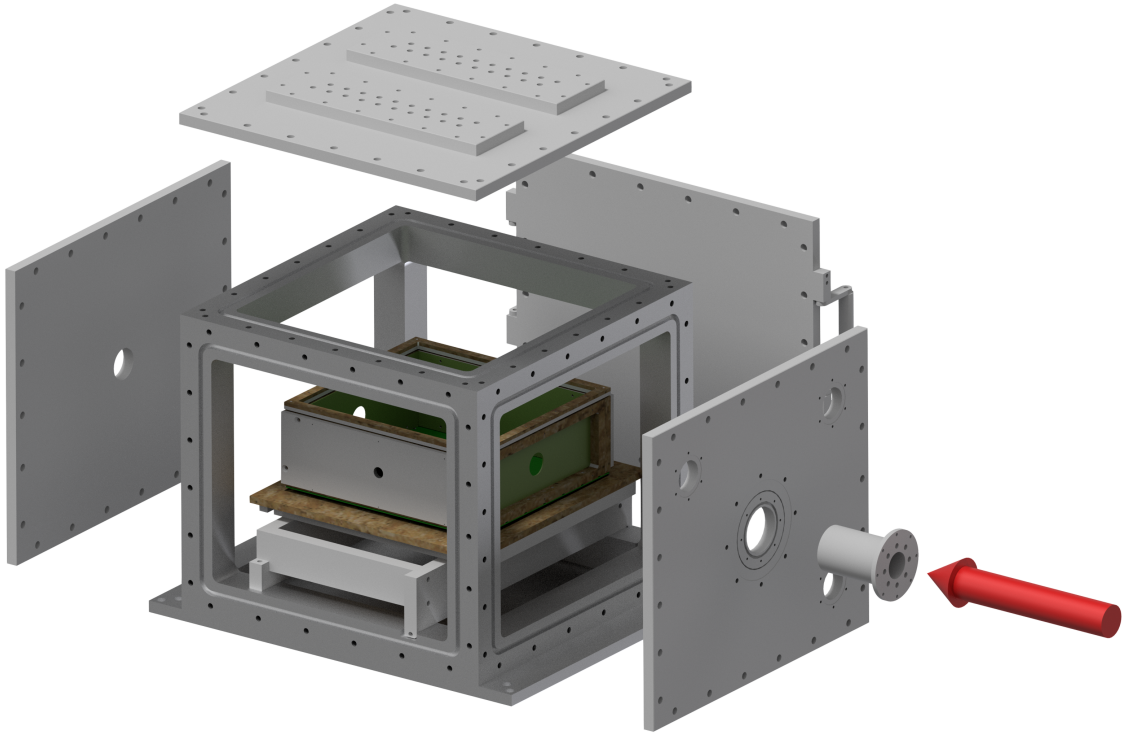
FIGURE 6.3: CAD of the chamber that houses the active region of MuSIC@Indiana. The arrow indicates the direction of the incident beam.

The active detector is housed inside of a 18" (W) x 18" (L) x 15.5" (H) chamber which was machined from a solid block of aluminum by Indiana University Mechanical Instrument Services resulting in cube shown in Figure 6.3. This fabrication approach ensures a clean machined interior surface which is free of welds. A clean chamber interior surface allows the chamber to achieve the lowest possible pressure which is important for removing contaminant gasses from the chamber prior to the detector being filled with the target gas. The six sides of the cube are sealed by six large flanges with 'O' rings. SMA electrical feedthroughs transport the 40 anode signals through two flanges situated on the top flange. Connected to each of these two flanges is a motherboard housing 20 high-quality charge sensitive amplifiers (CSAs) [136]. Coaxial cables transmit the CSA output to analog electronics which process the signals before being recorded by the data acquisition. Feedthroughs for the cathode signals, biasing of the anode and cathode, along

with pumping and gas inlet and outlet are located on the bottom flange. The upstream flange provides a re-entrant window while the downstream flange provides the means to insert the SBD detector using a linear positioner. The re-entrant window provides separation of the gas volume from the vacuum upstream. During an experiment, this window consists of a 2.6 μm doubly-aluminized mylar window sealed with an 'O' ring. This window was successfully tested to a pressure of 200 Torr. A thinner window of 1.5 μm doubly-aluminized mylar was tested but exhibited some leakage at a pressure of 100 Torr (which was lower than the desired pressure for the commissioning experiment).

As it functions as an active target, maintaining contaminant free gas at a stable pressure is critical to the proper operation of MuSIC@Indiana. This was accomplished by using an oil-free gas handling system (GHS). During operation, gas was continuously flowed through the detector via the GHS with the flow controlled by an electronic valve/controller (MKS 0248D-00500RV). The gas flow rate was chosen so that the gas volume of the detector ($\sim$55 L) was replenished in approximately one hour. Feedback for the solenoid valve was provided by monitoring the pressure inside the detector using a MKS Model 226 Differential Pressure Transducer. With this GHS it was possible to maintain a stable pressure in the detector to within 0.1 Torr of the set pressure. The pressure inside MuSIC@Indiana was independently measured using a absolute piezovaccum transducer (Newport 902B) with an accuracy of 0.1 Torr.

First tests on MuSIC@Indiana were carried out using a spectroscopy-grade 105 nCi ^{148}Gd disk source which emits a 3.183 MeV α particle. To ensure that the entire α energy was deposited over a single anode, the detector was operated at a pressure of 400 Torr of CF_4 gas. The source was then sequentially positioned over each anode segment and the energy deposited by the α particle over that segment was measured. Under these conditions, the adjacent segments showed no appreciable energy deposit from the

α particle. The results of these bench tests revealed that the inherent resolution of each anode is ~100 keV FWHM.

6.1.2 Characterization of MuSIC@Indiana with beam

The fusion excitation function for ^{18}O+^{12}C has been well measured [79, 97, 101, 137] and therefore provided a useful reference measurement for the commissioning of MuSIC@Indiana. To measure this excitation function, a beam of ^{18}O^{6+} ions was accelerated to an energy of $E_{lab} = 55$ MeV by the Notre Dame Nuclear Science Laboratory's 10MV Tandem Accelerator. The beam intensity was reduced to an intensity of ~10^4 particles/s in a controlled manner by passing it through slits and a 1/1000 sieve well upstream of the setup. The resulting low-intensity beam was focused onto MuSIC@Indiana filled with CH$_4$ gas at a pressure of 150 Torr. The cathode and anode were biased to voltages of -1500 V and 400 V respectively with the Frisch grid held at ground. The data acquired for this measurement was collected in just 10 hours.

Representative anode and cathode signals, processed by the high quality charge-sensitive amplifiers (CSAs) [136], are presented in Figure 6.4. These CSAs yield ~9 mV amplitude signal for a 3.183 MeV α particle in 400 Torr of CF$_4$. Collection of electrons by the anode together with inversion by the CSA determines the polarity of the anode signal. The risetime of this signal is approximately 100 ns as evident in the inset of Figure 6.4, consistent with the electron drift velocity of ~10 cm/μs and the Frisch grid to anode spacing of 1 cm. Examination of the cathode signal reveals a much larger amplitude which can be understood by noting that the cathode integrates the entire energy along the beam direction while the anode only collects a small portion of the particle's total ionization. The risetime of the cathode signal (~500 ns) is observed to be slower than the anode. This difference is due to the larger cathode-to-Frisch grid spacing as compared to the one for the anode-to-Frisch grid. It is also observed that the cathode signal precedes

85
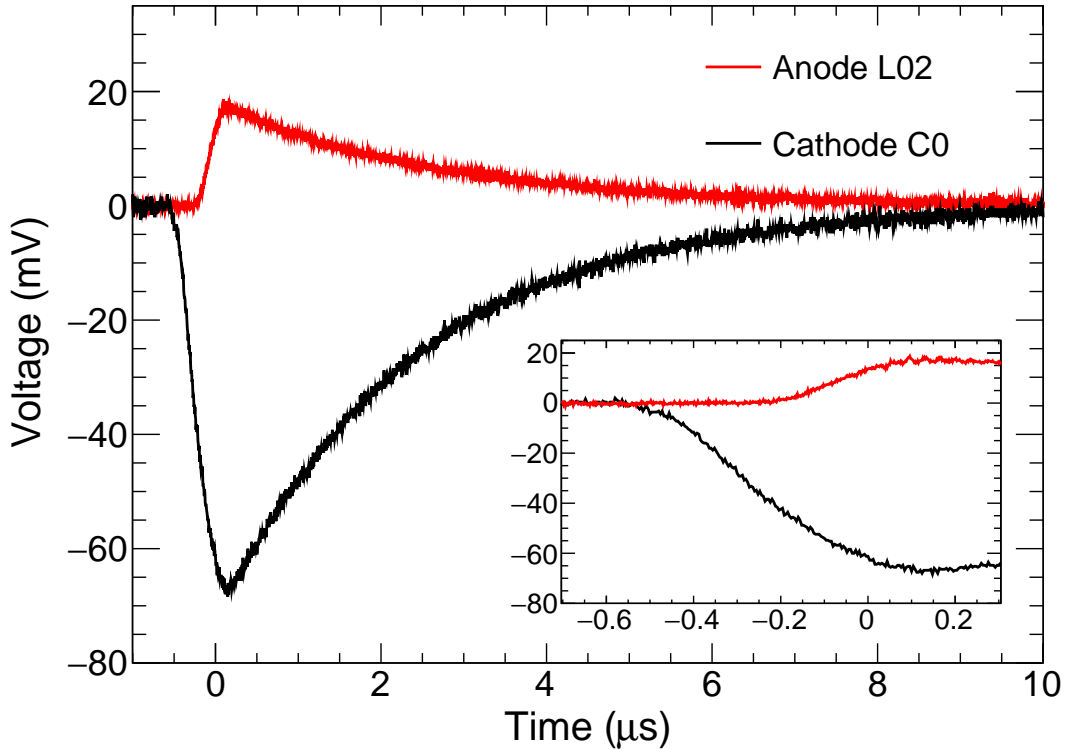
FIGURE 6.4: Representative CSA signals from single MuSIC@Indiana anode and cathode strips. The inset focuses on the rising edge of the same signals.

the anode signal by 400 ns. The delay of the anode relative to the cathode is due to the shielding of the anode from electron motion until they have passed the Frisch grid. It should be noted that the signal observed for the cathode is not due to the motion of the cations but due to the motion of the electrons away from the cathode. The fall time of the CSA signals is only $\sim$8 μs which allows successful operation of MuSIC@Indiana at a rate up to 1 x 10^5 particles/s.

The CSA signals from the detector are processed through standard shaping amplifiers and peak sensing digitizers (CAEN V785 ADC) before being acquired by the VME data acquisition system (DAQ) and recorded on the computer. The DAQ was triggered using signals from the segmented cathode. Each cathode's CSA signal was processed by a timing filter amplifier (TFA) and shaping amplifier. The TFA signals were summed,

discriminated and the resulting logic signal was used to gate the ADCs as well as trigger the data acquisition system.

Measuring the fusion excitation function requires knowledge of the incident energy across each anode. To measure this energy, a surface barrier detector was inserted from downstream into the active volume of the detector. Use of a precision linear positioner allowed the SBD to be positioned at the front and back of each anode with an accuracy of 0.5 mm. The energy of the beam was recorded at these positions at low beam intensity. Previous fusion measurements have assigned the beam energy at each anode based on energy loss programs such as SRIM [132] or LISE++ [138]. The SBD measurement in MuSIC@Indiana removes the need for such programs which have been established to have uncertainties of approximately 10% [94, 99].

6.1.3 Simple MuSIC@Indiana data analysis

Schematically illustrated in Figure 6.5 is the sequence for analyzing data from Mu-SIC@Indiana. The initial step in the analysis of MuSIC data involves the calibration of the left and right anode segments using the energy loss of the beam as measured by the SBD. Once the left and right segments have been calibrated, the two sides can be summed to calculate the total energy loss in an anode. For all subsequent steps in the analysis only the summed anode energy loss is used.

The second step in the analysis is to require the incident ion have the ΔE of the beam ($\pm$ 300 keV) in anode 0. This step is critical to accurately measuring the excitation function as it eliminates events where fusion occurs in either the window or gas upstream of the active area of MuSIC@Indiana. It also removes any beam pileup events.

After ensuring entry of a clean beam event into MuSIC@Indiana with the prior requirement, the analysis requires that the anode of maximum energy loss is not anode

1. Calibrate anodes; $\Delta E_{A(I)}^{Total} = \Delta E_{A(I)}^{Left} + \Delta E_{A(I)}^{Right}$

2. Require $\Delta E_{A(0)} = \Delta E_{beam(0)} \pm 300\ keV$

3. Require $\Delta E_{A(19)} \neq \Delta E_{Max}$

4. Define high ($\Delta E_{High(I)}$) thresholds using the remaining events in $\Delta E_{A(I)}$ vs $\Delta E_{A(I+1)}$ correlations

5. Require at least one anode to have $\Delta E_{A(I)} > \Delta E_{High(I)}$

6. For events where multiple anodes have $\Delta E_{A(I)} > \Delta E_{High(I)}$, require all such anodes be adjacent

7. Require ΔE drops monotonically after the maximum

8. Define low ($\Delta E_{Low(I)}$) thresholds using fusion events in $\Delta E_{A(I)}$ vs $\Delta E_{A(I+1)}$ correlations

9. Assign fusion to the first anode with $\Delta E_{A(I)} > \Delta E_{Low(I)}$

FIGURE 6.5:   MuSIC@Indiana analysis logic flowchart.

19. Anode 19 thus functions as a control anode. Requiring $\Delta E_{A(19)} \neq \Delta E_{Max}$ removes events (both fusion and scattering) which occur close to the downstream end of the detector.

After these first two requirements have been implemented, the correlation between the deposited energy in an anode and the energy deposited in the subsequent anode is examined. A representative correlation is shown in Figure 6.6a for anodes 12 and 13. Several features appear in the correlation each of which was identified by examining plots of ΔE vs anode number (called traces) associated with each feature.
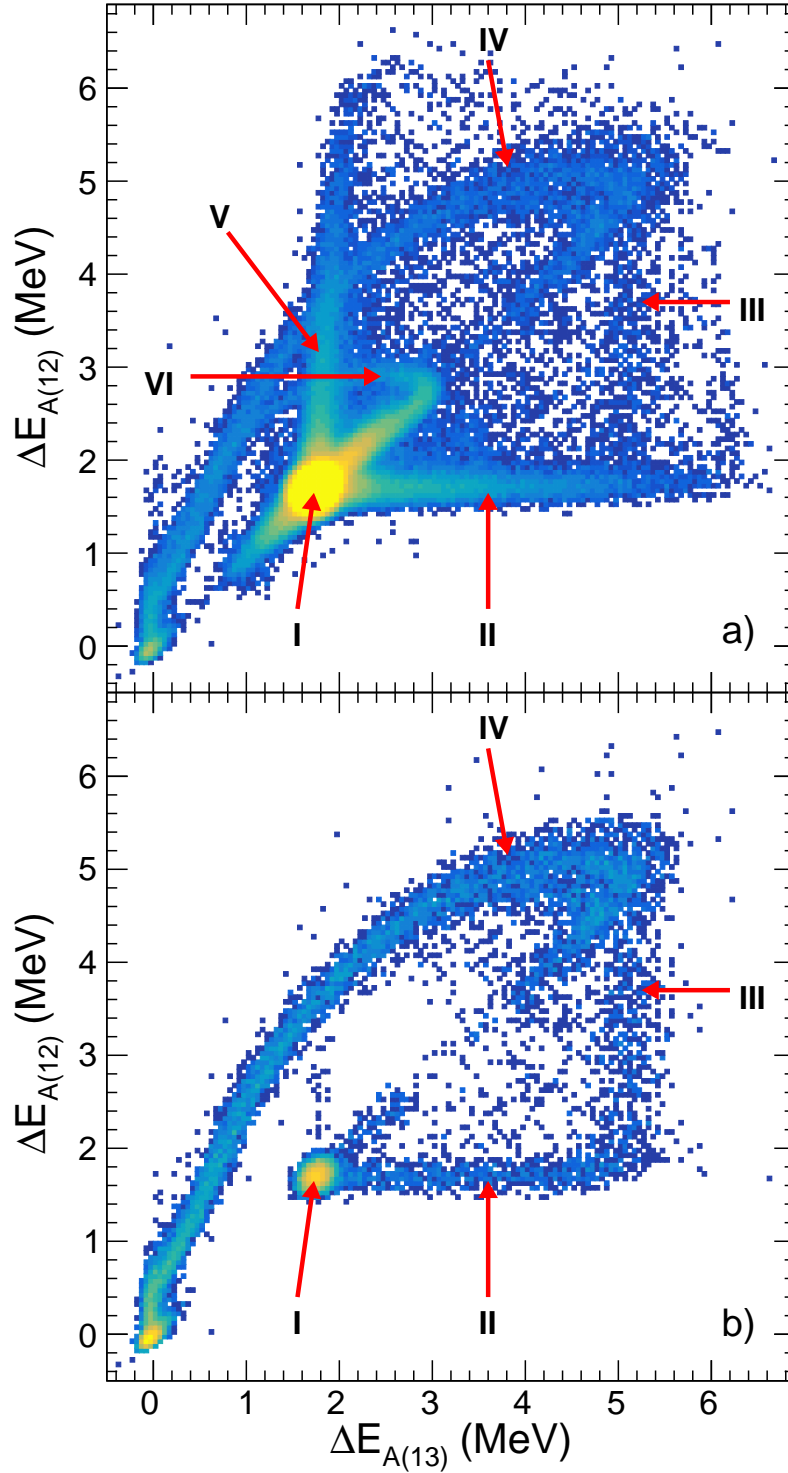
FIGURE 6.6: $\Delta E_{A(12)}$ vs $\Delta E_{A(13)}$ correlations. The upper plot shows the correlation after the first three steps of the analysis. The bottom plot shows the correlation only for events which were identified as ERs. Features of the correlations are identified by numerals and are explained in the text.

Feature I The most prominent feature in the spectrum is the bright spot at $\Delta E_{A(12)}$ = 1.8 MeV and $\Delta E_{A(13)}$ = 1.8 MeV which corresponds to events which are beam in both anode 12 and anode 13.

Feature II The second feature is a horizontal band which extends from the beam peak out to $\Delta E_{A(13)} \sim 6$ MeV. This feature corresponds to events where fusion occurs in anode 13. The fusion product with its larger atomic and mass number than the beam has a larger specific ionization (dE/dx) and consequently a larger energy deposit.

Feature III Extending vertically from $\Delta E_{A(12)}$ = 1.8 MeV and $\Delta E_{A(13)}$ = 5.2 MeV is a faint line which corresponds to events where fusion occurred in anode 12.

Feature IV Starting from $\Delta E_{A(12)}$ = 5.2 MeV and $\Delta E_{A(13)}$ = 5.2 MeV and extending as a tail to lower ΔE are events where fusion occurred in anodes prior to anode 12. This locus terminates at a distinct peak at $\Delta E_{A(12)}$ = 0 MeV and $\Delta E_{A(13)}$ = 0 MeV. This peak is associated with events in which fusion occurred much earlier in the detector and the ER has already ranged out in the detector gas prior to anode 12.

Feature V The near-vertical band extending from the beam peak corresponds to two-body events which are subsequently eliminated in the analysis.

Feature VI Extending diagonally from the beam peak up to $\Delta E_{A(12)}$ = 2.8 MeV and $\Delta E_{A(13)}$ = 2.8 MeV, and then turning with a tail back down to $\Delta E_{A(12)}$ = 0 MeV and $\Delta E_{A(13)}$ = 0 MeV are proton capture events resulting from the fusion of beam on hydrogen in the CH$_4$ detector gas. Proton capture of the ^{18}O beam results in ^{19}F which exhibits a larger specific ionization than the beam but less than that of the ERs. These proton

90

capture events are characterized by ΔE values that are higher than the beam for several consecutive anodes before dropping to $\Delta E = 0$ MeV at the end of the detector. A representative proton capture event is presented in Figure 6.7a

Correlations like the one shown in Figure 6.6a are used in the analysis to establish the quantity $\Delta E_{High(I)}$ for each anode. For example, Figure 6.6a was used to set $\Delta E_{High(12)}$ = 3.2 MeV, a measure of the maximum energy deposit associated with proton capture for that anode. Requirement that at least one anode has $\Delta E_{A(I)} > \Delta E_{High(I)}$ eliminates proton capture events from the data leaving putative fusion events.

After removing the proton capture events, the analysis requires that if multiple anodes have $\Delta E_{A(I)} > \Delta E_{High(I)}$, those anodes must be adjacent. This requirement rejects the majority of two-body scattering events. A representative two-body scattering event is shown in Figure 6.7b. Two-body scattering events are characterized by two particles with different specific ionization and consequently two ranges. This behavior is clearly evident in Figure 6.7b where one particle has a range of 1-2 anodes and the other has a range of approximately 11 anodes. Observation of two Bragg peaks in the trace is a clear indication of two particles in a single event.

Not all two-body scattering events are eliminated through the previous analysis step. To remove the remaining scattering events, the analysis requires that the ΔE drops monotonically after the anode of maximum ΔE. This requirement specifically eliminates scattering events where the low specific ionization (beam-like) particle has a long track and does not pass the high threshold later in the detector. This analysis is distinct from previous MuSIC analyses which required the use of the detector's left/right anode structure to distinguish two-body events from fusion events [94]. While events containing two particles can be eliminated by using the left/right information, the analysis steps described in this paper provide a simple and equally effective way of removing two-body scattering events from the data.

91
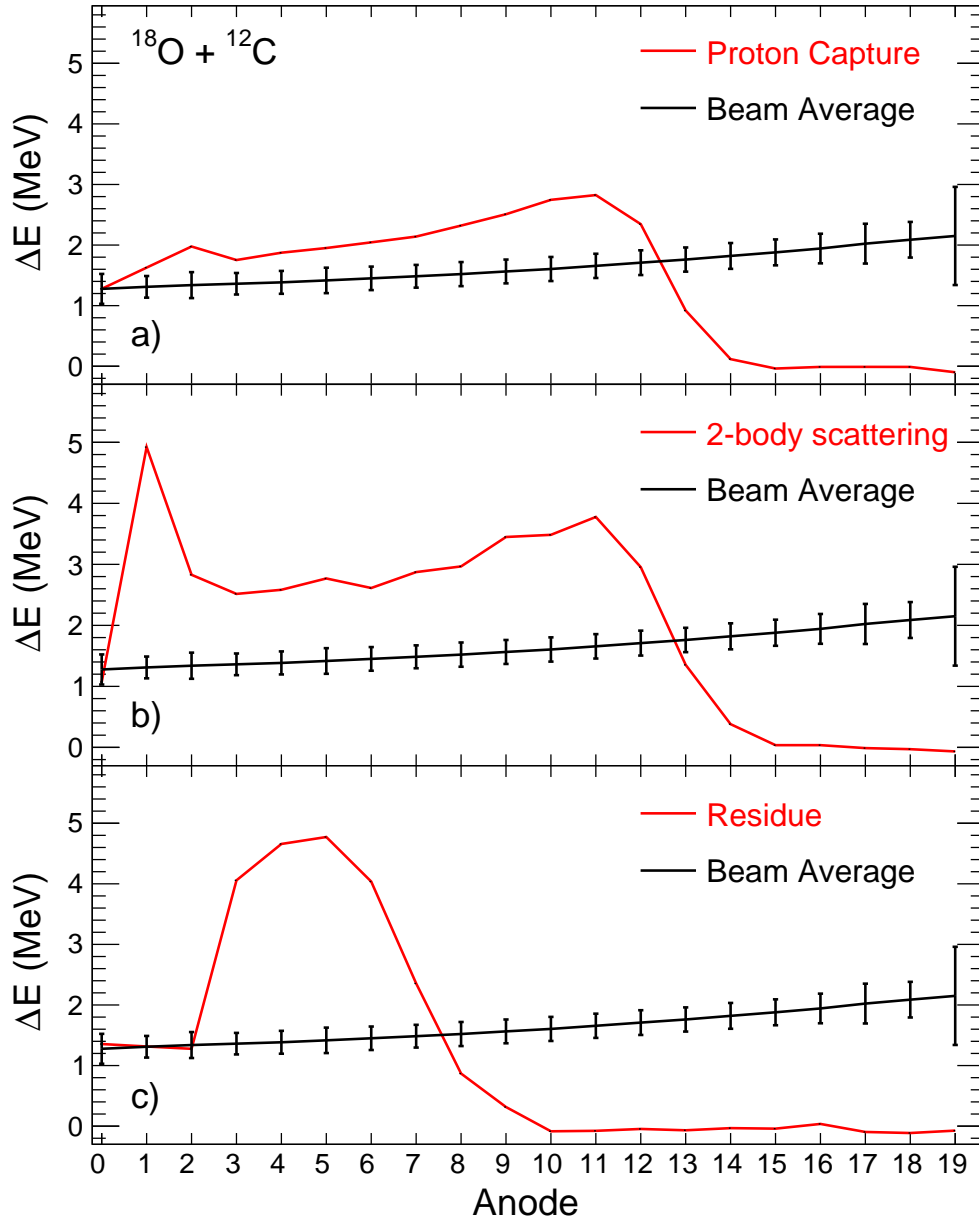
FIGURE 6.7: Experimental MuSIC@Indiana traces. Panel a) shows the trace for a proton capture event. Panel b) shows the trace for a two-body scattering event. Panel c) shows the trace for a residue from fusion occurring in anode 3. For all panels, the average beam trace is shown as the black line. The error bars on the average beam trace represent the FWHM of the beam ΔE distribution in that anode.

All remaining events are assigned as fusion events. A representative trace of a fusion event is presented in Figure 6.7c. Prior to anode 2 the ΔE observed is consistent with that of beam. At anode 2 the ΔE increases markedly reaching a maximum at anode 5 whereupon it decreases monotonically until anode 10. No additional energy is observed at subsequent anodes. Using the fusion events selected in this manner, correlations like the one shown in Figure 6.6b are made. After all of the analysis steps have been followed, Features V and VI as well as the scattering events in Feature II have been removed. The residues appearing in Features II, III, and IV are now clear. The remaining events in Feature I of Figure 6.6b correspond to fusion events which happen in anodes after anode 13. Using this correlation a low threshold, ΔE$_{Low(I)}$, is established for each anode. This threshold is set just above Feature I and is used to assign the anode of fusion. For example, Figure 6.6b was used to set ΔE$_{Low(12)} = 2.2$ MeV. The anode of fusion is assigned to the first anode with ΔE$_{A(I)} > \Delta$E$_{Low(I)}$.

6.1.4 ^{18}O+^{12}C excitation function

Once the occurrence of fusion has been identified and assigned to the appropriate anode, the cross-section can be calculated using: $\sigma = N_{ER}/(\epsilon * I * t)$, where N$_{ER}$ is the number of ERs in an anode, ϵ is the detector efficiency of an anode, I is the number of incident beam particles, and t is the target thickness as defined by the anode width and the gas pressure.

Use of anodes 0 and 19 as control anodes prohibits using them in the measurement of the excitation function. Moreover, the most downstream anodes are less than 100% efficient. An anode can be considered 100% efficient if there are a sufficient number of anodes to observe the peak in the corresponding trace, which requires 4-5 anodes. Consequently, the fusion cross-section is measurable for anodes 1 - 15 with 100% efficiency. Given this intrinsic efficiency, no efficiency correction is necessary to extract the fusion
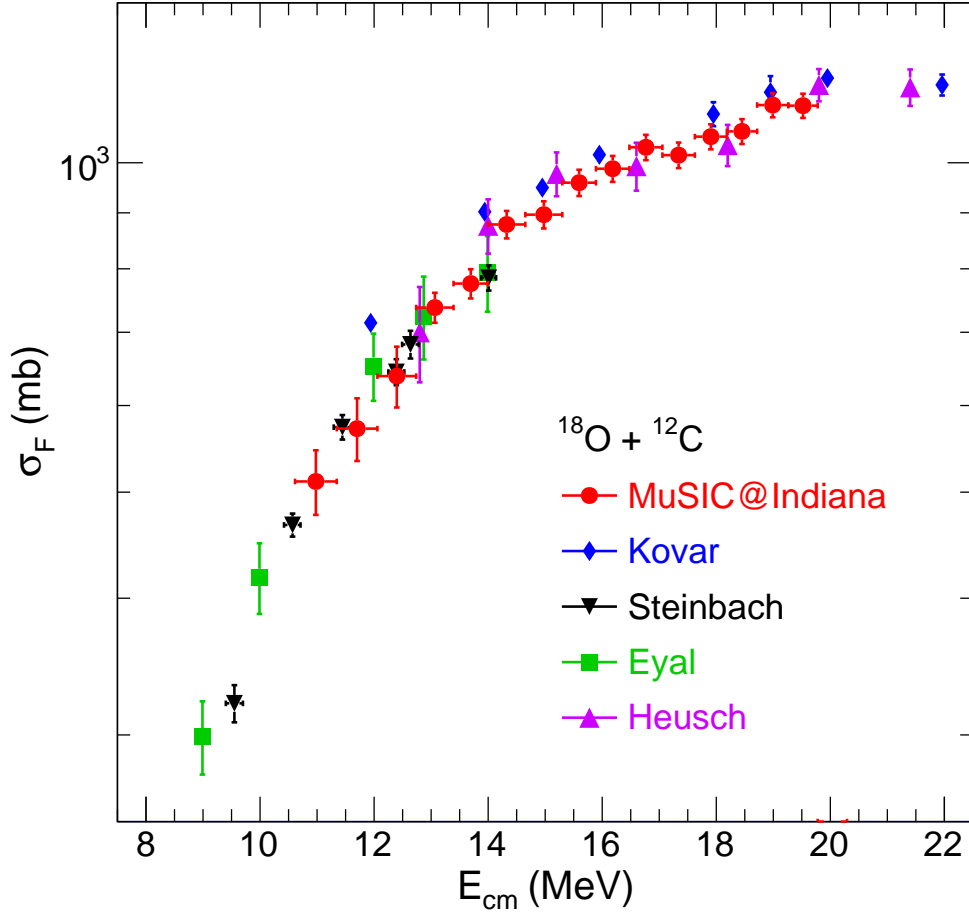
FIGURE 6.8: Fusion excitation function of $^{18}O+^{12}C$. The literature datasets are Kovar [97], Steinbach [79], Eyal [101], and Heusch [137].

cross-section when measurement of fusion is restricted to this section of the detector. The setup of this experiment thus enabled the measurement of the fusion cross-section for $^{18}O+^{12}C$ between 11 MeV < E_{cm} < 20 MeV.

In order to assign an energy to the cross-section associated with a particular anode, the SBD measurement of the beam at the front and back of each anode was used. Each datapoint in the excitation function is initially assigned the energy in the middle of the associated anode (calculated as the average of the energies at the front and the back of the anode). In reality the energy average of the anode is weighted toward higher energy (the upstream side of the anode) where generally the cross-section is higher. To correct

for this, the initial excitation function is parameterized using a Wong formalism [110]. Each datapoint is then segmented into 20 equally-spaced slices in energy. The new energy is calculated as the weighted average of the energy of the slices using the Wong-calculated cross-section:

$$E' = \frac{\sum[\sigma_{Wong}(slice) * E(slice)]}{\sum \sigma_{Wong}(slice)}$$

This process is repeated until the energy converges. Horizontal error bars represent the difference between the assigned anode energy and the energy at the front/back of the anode. The size of the vertical error bars are calculated from the experimental statistics.

The measured MuSIC@Indiana $^{18}O+^{12}C$ excitation function is displayed in Figure 6.8. It is observed to be in good agreement with the previously reported cross-sections in the literature. Below $E_{cm} = 14$ MeV the MuSIC@Indiana measurement matches the Eyal [101] and Steinbach [79] measurements even to the extent of interpolating between the published points in those datasets. In this same region there are two datapoints from Kovar [97] and one datapoint from Heusch [137] which are high relative to Eyal, Steinbach, and MuSIC@Indiana. This result suggests that Kovar and Heusch may provide a systematically high measurement of the cross-section. This trend continues above E_{cm} = 14 MeV with the MuSIC@Indiana cross-sections below all Kovar datapoints. The two points from Heusch between E_{cm} = 16 and 19 MeV are also low relative to all other Heusch points and match the measured data. It should be appreciated that all of the prior measurements of the fusion cross-section from the literature were thin-target measurements with limited angular coverage. Extraction of the fusion cross-section from such measurements required integration of the angle and energy distributions for the individual ERs which introduces uncertainties into the total extracted fusion cross-section. Use of a MuSIC detector provides a direct integrated measure of the fusion cross-section and removes these specific uncertainties.

6.2 Extending the capability of MuSIC detectors

6.2.1 Conceptual framework for simulating MuSIC data

MuSIC detectors provide several advantages over thin-target measurements including being self-normalizing, having high efficiency, and being able to measure a wide portion of an excitation function using one incident beam energy. However, MuSIC detectors also contain a significant disadvantage as compared to thin-target measurements. From the simplest perspective, fusion events are always associated with the discrete anode in which the fusion occurred. Given the atom density of the gas and the number of beam particles incident on that anode the fusion cross-section for each anode is calculated. Along with the cross-section, consideration of the energy lost by the beam prior to the anode allows determination of the energy incident on that anode. In this way, multiple points along an excitation function are simultaneously measured. In this simplest approach of analyzing MuSIC data the fusion cross-section is therefore discretized (binned) based on the anode in which fusion occurs (as described in Section 6.1.3) [94]. Moreover, the corresponding excitation function has error bars in the energy dimension corresponding to the energy loss of the beam in a single anode. These broad energy error bars diminish the observation of fine structure in the excitation function of the reaction being studied [99]. In addition to the wide energy error bars which result from the simple analysis, no information about the evaporation residues (atomic number, energy, etc.) is reported. To move beyond this simple approach we propose to utilize the entire information contained in a MuSIC trace.

In order to overcome these limitations, a more advanced approach to MuSIC data analysis was developed. This approach implements a trace-matching technique which simulates a library of possible fusion traces and then finds the best library match of each experimental trace. In considering simulation of a MuSIC fusion event, it is best to

consider the trace as two separate parts: the energy loss as beam prior to fusion and the energy loss as ER following fusion. As a beam particle traverses the detector it deposits an energy ΔE on an anode corresponding to:

$$\Delta E = \int_{x_1}^{x_2} \left(\frac{dE}{dx} \right)_{Beam} dx$$

where x_1 and x_2 represent the upstream and downstream edges of an anode respectively. When low-energy fusion occurs, amalgamation of the projectile and target nuclei produces a compound nucleus that de-excites via neutron and charged-particle evaporation on the timescale of 10^{-20}s. The resulting evaporation residue (ER) causes ionization in the gas based on its characteristic specific ionization. For the anode on which the fusion occurs at position x, the energy deposit becomes:

$$\Delta E = \int_{x_1}^{x} \left(\frac{dE}{dx} \right)_{Beam} dx + \int_{x}^{x_2} \left(\frac{dE}{dx} \right)_{ER} dx$$

By simulating traces for all possible ERs and comparing these traces with those experimentally observed, some localization of the fusion position can be achieved. In particular, the position at which fusion occurs is most closely related to the ΔE of the first anode which contains energy loss caused by the ER. If the trace were a electronic signal, this would be analogous to the risetime. By performing the trace-matching we are finding not only the best match to each trace's 'risetime', but also to each trace's 'amplitude' and 'integral'. The trace's 'amplitude' is closely related to the Bragg peak of the ion's energy loss and provides information about the ion's atomic number. Similarly, the trace's 'integral' is a direct measure of the ion's total energy. By performing the trace-matching analysis, access is gained not only to a more accuracte localization of the fusion position, but also to other ER characteristics including atomic number and total energy.

6.2.2   Simulation of fusion in MuSIC@Indiana

Guided by simulated traces [99] previous MuSIC measurements have extracted reaction cross-sections for (α,p) and (α,n) reactions. Known limitations in the simulation of the traces however restricted the comparison to only a qualitative description. Moreover, describing fusion traces accurately is complicated by the wider range of atomic and mass number of the reaction products as compared to (α,p) and (α,n) reactions. Past simulations of fusion in MuSIC detectors has been hampered but the aforementioned difficulties preventing the extraction of more detailed information on the fusion [94], namely uncertainties in energy loss calculations.

In order to execute a trace-matching analysis of MuSIC experimental data, it is necessary to accurately simulate MuSIC events for putative ERs. In the approach we have adopted, accurate *in situ* measurement of energy loss for multiple ions in the detector gas together with energy loss calculations provides the necessary reference library for extracting an improved description of fusion. To demonstrate the effectiveness with which the spatial localization of fusion can be achieved this technique was performed on the same ^{18}O+^{12}C data for which results are shown in Section 6.1.4. To start, simulation of ^{18}O beam at E_{lab} = 55 MeV impinging on CH_4 gas at 150 Torr was performed in order to compare to the experimental data.

The flowchart for simulating MuSIC@Indiana events is shown in Figure 6.9a. In the first step, range tables are created using the energy loss program SRIM [132], with a unique range table for both the beam as well as each possible ER. For each ion calculated, the energy spans the interval from 1 keV to 100 MeV with consecutive energies differing by less than 15%. Within this energy range, to interpolate between calculated values of the energy, a spline fit is employed. Before explaining the remainder of the steps in the flowchart (Figure 6.9a), as the range determination is a critical element in the analysis,

a)

Create SRIM range tables

Scale SRIM ranges to match measured ranges

Select residue characteristics: Z, A, E_{ER}, Θ, & D

Given the ER total range (R_T), find the endpoint from the starting location (D)

Calculate the distance from the endpoint to the front of each preceding anode ($R_{A(I)}$)

Using the $R_{A(I)}$ values, find the energy at each anode edge ($E_{A(I)}$)

Calculate the energy loss for each anode, $\Delta E_{A(I)} = E_{A(I)} - E_{A(I+1)}$

Loop to next ER

b)

R_7
R_8
R_9
R_{10}
R_{11}

Beam

D

R_T

0 ... 5 6 7 8 9 10 11

FIGURE 6.9: Panel a: Flowchart for the simulation of fusion events for MuSIC@Indiana events. Panel b: Schematic diagram illustrating the simulation of a fusion event. The location of fusion inside the detector is given as D and relevant distances from the fusion location are given as $R_A(I)$.

it is necessary to describe the procedure for determining the range of different ions in further detail.

It is well established that energy loss values in SRIM when compared to other energy loss programs or experimental data often exhibit uncertainties of approximately 10% [94, 99]. Other energy loss programs also exhibit comparable uncertainties. To minimize this uncertainty, the range of specific ions in the detector gas were measured. These measured ranges were used, as described below, to scale the calculated SRIM ranges as indicated in the second step of Figure 6.9a. Low-intensity beams of ions with $8 \leq Z \leq 14$ were accelerated by the 10 MV tandem accelerator at Notre Dame University and impinged on MuSIC@Indiana. In addition, multiple isotopes of both oxygen and magnesium nuclei were also measured to quantify the isotopic impact on energy loss. To measure the $\Delta E/\Delta x$ a silicon surface barrier detector was attached to a linear-motion vacuum feedthrough and inserted into the active area of MuSIC@Indiana. The results of these measurements are presented in Figure 6.10. A clear separation of the energy loss curves for the different Z is observed in Figure 6.10, while the separation between different isotopes of the same element is, as expected, significantly smaller.

To extract the experimental range of each isotope, the correlation between measured energy and position in the detector is plotted in Figure 6.11. The distance is taken relative to the upstream edge of the detector. For each nuclide the measured correlation is fit with a second degree polynomial. As can be seen in Figure6.11, the parameterization provides a good description of the data even for all ions independent of whether they stopped in the detector gas. These fits are extrapolated to the stopping point, e.g. zero remaining energy, to find each isotope's experimental range. The relationship between the SRIM range and the experimental range is defined as:

$$R_{EXP} = Slope * R_{SRIM}$$
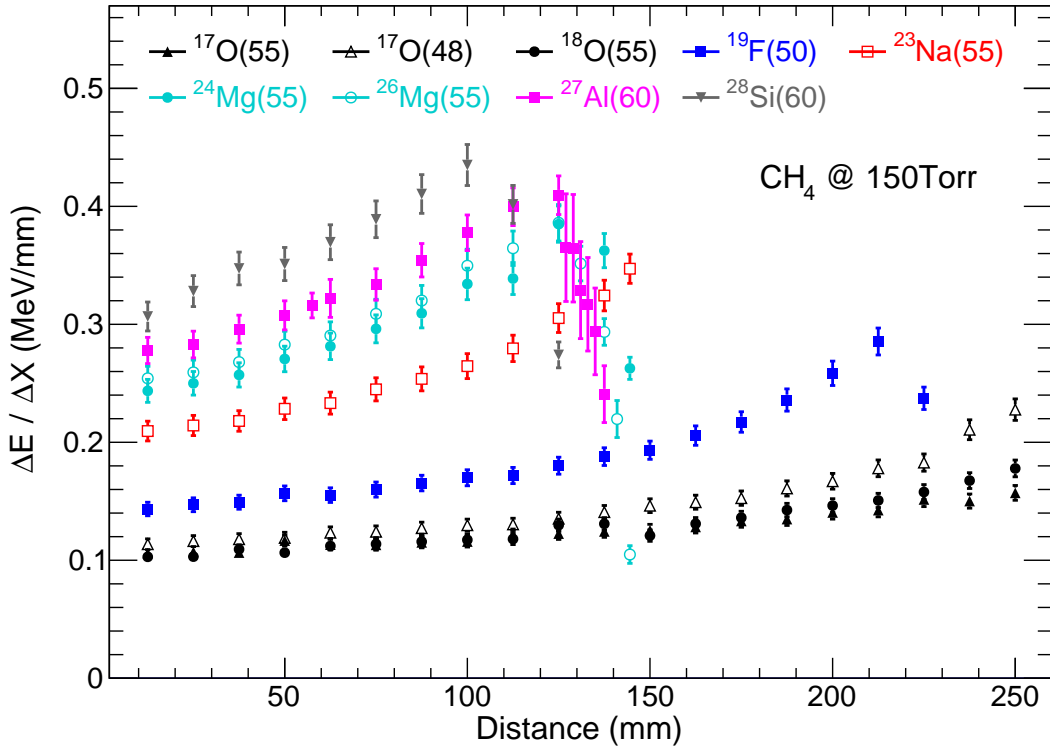
FIGURE 6.10: Measured energy loss for several isotopes including potential residues. Listed along each isotope is the incident energy in MeV.

TABLE 6.1: Parameters for scaling SRIM ranges

Isotope	Slope
^{17}O	1.1905
^{18}O	1.1542
^{19}F	1.1687
^{23}Na	1.1472
^{24}Mg	1.1444
^{26}Mg	1.1368
^{28}Si	1.1803

No offset is used because an ion with zero energy must have a range of zero. For a given nuclide, the slope is defined by the point (R_{SRIM}, R_{EXP}) at the upstream edge of the detector. The slope for all measured nuclides is given in Table 6.1. For any nuclide in the simulation without an experimentally measured range, the SRIM range is scaled using a slope taken as the average slope of all measured nuclides.
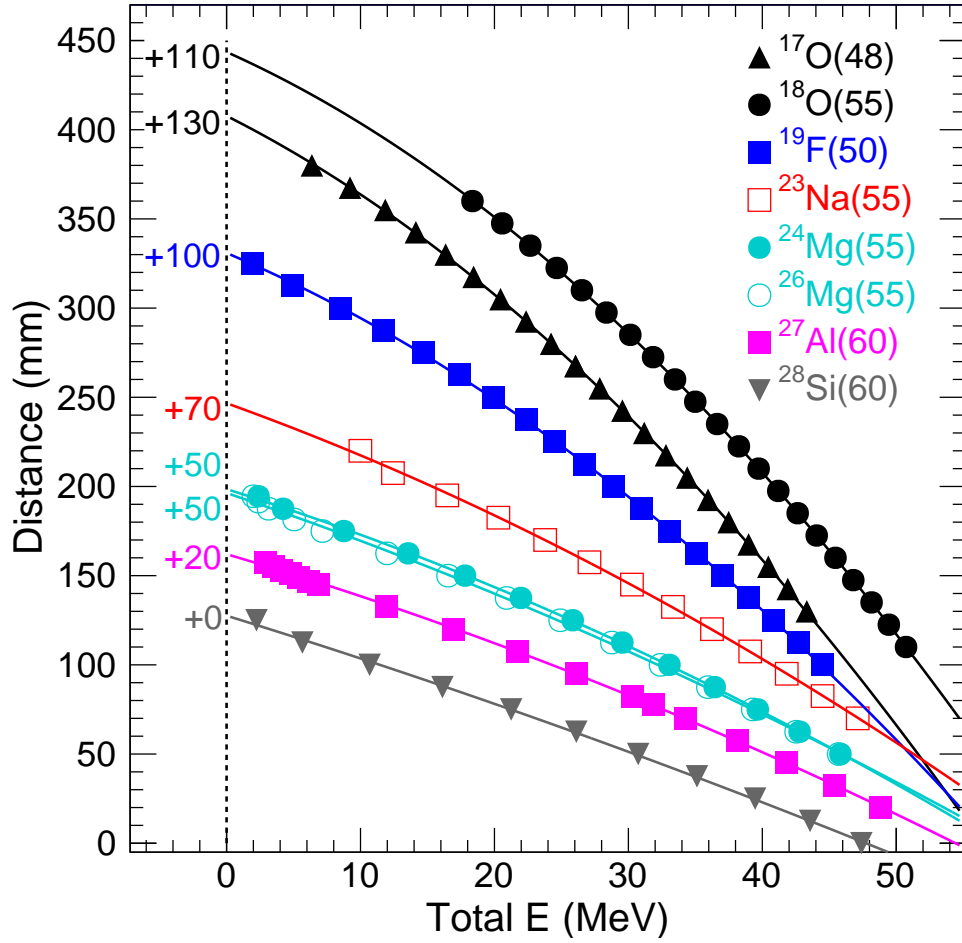
FIGURE 6.11: The distance from the front of MuSIC@Indiana as a function of the energy measured by the SBD for all measured ions. Listed in parenthesis is the incident energy in MeV. For clarity the curves are vertically offset by the numbers indicated on the left.

The energy loss for the beam in MuSIC@Indiana is shown in Figure 6.12. The average experimental beam trace (dashed black line) is compared to the simulated beam trace from SRIM (solid blue line). The simulation produces a trace which is systematically 15-35% higher in ΔE than what is measured by MuSIC@Indiana. After scaling, the simulated beam trace (solid red line) matches the experimental trace to within 4% ($\sim$60 keV) for all anodes, showing the accuracy of the range scaling.

Once the SRIM ranges have been appropriately scaled for the beam and the residues, the first step in simulating a fusion event is to select the characteristics of the fusion event
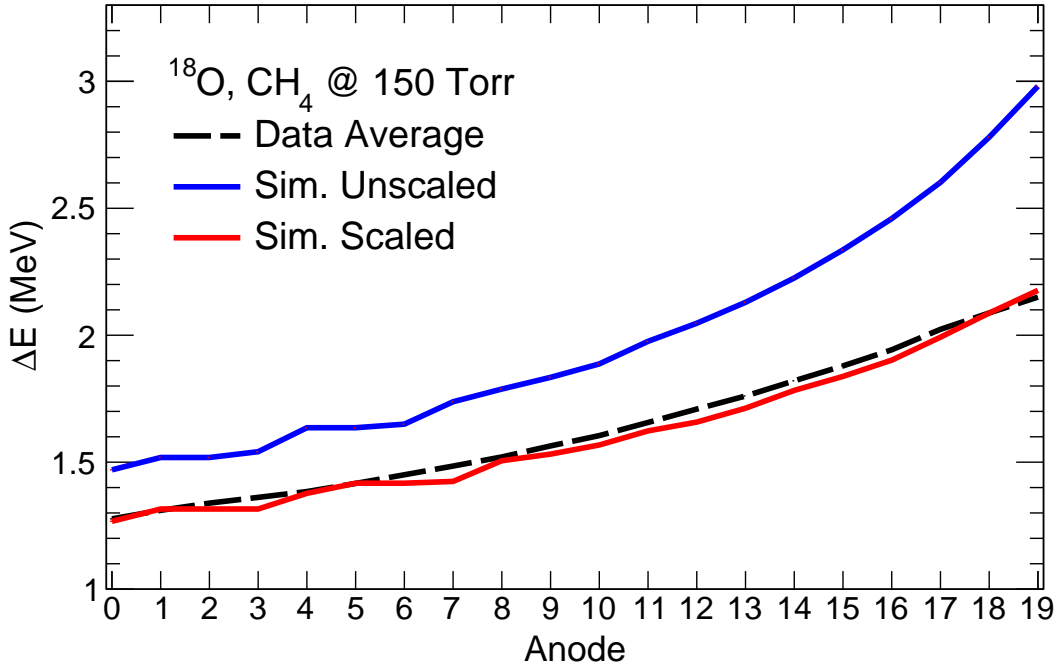
FIGURE 6.12: The average experimental beam trace (dashed black line) is presented along with a simulated beam trace before (solid blue line) and after (solid red line) scaling the SRIM ranges.

which will determine the energy loss within MuSIC@Indiana. The energy loss for each event is characterized by the ER atomic number (Z), mass number (A), energy (E_{ER}), and angle (θ), as well as the location at which the simulated fusion occurs (D).

Potential ERs for the reaction of interest, $^{18}O+^{12}C$, are determined using the statistical decay code evapOR [84]. All potential isotopes with a probability above 0.1% in evapOR are simulated, with the ER characteristics presented in Table 6.2. The angle of ER emission ranges from Θ_{min} to Θ_{max} with a 5° spacing. Because the ER distributions manifest a narrow range in Θ, its impact on the energy deposit in an anode is negligible. The energies of the ER, E_{ER}, simulated are also guided by evapOR. They are chosen to range from 5 to 45 MeV with a 1 MeV spacing. The location of fusion (D) is simulated as spanning the active detector length (250 mm) in increments of 0.5 mm. Although some less likely events are simulated, this method minimizes the influence of inaccuracies in

TABLE 6.2: ER characteristics used for creating the simulated library.

Z	A_{min}	A_{max}	$\Theta_{min}(°)$	$\Theta_{max}(°)$
10	19	23	0.0	25.0
11	22	26	0.0	20.0
12	23	28	0.0	20.0
13	26	29	0.0	15.0
14	26	29	0.0	15.0

evapOR on the library.

Once these parameters are assigned for a specific library event, the total range of the ER (R_T) is determined using the range table. The distance from the endpoint to the front of each preceding anode ($R_{A(I)}$) is calculated as illustrated in Figure 6.9b. The energy of the ER at the front of each anode ($E_{E(I)}$) can then be determined using these distances and the range table. Lastly, the energy loss over a single anode ($\Delta E_{A(I)}$) is calculated as $\Delta E_{A(I)} = E_{A(I)} - E_{A(I+1)}$. Prior to the point of fusion, D, the energy loss is assigned to be that of simulated beam.

6.2.3 Trace-matching MuSIC@Indiana data analysis

With the library of simulated traces defined, the procedure for analyzing a fusion event is depicted in the flowchart presented in Figure 6.13. From the experimental event data, fusion events are distinguished from un-reacted beam, proton capture, and two-body scattering as described in Section 6.1.3. In essence, a trace is categorized as corresponding to fusion based upon it surpassing a minimum ΔE threshold above ΔE_{Beam} and having a range consistent with an ER. At this point each fusion event is associated with the anode, $A_{Threshold}$, for which the minimum threshold is surpassed. In the trace-matching analysis the position of the fusion is localized by comparing the measured MuSIC@Indiana trace to all library events in a 'trace-matching' process. The span of ER energies considered is limited by summing the ΔE from $A_{Threshold}$ to A_{19}. Only library events with energies

within 3 MeV of this energy are considered. The deviation of the experimental event from a library event is assessed through the calculation of the quantity η^2, defined as:

$$\eta^2 = \sum_{Anodes} (\Delta E_{A(I)}^{exp} - \Delta E_{A(I)}^{sim})^2$$

The library event with the minimum η^2 is identified and subsequently used as a reference for calculating residue characteristics. Each fusion event characteristic (D, Z, E_{ER}, A, and Θ) is calculated to be the average value for all library events within 0.2 of the minimum η^2. In general, traces for library events above $\eta_{min}^2+0.2$ were observed to deviate consistently from the data trace beyond the level of the detector noise. As such, events with a η^2 greater than 0.2 above η_{min}^2 are not included in the calculation of the average D, Z, E_{ER}, and A.

A representative experimental fusion trace (blue) is presented in Figure 6.14a, alongside the trace of its associated η_{min}^2 library event (red). The η_{min}^2 event shows excellent agreement with the data trace. To examine the differences between the two, the deviation of the η_{min}^2 library event from the experimental fusion trace is depicted in Figure 6.14b as the red line. Its deviation from the data at the peak, anode 7, is ~ 60 keV well within the energy uncertainty of the ΔE signal. A measure of what represents a reasonable deviation is realized by examining the distribution of all beam events represented by the error bars on the average beam trace (black, FWHM ~ 200 keV) shown in Figure 6.14a. In addition, Figure 6.14a shows the trace for the library event at $\eta_{min}^2+0.2$ (green). This trace is also in good agreement with the data and is within the uncertainty on the ΔE signal observed during the experiment.

For the data event shown in Figure 6.14a, the dependence of the η^2 value as a function of D and each of the ER characteristics Z, E_{ER}, and A is shown in Figure 6.15a-d, respectively. Also presented in Figure 6.15a-d are the mean and RMS values of each
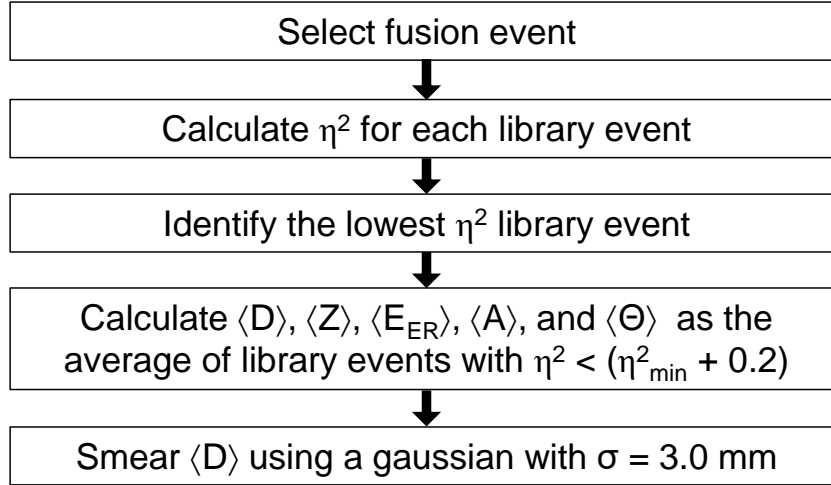
FIGURE 6.13: Flowchart depicting the logic of the trace-matching analysis implemented.

distribution. The width of the D distribution, 0.893 mm, is much smaller than a single anode width of 12.5 mm. This indicates that one can achieve sub-anode resolution on the location of fusion in MuSIC@Indiana. From the value of D the energy at which fusion occurs can be directly calculated allowing a higher granularity determination of the fusion excitation function – one that is not determined by the anode geometry of the detector. As shown in Figure 6.15b, the Z distribution is well-defined with most events corresponding to a single Z value. Similarly, Figure 6.15c shows a narrow distribution in E_{ER} with all events falling within 0.5 MeV of the average. As observed in the $\Delta E/\Delta x$ measurements presented in Figure 6.10, the energy loss has a slight dependence on A. This weak dependence provides a poor discrimination capability for A and is reflected in Figure 6.15d by a relatively broad A distribution spanning 4-5 masses.

The energy loss values in the library do not account for the variation in ΔE experimentally measured due to both the Fano factor of the gas and the electronic noise. This deficiency can be framed in terms of an uncertainty in the extracted value of D. The average D is smeared using a Gaussian distribution centered at the averaged D value with $\sigma_D = 3.0$ mm as indicated in the last step of Figure 6.13.

106
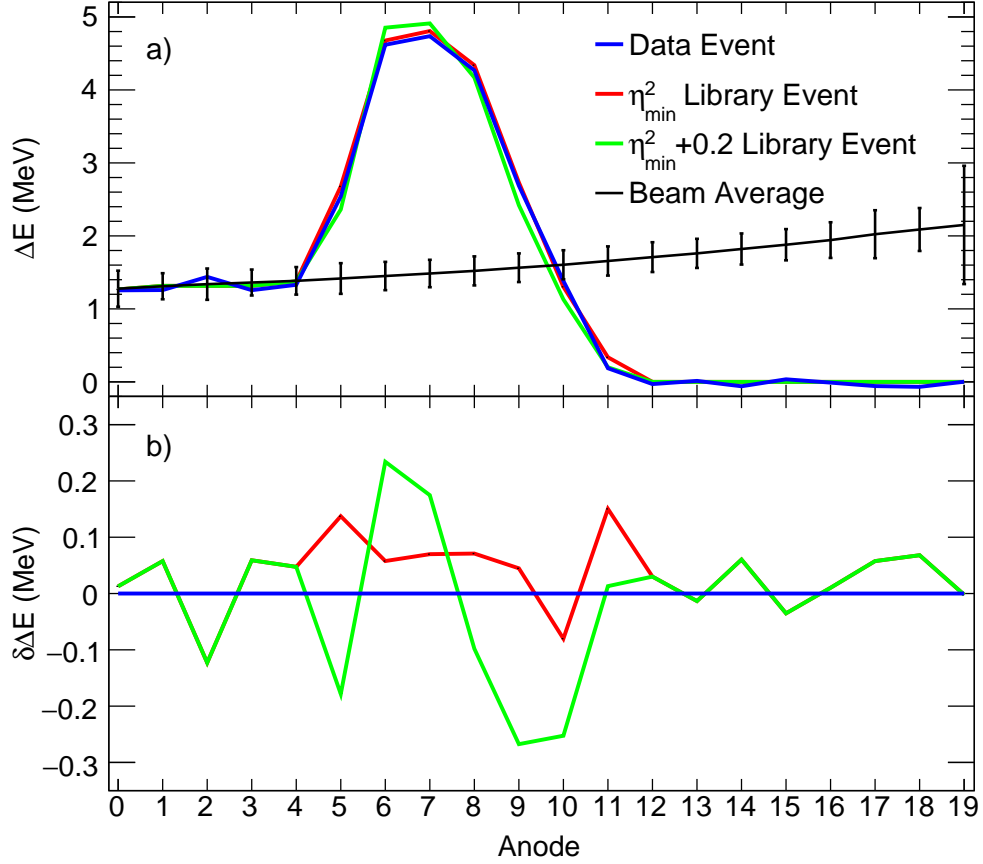
FIGURE 6.14: An experimental MuSIC@Indiana trace with both the library trace of minimum η^2 and the library trace of minimum $\eta^2+0.2$ is shown in panel a. The average beam behavior is also shown for reference with error bars representing the FWHM of the noise seen in the detector. Panel b shows the deviation of both library traces from the experimental event.

6.2.4 Results of trace-matching analysis

The analysis technique described in Section 6.2.3 was applied to the ^{18}O+^{12}C reaction for data collected using MuSIC@Indiana. The experiment was performed at the University of Notre Dame's Nuclear Science Laboratory. A beam of ^{18}O^{6+} ions was accelerated by the 10 MV tandem accelerator to E_{lab} = 55 MeV and bombarded MuSIC@Indiana filled with 150 Torr of CH_4.

As demonstrated in Figure 6.15b, the trace-matching analysis allows for the extraction of residue Z with high confidence. The experimental Z distribution as a function of
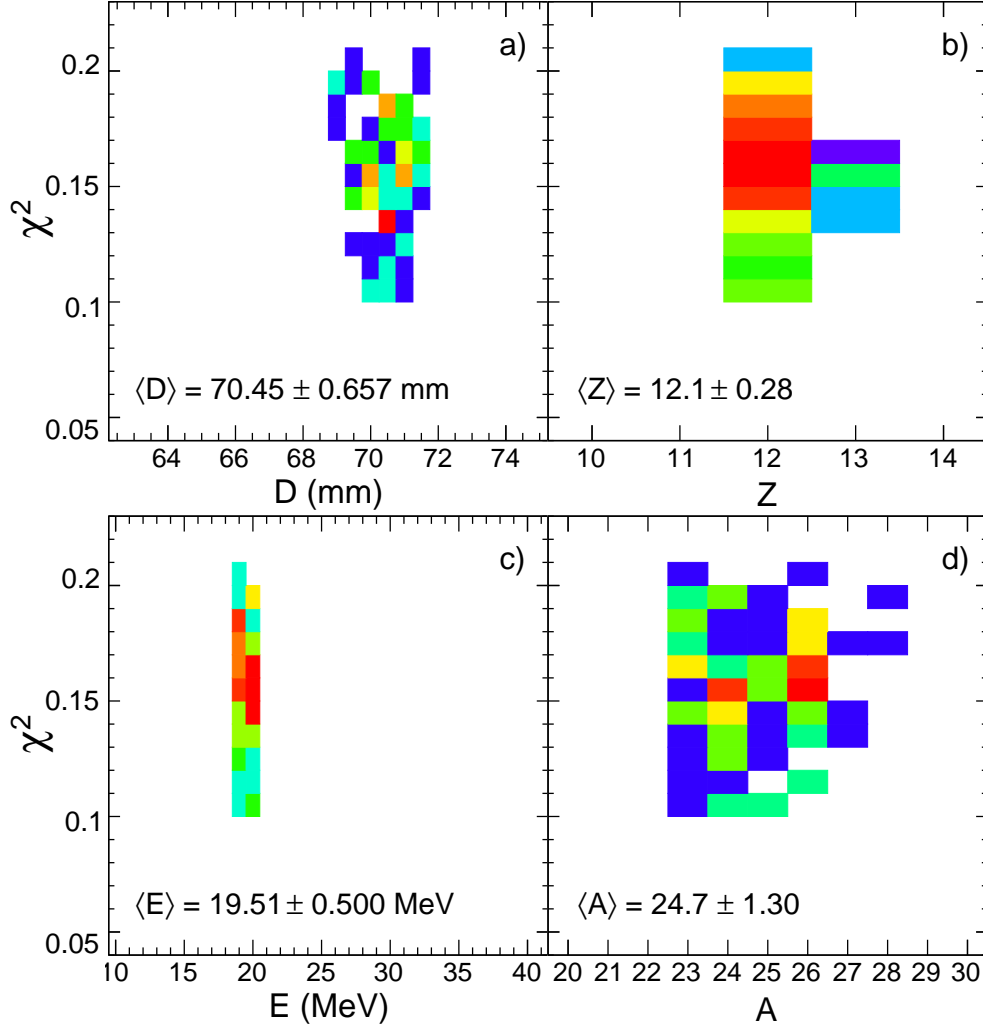
FIGURE 6.15: η^2 distributions for a single data event as a function of the D, Z, E_{ER}, and A are shown in panels a-d, respectively. Each variable is presented with the mean and root mean square values of the distribution.

$E_{C.M.}$ for $^{18}O+^{12}C$ is presented in Figure 6.16. A clear trend is observed as a function of $E_{C.M.}$, with Z≤12 dominating the distribution at higher energies and a shift to Z≥13 dominating at lower energies. This trend is consistent with a previous investigation of the α-emission cross-section from the compound nucleus [139]. A near 100% probability for α-emission at $E_{C.M.}$ = 14 MeV was observed, with the probability falling off substantially for lower incident energies [139]. The trend observed in Figure 6.16 indicates good agreement with these results. The Z distribution as a function of $E_{C.M.}$ has been previously
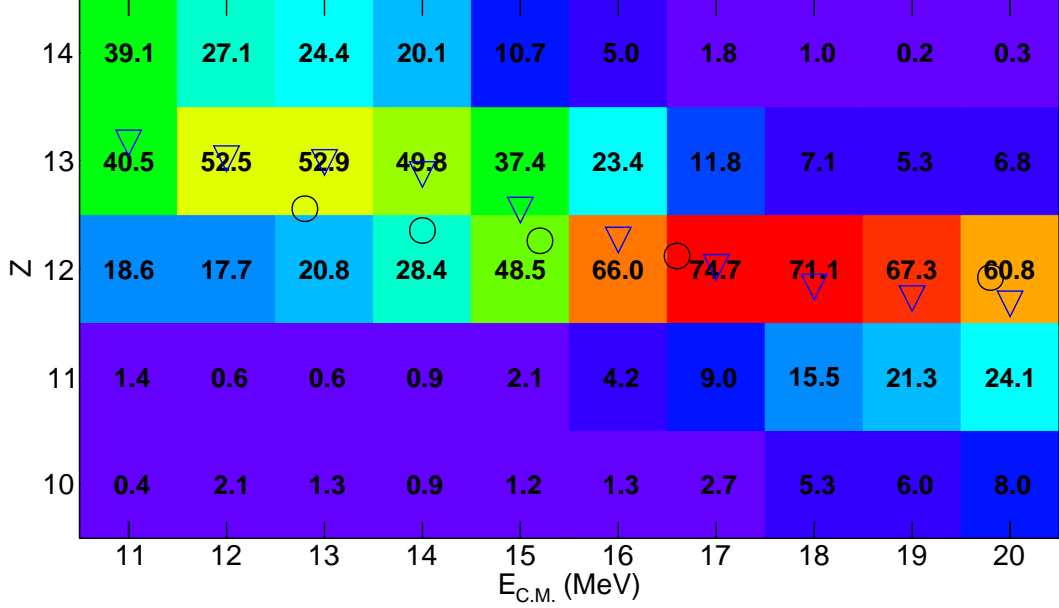
FIGURE 6.16: Fusion evaporation residue Z-distribution as a function of $E_{C.M.}$ for $^{18}O+^{12}C$. Numbers indicate the elemental percentage for a given bin in $E_{C.M.}$. The $\langle Z_{ER} \rangle$ from this work is shown as the open triangles while $\langle Z_{ER} \rangle$ from [137] is indicated by the open circles.

reported [137]. The $\langle Z_{ER} \rangle$ reported in [137] is shown in Figure 6.16 as the open circles. In comparison, the $\langle Z_{ER} \rangle$ for the current work is portrayed as the open triangles. The good agreement of the measured $\langle Z_{ER} \rangle$ in the current work as compared to prior measurements [137, 139] suggests that the current analysis is correctly identifying the $\langle Z_{ER} \rangle$.

Presented in Figure 6.17a are the results of the trace-matching analysis binned at the one-anode level ($\Delta D = 12.5$ mm), alongside the same data set as analyzed according to Section 6.1.3. One should note that in both cases the represented error bars in σ_F are entirely statistical and the error bars in $E_{C.M.}$ are $\sim$800 keV. All points on the two excitation functions agree within the error bars and no systematic trend is observed. The minor differences between the two analyses are due to the reshuffling of events for which fusion occurs near an anode edge. In the simple analysis, a threshold must be set for each anode which designates an event as being fusion in that anode. This threshold is dependent on the noise in the detector. As such, fusion events which occur deep in an

anode may not have sufficient energy loss to be above threshold and will not be identified as fusion-like until the subsequent anode. For the entire excitation function this is a small effect as each anode gains events from the preceding anode and loses events to the following anode. This results in a 'smoothing' of the excitation function as the anode edges do not provide a sharp cutoff for binning in the simple analysis. In contrast, the trace-matching analysis properly identifies the location of these events near an anode edge and assigns them to the correct energy in the excitation function.

The same trace-matching analysis is presented in Figure 6.17b binned at the half-anode level (ΔD = 6.25 mm). Increasing the number of points by a factor of two reduces the energy error bars by a factor of two, $\sim$400 keV. Correspondingly, on average each datapoint has half the statistics, which only increases the error bars in σ_F by a factor of $\sim$1.4. As the uncertainty in both energy and cross-section are relevant to the accurate determination of the fusion excitation function, this significant improvement in energy uncertainty at the cost of a modest worsening in the cross-section determination is an overall improvement in the determination of the excitation function. Further reduction in the energy uncertainties evident in Figure 6.17b are not warranted given the statistical uncertainties of the measurement. Overall, this excitation function also matches the results from Section 6.1.4. Some structures appear to be emerging, notably small peaks at $E_{C.M.} \sim$ 15.3 and 16.5 MeV.

To better understand the nature of these structures, this excitation function is plotted against literature data in Figure 6.18. The literature data matches the measured data well, in particular because of the non-smooth behavior observed for the current work. Below $E_{C.M.}$ = 14 MeV, this work is in good agreement with all three literature datasets. At energies above $E_{C.M.}$ = 15 MeV where the non-smooth behavior is most pronounced, the measured data agrees with Heusch and maps out oscillations which are common in light fusing systems [97, 140, 141]. Inspection of Heusch together with the trace-matched

MuSIC@Indiana data indicates the presence of oscillations, most prominently a broad structure between 16 and 18 MeV. While the Heusch data is consistent with these oscillations, taken on its own it does not have enough definition of the excitation function in this energy range to observe these structures definitively. This comparison of the literature and the MuSIC@Indiana data highlights an inherent advantage of measuring fusion with a MuSIC detector and employing the trace-matching analysis. With this analysis, the energies at which fusion is measured are decoupled from the anode segmentation, effectively providing a measurement of the fusion excitation function that is continuous in energy and with error bars comparable to thin-target measurements. The current analysis also underscores the importance of improving the energy resolution of an excitation function for locating narrower structures. While this work provides evidence for oscillatory structure in the $^{18}O+^{12}C$ excitation function, the magnitude of these oscillations is comparable to the present statistical uncertainties in the measured cross-section. As such, further measurements which acquire higher statistics should be performed in order to confirm these results.
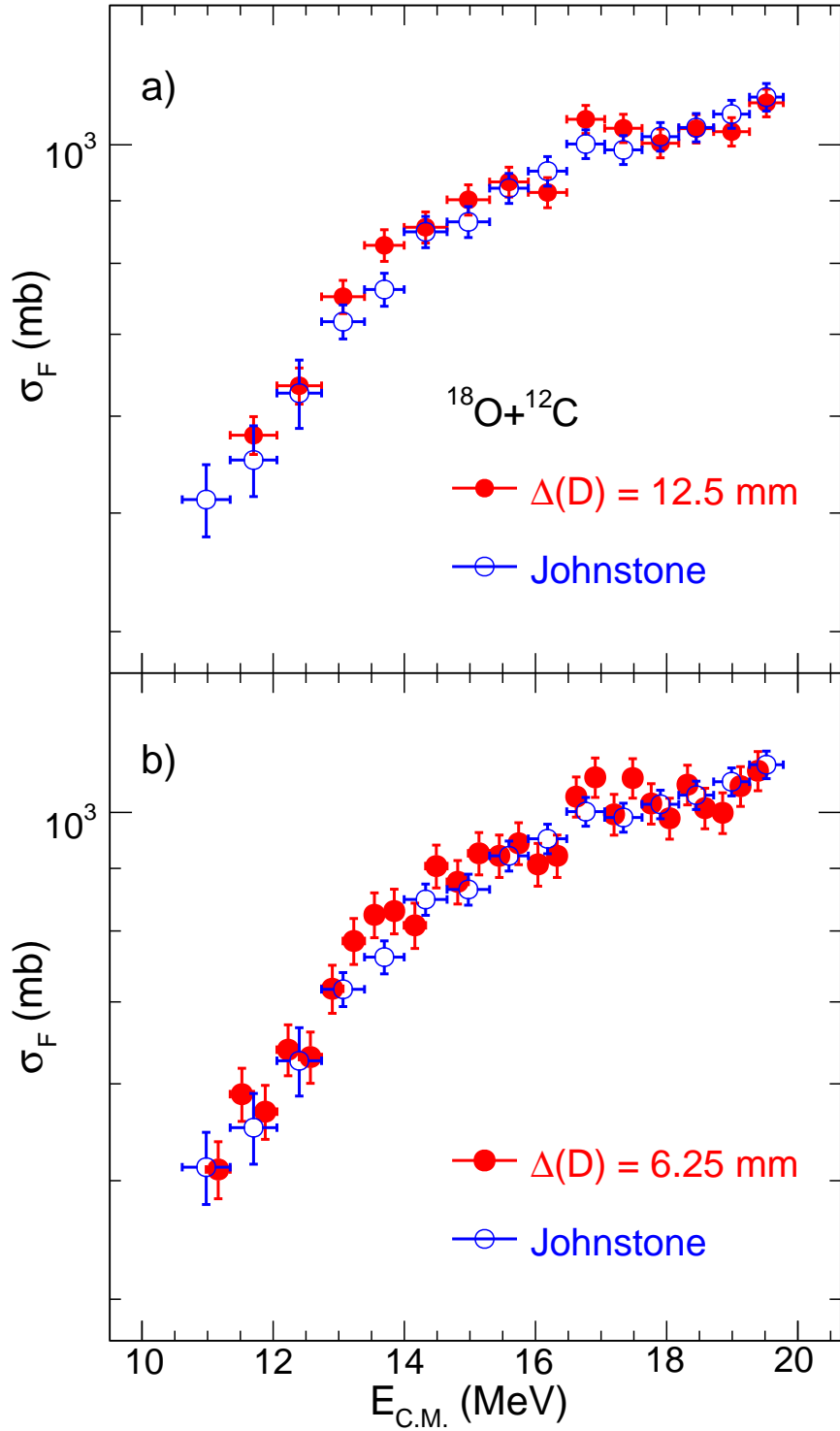
FIGURE 6.17: The measured fusion excitation function of $^{18}O+^{12}C$ extracted using the trace-matching analysis technique together with the published excitation function of the same data from [142]/Section 6.1.4. The extracted excitation function is shown binned at the 1-anode (a) and half-anode (b) levels.
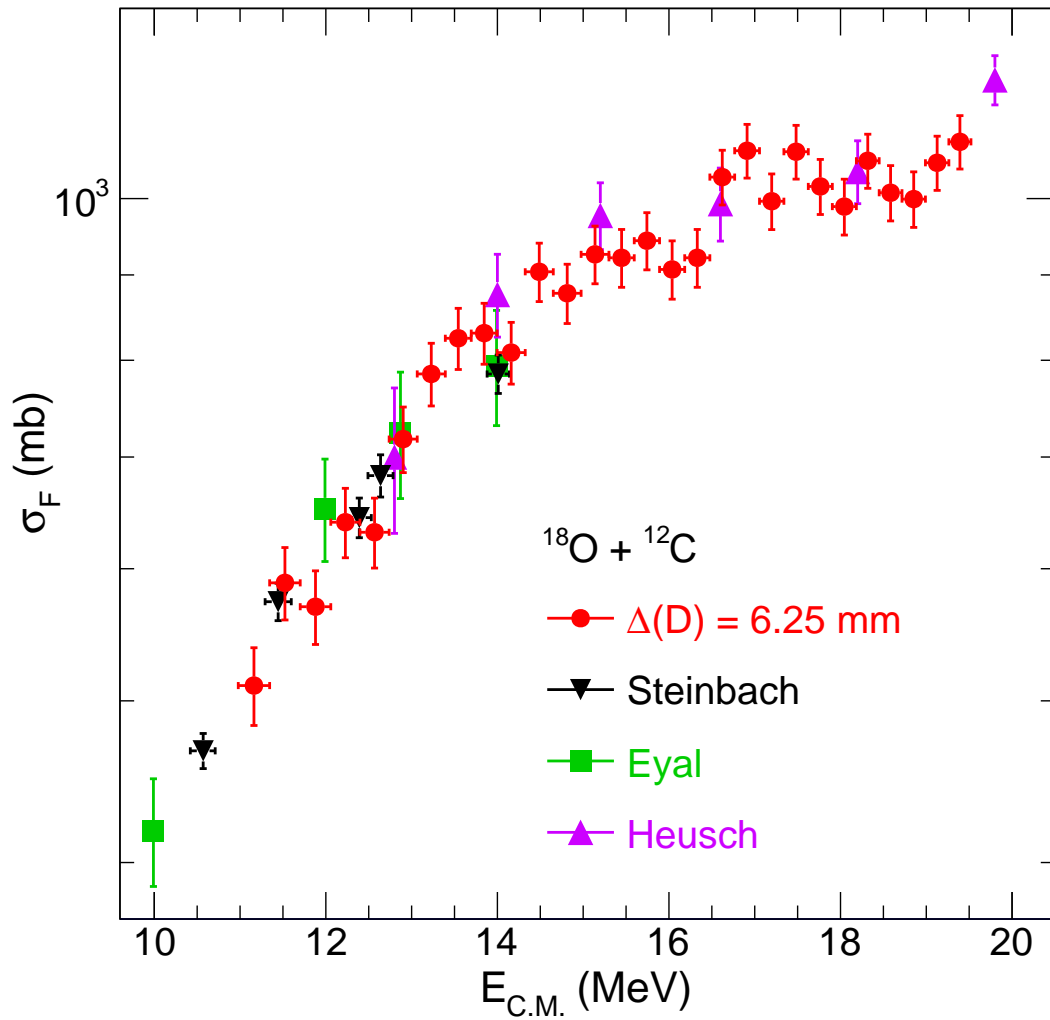
FIGURE 6.18: Comparison of the high resolution fusion excitation function of $^{18}O+^{12}C$ obtained with the trace-matching analysis technique with the thin-target data sets of Steinbach [79], Eyal [101], and Heusch [137].

Chapter 7

Summary and outlook

7.1   Mid-mass fusion measurements near shell closures

Previous measurements of the fusion excitation functions for ^{39,47}K+^{28}Si showed large enhancement of the neutron-rich isotope relative to the stable counterpart [4]. Both ^{39}K (N=20) and ^{47}K (N=28) have closed neutron-shells. To expand measurement of the potassium isotopic chain away from closed neutron-shells, the fusion excitation functions for ^{41,45}K+^{28}Si were measured. Additional measurements were made of ^{36,44}Ar to help understand the role of the unpaired proton in potassium. Measurements were conducted at MSU's NSCL ReA3 reaccelerator using the ETOF technique.

In addition to the intended measurements, analysis of the data allowed extraction of the fusion excitation functions for the measured isotopes on contaminant oxygen in the target. Systematic measurement of the fusion excitation functions for ^{39,41,45,47}K + ^{16}O and ^{36,44}Ar + ^{16}O have yielded surprising results. Comparison of the different excitation functions was done in a reduced space which accounts for the systematic changes in the size of the reacting nuclei as well as their Coulomb barrier. The open neutron-shell nuclei of ^{41,45}K manifest larger reduced fusion cross-sections than the closed neutron-shell isotopes ^{39,47}K. This result indicates that the additional binding due to the closed-shell structure is present at the saddle point. In all cases considered, the São Paulo fusion model using the systematic densities overpredicts the measured fusion cross-sections. Use of more realistic density distributions from DHB calculations resulted in a reduction of the predicted fusion cross-section as compared to the systematics. For the open-shell nuclei, the use of these more accurate ground-state densities in the São Paulo fusion model

provided a reasonable description, particularly for the K isotopes. For the closed-shell nuclei, however, use of the DHB densities still overpredicts the measured cross-sections, particularly above the barrier.

The extracted cross-sections on the ^{28}Si target show results similar to reaction on the ^{16}O target. At above-barrier energies a slight enhancement in the reduced excitation functions for open-shell projectiles is observed relative to the closed-shell projectiles. At energies below the barrier this enhancement is markedly increased. Additional insight was gained by plotting the reduced excitation functions according to the closest closed neutron-shell. For the nuclei near the N=20 closed shell (^{39}K, ^{41}K, and ^{36}Ar), the ^{41}K and ^{36}Ar excitation functions overlap and are both enhanced relative to the ^{39}K. These results seem to indicate that the presence of two holes below a closed-shell is effectively the same as the presence of two particles above the closed-shell in determining the fusion cross-section. Similarly in the vicinity of the N=28 shell (^{47}K, ^{45}K, and ^{44}Ar), the open-shell ^{45}K and ^{44}Ar excitation functions overlap and exhibit cross-sections larger than the closed-shell ^{47}K. This agreement between the open-shell argon and potassium nuclei seems to indicate that the unpaired proton in potassium has little effect on fusion in the measured energy range. Calculations of the fusion cross-section with the São Paulo model using DHB densities provided a reasonable description of the ^{39,47}K excitation functions, but drastically underpredicted the cross-sections for open-shell nuclei below the barrier. Inclusion of low-lying states of the ^{28}Si target improves the agreement of the calculation with the measured ^{39,47}K cross-sections (with particular improvement below the barrier), but still fails to describe the measured below-barrier cross-sections of the open-shell nuclei.

Use of the reduced excitation functions allowed comparison of the reactions on ^{16}O to the reactions on ^{28}Si on a projectile-by-projectile basis. In the energy interval measured for both targets, the excitation function for reaction with ^{16}O is in reasonable agreement

with the excitation function for reaction with ^{28}Si for all projectiles. This indicates that, for above-barrier energies, ^{16}O and ^{28}Si do not differ significantly once size and barrier effects have been accounted for. At the lowest measured oxygen energies a slight dip in the oxygen excitation functions relative to the corresponding silicon excitation functions is observed. As ^{16}O itself is a closed-shell nucleus (Z=8 and N=8), fusion on an ^{16}O target may be suppressed relative to fusion on ^{28}Si. It is difficult to make this claim with strong certainty without having measurements of the excitation functions on oxygen below the barrier where the effects of the closed and open shells are more drastic. These results show the importance of below-barrier measurements to seeing the influence of shell effects on fusion and motivate further measurements on oxygen at sub-barrier energies.

Overall, the measurement of the ^{39,41,45,47}K,^{36,44}Ar+^{28}Si,^{16}O excitation functions have provided strong evidence that neutron-richness is not the sole factor in determining the near-barrier fusion cross-section for mid-mass systems. There is now strong evidence that the binding energy of the fusing nuclei is more important than deformation in determining the fusion cross-section for mid-mass nuclei. Measurement of ^{40,44,48}Ca+^{28}Si would provide insight into what effect the addition of a single proton to potassium (and thereby closure of the proton-shell) would have on the excitation function. As ^{40,44,48}Ca are all stable, production of these beams with high intensity should be achievable at several accelerator facilities allowing for measurement of these systems with ETOF. These measurements may also have important implications for super-heavy element (SHE) production. A common target in reactions to produce SHEs is ^{48}Ca, however the experimental evidence discussed in this thesis suggests that neutron-rich isotopes away from closed-shells may provide a better target for these reactions.

7.2 High-quality target production

The measurement of the mid-mass Ar and K + ^{28}Si fusion excitation functions by ETOF was impeded by the presence of contaminant oxygen in the form of a silicon oxide in the target. The foils used in these measurements contained $\sim$40% oxygen throughout the foil. In the final analysis, the intended excitation functions as well as the additional excitation functions from the data for the reactions on ^{16}O were able to be extracted. Such an outcome is dependent upon the resolution of the ETOF telescopes and the geometry of the detectors which may vary between experiments. In an effort to create improved targets, high-quality thin Si films were produced.

Both ^{nat}Si and isotopically-enriched ^{28}Si foils with a thickness of $\sim$220 μg/cm^2 and a low oxygen content were produced via vapor deposition. The thickness of the foils was characterized using measurements from both a QCM and ^{148}Gd α-particle gauge. These measurements were in agreement to within 0.5% on average, which indicated that the QCM was a reliable measure of the foil thickness during evaporation. In general, RBS thickness measurements were qualitatively consistent with the determined thicknesses. Measurements of elemental abundances using XPS and RBS showed silicon purity to be 87%$-$90% with the primary contaminant being oxygen. An enhanced oxygen content of up to 40% was observed at the foil surface. These foils manifest an approximately 4-fold reduction in the oxygen content as compared to previous foils. This reduced oxygen content reduces a significant source of background thus improving future fusion cross-section measurements.

Foils produced with these procedures were used in the experiment E20022 at Michigan State University's ReA3 reaccelerator facility to measure the reaction ^{28,30,32}Si + ^{28}Si. No significant deterioration in the Si foils has been observed from ambient conditions. However, the foils are fragile and susceptible to breaking if mishandled. The established

117

procedures provide the methodology necessary for creation of additional Si targets if necessary. Should an experiment require different targets, the present target fabrication techniques should be useful as a starting point in the production of high-quality targets of other refractory materials.

7.3 MuSIC@Indiana - towards measurements near the neutron dripline

In trying to understand the nature of neutron-rich matter, the most interesting and valuable measurements of fusion will always be concerned with the most exotic beams. The imminent first beams at next generation radioactive beam facilities such as FRIB will allow measurements to be made closer to the neutron dripline than ever before. The most neutron-rich beams, however, will always be available at low beam intensities. Use of thin-target approaches is impractical for beams with rates lower than $\sim 5 \times 10^3$ particles/s. MuSIC detectors, with their direct measurement of the angle-integrated fusion cross-section and ability to simultaneously measure multiple points on an excitation function, provide an alternative tool for radioactive beam experiments that can efficiently measure fusion excitation functions for beam rates at and below 10^3 particles/s.

In preparation for future experiments near the neutron dripline, a new MuSIC-style detector, MuSIC@Indiana, was developed. MuSIC@Indiana is differentiated from other MuSIC detectors in its ability to precisely insert an SBD into the detector active volume. The SBD enabled the accurate measurement of the beam energy at each anode allowing calibration of MuSIC@Indiana. Additionally, the SBD eliminated the uncertainties associated with energy loss programs in identifying the occurrence of fusion and extracting the fusion excitation function. MuSIC@Indiana was commissioned by the measurement of the $^{18}O+^{12}C$ fusion excitation function at the University of Notre Dame's Nuclear Science Laboratory's 10 MV Tandem Accelerator. An analysis procedure was developed that provided a simple means of discriminating fusion events from proton capture and

two-body scattering events. The effectiveness of this analysis was demonstrated by the good agreement between the extracted excitation function and previously reported cross-sections from thin-target measurements. The quality of the MuSIC@Indiana ^{18}O+^{12}C measurement over a short time interval demonstrated that MuSIC@Indiana is an effective tool for accurate measurement of fusion with low-intensity radioactive beams.

A significant drawback in using MuSIC detectors is the challenge in localizing the position of fusion within the detector. This results in wide error bars in the energy dimension for the measured excitation function. To improve the use of MuSIC detector in measuring fusion, a new approach for analyzing fusion data from a MuSIC detector was developed. This analysis, which relies on matching the measured ΔE in a MuSIC trace with simulated energy loss curves, successfully extracted a high resolution fusion excitation function. Critical to this analysis was development of an energy loss library which necessitated accurate energy loss measurements for the ions of interest. Using a library for ^{18}O+^{12}C a trace-matching analysis of experimental data was performed. As a result of this analysis the evaporation residue Z-distribution was additionally obtained along with a localization of the fusion position at the sub-anode level. The resulting high resolution fusion excitation function obtained is comparable to those obtained for thin-targets but is substantially more efficient.

The commissioning of MuSIC@Indiana has enabled further investigation of the ^{X}O+^{12}C isotopic chain. A recent investigation has shown a large above-barrier enhancement for the fusion cross-section of ^{19}O+^{12}C relative to ^{16}O+^{12}C [6]. This enhancement is not well described by either static (RMF-SP) or dynamical models (TDHF). A potential source of this enhancement is the last neutron in ^{19}O which is unpaired. To delve further into understanding the role of an unpaired neutron in the fusion, the ^{17}O+^{12}C excitation function has been measured with MuSIC@Indiana. The analysis of this data has been finalized and publication is forthcoming. To extend the investigation of this isotopic chain

119

an experiment has been approved to run at GANIL using MuSIC@Indiana to measure the ^{19,20}O+^{12}C excitation functions.

These proposed MuSIC@Indiana measurements with ^{19,20}O+^{12}C at GANIL together with the anticipated measurement of ^{21,22}O+^{12}C at FRIB provide a comprehensive and systematic dataset for understanding fusion of neutron-rich light nuclei. Together with the proposed ETOF measurements of ^{40,44,48}Ca+^{28}Si, these data will build upon the initial examination of the influence of shell structure on fusion of neutron-rich nuclei presented in this thesis.

Appendix A

Electonics
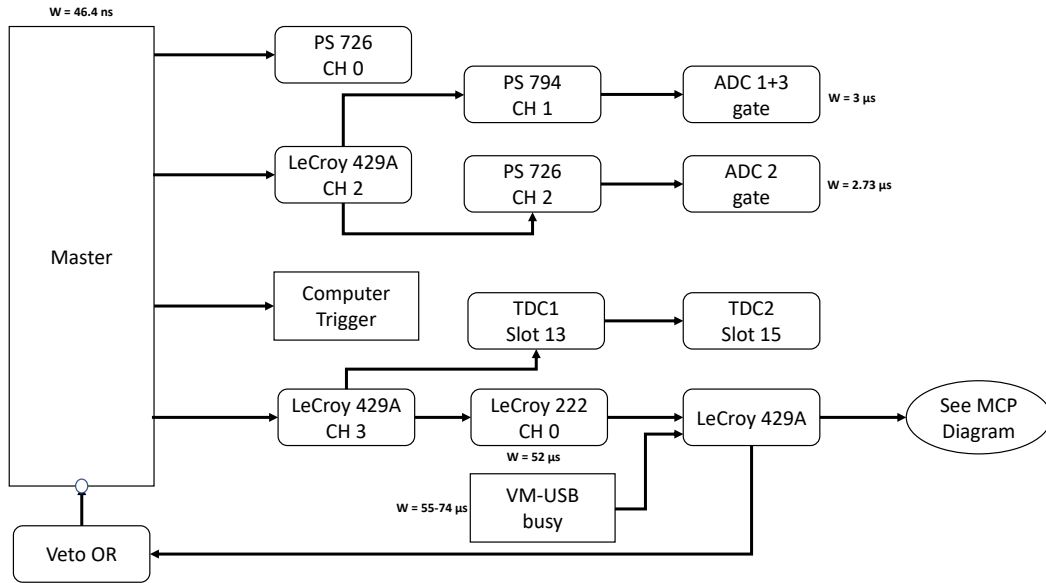
FIGURE A.1:   Electronics diagram for the master trigger in E17002.
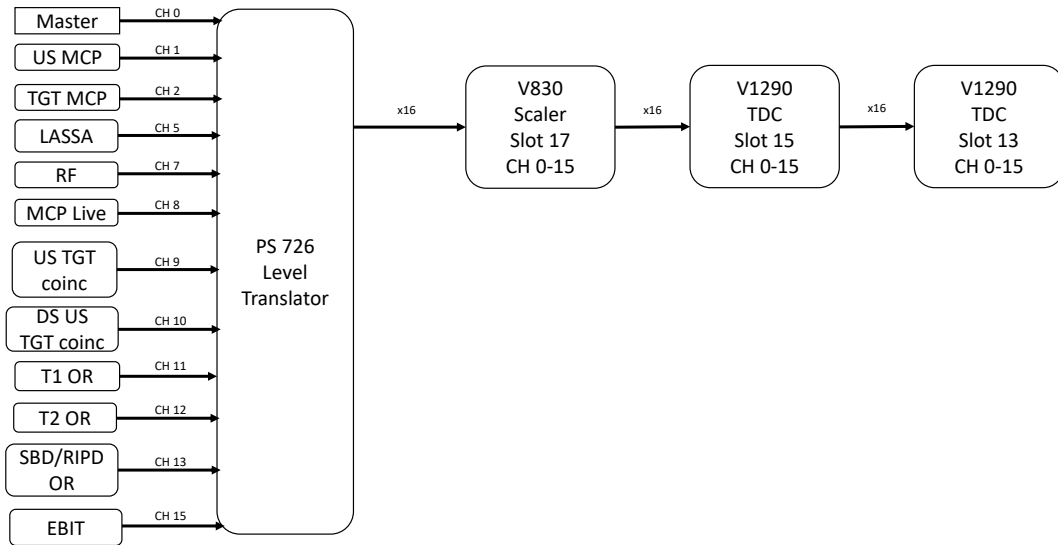
FIGURE A.2: Electronics diagram for the level translator in E17002.
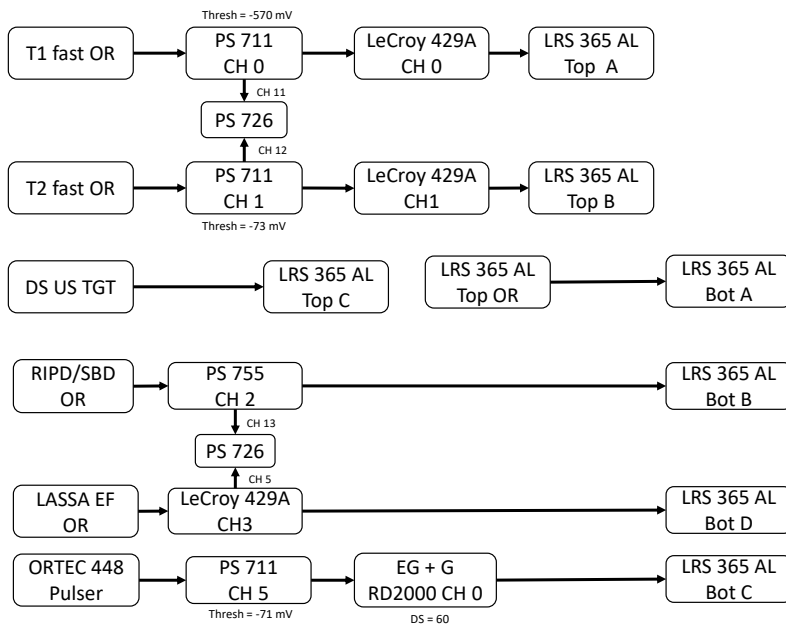
FIGURE A.3: Electronics diagram for the trigger logic in E17002.
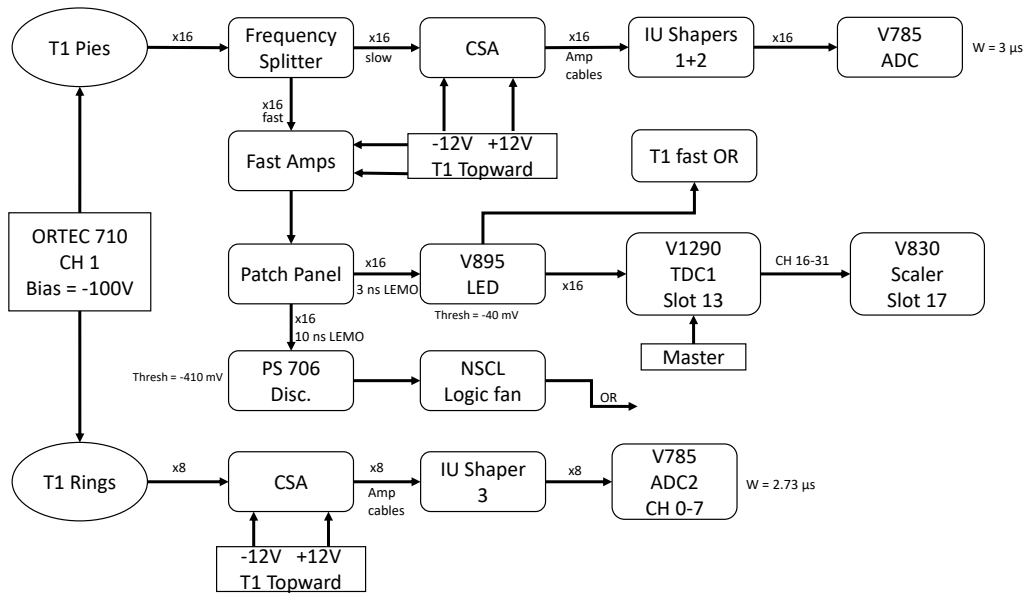
FIGURE A.4: Electronics diagram for the T1 pies and rings in E17002.
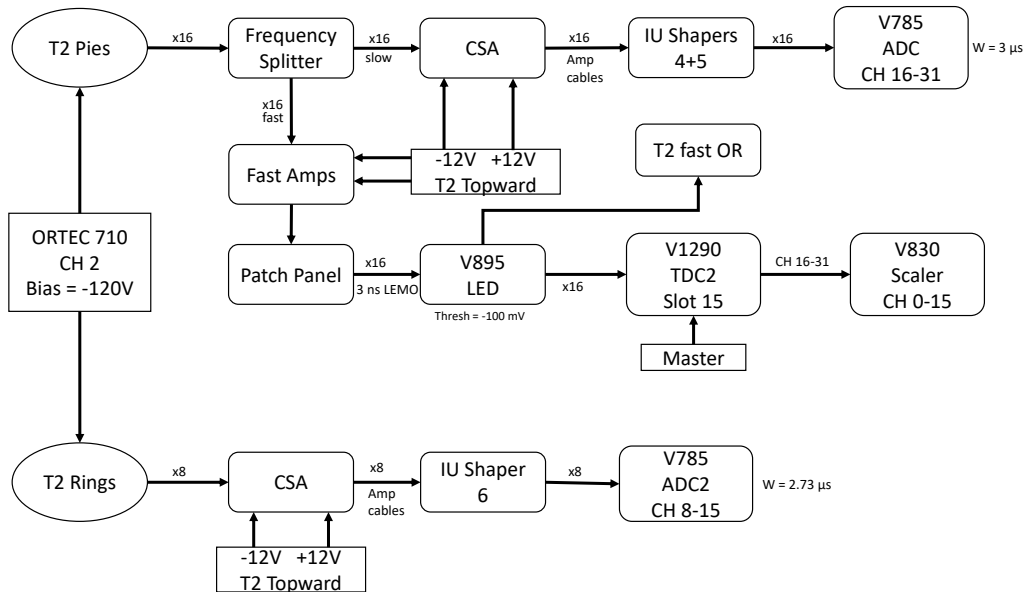
FIGURE A.5: Electronics diagram for the T2 pies and rings in E17002.

123
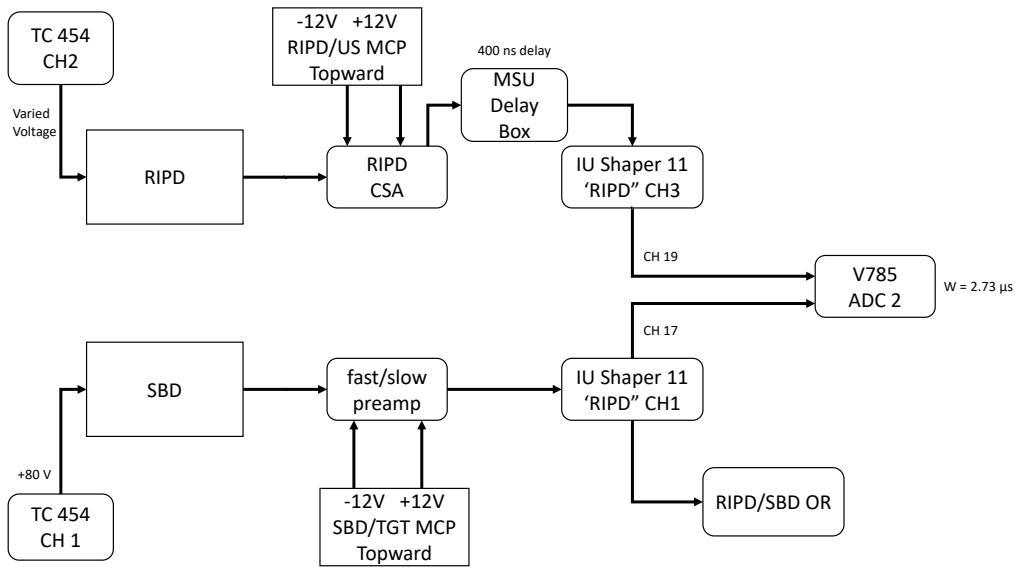
FIGURE A.6: Electronics diagram for the SBD and RIPD in E17002.
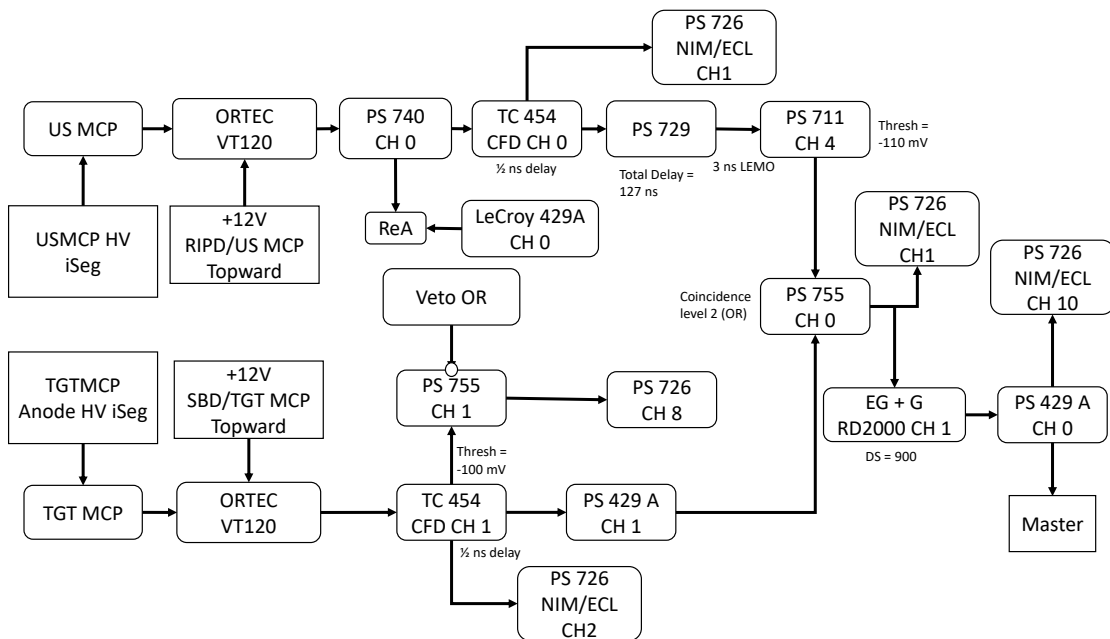
FIGURE A.7: Electronics diagram for the MCPs in E17002.

124
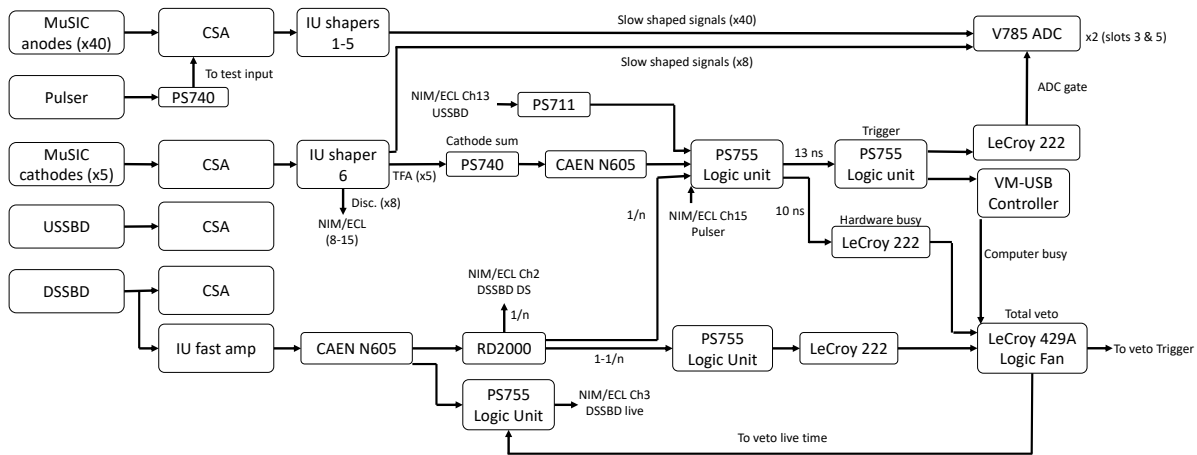
FIGURE A.8:   Electronics diagram for MuSIC.

Appendix B

Cross-section details

B.1 ETOF cross-section data

The experimental fusion cross-section is calculated as:

$$\sigma_{fusion} = \frac{N_{ER}}{(N_{beam} * t * \epsilon_{ER})}$$

In the above equation σ_{fusion} is the cross-section for fusion, N_{ER} is the number of evaporation residues, N_{beam} is the number of beam particles, t is the target thickness, and ϵ_{ER} is the geometric efficiency. The table of measured cross-sections for each reaction provides the energy of each datapoint, the calculated σ_{fusion}, the N_{ER} in each telescope T1 and T2, the N_{beam}, and ϵ_{ER}. The caption also provides the target thickness and a description of which segments of the silicon detectors were used to calculate ϵ_{ER}.

Note that all ^{39}K and ^{47}K data shown in the main body of this thesis are from a prior experiment (E15505). Details of those measurements can be found in Appendix C of Ref. [83]. As a reference between E17002 and E15505, three energies of ^{39}K beam were measured in E17002 but are not shown in the main body of this thesis. Those datapoints are reported here in this appendix.

TABLE B.1: Cross-section information for ^{36}Ar+^{16}O. Data collected in experiment E17002. T1 used rings 1-6 and T2 used rings 0-7 for all energies. An additional efficiency correction $\epsilon_{pie} = 15/16$ was applied to all energies except ID89 to account for a faulty pie segment. For ID89, $\epsilon_{pie} = 14/16$. The target thickness used in this experiment was 98±4 μg/cm^2 of ^{16}O as measured by RBS.

ID	$E_{c.m.}$ (MeV)	σ (mb)	$N_{ER,T1}$	$N_{ER,T2}$	N_{beam}	ϵ_{ER}
103	28.527 ± 0.109	$373.755^{+30.7}_{-30.5}$	59	162	206683937	0.7776
107	29.926 ± 0.111	$468.697^{+34.5}_{-35.0}$	95	211	228362837	0.7773
100	27.735 ± 0.109	$330.314^{+29.7}_{-32.0}$	55	113	177848509	0.7782
92	25.272 ± 0.108	$253.831^{+21.9}_{-22.4}$	50	142	264193547	0.7560
91	24.558 ± 0.104	$235.772^{+23.4}_{-24.2}$	46	87	197641186	0.7765
89	23.984 ± 0.105	$116.530^{+20.4}_{-16.5}$	13	44	175864857	0.7668

TABLE B.2: Cross-section information for ^{44}Ar+^{16}O. Data collected in experiment E17002. The target thickness used in this experiment was 98±4 μg/cm^2 of ^{16}O as measured by RBS.

ID	$E_{c.m.}$ (MeV)	σ (mb)	$N_{ER,T1}$	$N_{ER,T2}$	N_{beam}	ϵ_{ER}
124	28.523 ± 0.117	$404.683^{+44.4}_{-44.4}$	45	56	99881828	0.6792
121	27.867 ± 0.114	$382.799^{+48.3}_{-50.3}$	47	52	103001967	0.6825
116	26.386 ± 0.113	$332.790^{+38.3}_{-39.0}$	62	28	154159737	0.4769
111	25.077 ± 0.116	$352.770^{+34.4}_{-34.5}$	54	82	154938279	0.6764
108	24.179 ± 0.117	$288.235^{+34.2}_{-35.5}$	39	46	118093480	0.6788
106	23.577 ± 0.118	$223.278^{+34.2}_{-37.0}$	21	26	84272530	0.6790

TABLE B.3: Cross-section information for ^{39}K+^{16}O. Data collected in E17002. The target thickness used in this experiment was 98±4 μg/cm^2 of ^{16}O as measured by RBS. The three datapoints recorded here are not shown in the main body of this thesis, but were measured and used as a reference to scale the cross-sections from E15505 (2016) which were calculated without a proper target thickness measurement. That scaled data (which can be found in Appendix C of Ref. [83]) is what is show in this thesis.

ID	$E_{c.m.}$ (MeV)	σ (mb)	$N_{ER,T1}$	$N_{ER,T2}$	N_{beam}	ϵ_{ER}
112	27.604 ± 0.129	$286.712^{+22.2}_{-22.2}$	60	153	299549902	0.7303
9112	31.469 ± 0.074	$496.105^{+58.3}_{-58.3}$	32	62	70571797	0.7298
8112	23.107 ± 0.119	$308.173^{+31.8}_{-33.0}$	25	76	131914893	0.7289

TABLE B.4: Cross-section information for ^{41}K+^{16}O. Data collected in experiment E17002. T1 used rings 1-6 for all energies except ID97 which does not include ring 2. T2 used rings 0-7 for all energies. An additional efficiency correction $\epsilon_{pie} = 15/16$ was applied to all energies to account for a faulty pie segment. The target thickness used in this experiment was 98 ± 4 μg/cm^2 of ^{16}O as measured by RBS.

ID	$E_{c.m.}$ (MeV)	σ (mb)	$N_{ER,T1}$	$N_{ER,T2}$	N_{beam}	ϵ_{ER}
111	29.878 ± 0.072	$646.623^{+57.8}_{-58.7}$	61	111	100880078	0.7168
9111	26.082 ± 0.122	$204.536^{+40.5}_{-43.2}$	4	23	50342597	0.7128
8111	29.244 ± 0.078	$378.160^{+30.4}_{-30.8}$	75	156	231987725	0.7158
7111	27.146 ± 0.113	$334.709^{+27.9}_{-29.4}$	84	155	271766808	0.7142
100	26.125 ± 0.083	$278.968^{+28.5}_{-29.3}$	37	84	165380705	0.7129
9100	24.048 ± 0.115	$161.166^{+39.7}_{-38.7}$	6	12	43124767	0.7040
97	25.407 ± 0.083	$181.157^{+27.9}_{-28.3}$	46	0	278639073	0.6577
95	24.626 ± 0.077	$165.529^{+16.5}_{-16.5}$	51	78	297906126	0.7111
92	23.694 ± 0.076	$104.154^{+11.3}_{-10.9}$	35	78	414421652	0.7117

TABLE B.5: Cross-section information for ^{36}Ar+^{28}Si. Data collected in experiment E17002. T1 used rings 1-6 and T2 used rings 0-7 for all energies. An additional efficiency correction $\epsilon_{pie} = 15/16$ was applied to all energies except ID89 to account for a faulty pie segment. For ID89, $\epsilon_{pie} = 14/16$. The target thickness used in this experiment was 258 ± 10 μg/cm^2 of ^{28}Si as measured by RBS.

ID	$E_{c.m.}$ (MeV)	σ (mb)	$N_{ER,T1}$	$N_{ER,T2}$	N_{beam}	ϵ_{ER}
103	40.562 ± 0.159	$298.2^{+18.8}_{-18.6}$	59	198	206683937	0.8030
107	42.551 ± 0.161	$451.8^{+22.0}_{-22.4}$	100	318	228362837	0.8109
100	39.436 ± 0.160	$266.4^{+18.9}_{-18.9}$	41	145	177848509	0.8115
92	35.934 ± 0.158	$76.4^{+8.4}_{-8.6}$	11	71	264193547	0.8189
91	34.919 ± 0.151	$46.0^{+7.4}_{-7.4}$	6	33	197641186	0.8245
89	34.103 ± 0.155	$13.4^{+4.4}_{-4.2}$	2	6	175864857	0.8184

B.2 MuSIC cross-section data

For the measurements done with MuSIC@Indiana, the experimental fusion cross-section was calculated using the same equation as given above:

$$\sigma_{fusion} = \frac{N_{ER}}{(N_{beam} * t * \epsilon_{ER})}$$

TABLE B.6: Cross-section information for ^{44}Ar+^{28}Si. Data collected in experiment E17002. T1 used rings 2-6 and T2 used 0-7 for all energies. An additional efficiency correction $\epsilon_{pie} = 15/16$ was applied to all energies to account for a faulty pie segment. The target thickness used in this experiment was 258±10 μg/cm^2 of ^{28}Si as measured by RBS.

ID	$E_{c.m.}$ (MeV)	σ (mb)	$N_{ER,T1}$	$N_{ER,T2}$	N_{beam}	ϵ_{ER}
124	41.596 ± 0.180	$339.8\,^{+28.9}_{-28.6}$	39	103	99881828	0.8043
121	40.640 ± 0.177	$265.6\,^{+25.3}_{-25.0}$	27	86	103001967	0.8011
116	38.480 ± 0.172	$234.6\,^{+19.2}_{-19.4}$	55	95	154159737	0.7972
111	36.570 ± 0.177	$131.5\,^{+14.4}_{-14.4}$	27	55	154938279	0.7928
108	35.261 ± 0.176	$76.1\,^{+12.5}_{-13.2}$	12	26	118093480	0.7912
106	34.383 ± 0.176	$75.1\,^{+14.7}_{-14.7}$	8	18	84272530	0.7893

TABLE B.7: Cross-section information for ^{39}K+^{28}Si. Data collected in experiment E17002. T1 used rings 2-6 for ID112 and ID8112 and rings 4-6 for ID9112. T2 used rings 0-7 for all energies. An additional efficiency correction ϵ_{pie} = 15/16 was applied to all energies to account for a faulty pie segment. The target thickness used in this experiment was 258±10 μg/cm^2 of ^{28}Si as measured by RBS. The three datapoints shown here are for the data collected in E17002. The other ^{39}K+^{28}Si data shown in this thesis comes from E15505 and can be found in Appendix C of Ref. [83].

ID	$E_{c.m.}$ (MeV)	σ (mb)	$N_{ER,T1}$	$N_{ER,T2}$	N_{beam}	ϵ_{ER}
112	39.656 ± 0.187	$137.6\,^{+11.0}_{-11.3}$	18	156	299549902	0.7974
9112	45.208 ± 0.113	$386.4\,^{+40.5}_{-37.7}$	0	85	70571797	0.7403
8112	41.814 ± 0.174	$283.3\,^{+24.0}_{-23.1}$	25	119	131914893	0.7923

For the MuSIC@Indiana measurements, the beam count is consistent across all measured datapoints. Additionally, the target thickness of each datapoint is given by the gas pressure length of the detector used. These values are given in the caption of the following tables. The residue detection efficiency is 100% over all measured datapoints. Each table contains the energy of each datapoint, the σ_{fusion}, and the N_{ER}.

TABLE B.8: Cross-section information for ^{41}K+^{28}Si. Data collected in experiment E17002. T1 used rings 2-6 for energies ID111, ID9111, ID7111, and ID9100 and rings 4-6 for ID8111. T1 was not used for ID100, ID97, ID95, and ID92. T2 used rings 0-7 for all energies. The target thickness used in this experiment was 258±10 μg/cm^2 of ^{28}Si as measured by RBS.

ID	$E_{c.m.}$ (MeV)	σ (mb)	$N_{ER,T1}$	$N_{ER,T2}$	N_{beam}	ϵ_{ER}
111	43.194 ± 0.111	$416.7 \, ^{+33.2}_{-33.2}$	0	121	100880078	0.7865
9111	37.705 ± 0.180	$100.3 \, ^{+21.9}_{-21.9}$	5	16	50342597	0.7992
8111	42.277 ± 0.119	$354.6 \, ^{+19.9}_{-19.9}$	0	267	231987725	0.7430
7111	39.243 ± 0.169	$176.5 \, ^{+12.5}_{-12.5}$	42	156	271766808	0.7977
100	37.768 ± 0.124	$111.0 \, ^{+14.4}_{-14.3}$	-	56	165380705	0.6283
9100	34.765 ± 0.170	$33.5 \, ^{+14.8}_{-13.7}$	4	1	43124767	0.7974
97	36.730 ± 0.125	$65.3 \, ^{+9.1}_{-8.6}$	-	55	278639073	0.6229
95	35.601 ± 0.120	$35.2 \, ^{+6.0}_{-6.0}$	-	34	297906126	0.6236
92	34.253 ± 0.116	$6.7 \, ^{+2.2}_{-2.2}$	-	7	414421652	0.6228

TABLE B.9: Cross-section information for ^{45}K+^{28}Si. Data collected in experiment E17002. T1 used rings 2-6 for all energies except ID9117 which used rings 4-6. T2 used rings 0-7 for all energies. The target thickness used in this experiment was 258±10 μg/cm^2 of ^{28}Si as measured by RBS.

ID	$E_{c.m.}$ (MeV)	σ (mb)	$N_{ER,T1}$	$N_{ER,T2}$	N_{beam}	ϵ_{ER}
117	40.662 ± 0.165	$205.4 \, ^{+13.3}_{-13.5}$	85	154	284136913	0.7874
9117	43.261 ± 0.128	$318.6 \, ^{+24.8}_{-25.3}$	33	138	147122024	0.7095
115	39.716 ± 0.161	$198.7 \, ^{+19.9}_{-18.6}$	41	88	157268366	0.7873
9112	35.830 ± 0.168	$38.8 \, ^{+5.3}_{-5.3}$	11	43	343690826	0.7775
8112	36.663 ± 0.195	$90.4 \, ^{+9.9}_{-9.9}$	31	53	229616822	0.7778
8117	37.905 ± 0.178	$140.4 \, ^{+17.7}_{-18.2}$	19	43	110497942	0.7805
6117	38.567 ± 0.176	$131.7 \, ^{+15.0}_{-14.6}$	23	56	151349209	0.7813
123	40.368 ± 0.184	$217.6 \, ^{+21.7}_{-22.0}$	30	69	114614159	0.7862
107	34.834 ± 0.147	$30.5 \, ^{+6.2}_{-6.1}$	10	15	200494638	0.7859
9107	34.122 ± 0.168	$8.3 \, ^{+3.4}_{-3.6}$	0	6	179642746	0.7769

TABLE B.10: Cross-section information for $^{18}O+^{12}C$ as determined by the simple analysis described in Section 6.1.3. The target thickness used in this analysis was 6.1762e18 nuclei/cm^2 of ^{12}C (1 anode thickness of CH$_4$ at 150 Torr). The beam count (N$_{beam}$) for this dataset is 220682000. Anode 0 has no cross-section because it is used as a control anode in the analysis and therefore must only contain beam events. Anodes after anode 15 do not have 100% efficiency and so no cross-section was calculated.

Anode	E$_{c.m.}$ (MeV)	σ (mb)	N$_{ER}$
0	-	-	-
1	19.521 ± 0.258	1127.7 ± 28.8	1537
2	18.990 ± 0.273	1129.2 ± 28.8	1539
3	18.451 ± 0.266	1068.3 ± 28.0	1456
4	17.905 ± 0.280	1056.5 ± 27.8	1440
5	17.340 ± 0.284	1016.2 ± 27.3	1385
6	16.766 ± 0.289	1033.0 ± 27.5	1408
7	16.184 ± 0.293	987.5 ± 26.9	1346
8	15.595 ± 0.295	958.9 ± 26.5	1307
9	14.976 ± 0.324	896.6 ± 25.6	1222
10	14.324 ± 0.327	878.2 ± 25.4	1197
11	13.695 ± 0.302	775.5 ± 23.9	1057
12	13.065 ± 0.327	737.4 ± 23.3	1005
13	12.398 ± 0.340	638.3 ± 40.8	870
14	11.701 ± 0.356	571.5 ± 37.6	779
15	10.979 ± 0.366	511.4 ± 34.7	697
16	-	-	-
17	-	-	-
18	-	-	-
19	-	-	-

TABLE B.11: Cross-section information for $^{18}O+^{12}C$ as determined by the trace-matching analysis described in Section 6.2.3 and binned at a one-anode spacing. The target thickness used in this analysis was 6.1762e18 nuclei/cm^2 of ^{12}C (1 anode thickness of CH$_4$ at 150 Torr). The beam count (N$_{beam}$) for this dataset is 220682000. The bin associated with anode 0 have no cross-section because anode 0 is used as a control anode in the analysis and therefore must only contain beam events. Bins associated with anodes after anode 15 are excluded because these anodes do not have 100% efficiency.

Bin	E$_{c.m.}$ (MeV)	σ (mb)	N$_{ER}$
0	-	-	-
1	19.521 ± 0.258	1082.2 ± 28.2	1475
2	18.990 ± 0.273	1025.0 ± 27.4	1397
3	18.451 ± 0.266	1030.8 ± 27.5	1405
4	17.905 ± 0.280	1003.0 ± 27.1	1367
5	17.340 ± 0.284	1031.6 ± 27.5	1406
6	16.766 ± 0.289	1049.2 ± 27.7	1430
7	16.184 ± 0.293	914.2 ± 25.9	1246
8	15.595 ± 0.295	932.5 ± 26.2	1271
9	14.976 ± 0.324	901.7 ± 25.7	1229
10	14.324 ± 0.327	856.2 ± 25.1	1167
11	13.695 ± 0.302	827.6 ± 24.6	1128
12	13.065 ± 0.327	751.3 ± 23.5	1024
13	12.398 ± 0.340	635.4 ± 21.6	866
14	11.701 ± 0.356	578.9 ± 20.6	789
15	10.979 ± 0.366	409.4 ± 17.3	558

TABLE B.12: Cross-section information for ^{18}O+^{12}C as determined by the trace-matching analysis described in Section 6.2.3 and binned at half-anode spacing. The target thickness used in this analysis was 3.0881e18 nuclei/cm^2 of ^{12}C (half-anode thickness of CH$_4$ at 150 Torr). The beam count (N$_{beam}$) for this dataset is 220682000. The bins associated with anode 0 have no cross-section because anode 0 is used as a control anode in the analysis and therefore must only contain beam events. Bins associated with anodes after anode 15 are excluded because these anodes do not have 100% efficiency.

Bin	E$_{c.m.}$ (MeV)	σ (mb)	N$_{ER}$
0	-	-	-
1	-	-	-
2	19.650 ± 0.129	1082.9 ± 39.9	738
3	19.392 ± 0.129	1081.5 ± 39.8	737
4	19.127 ± 0.137	1050.6 ± 39.3	716
5	18.853 ± 0.137	999.3 ± 38.3	681
6	18.584 ± 0.133	1008.1 ± 38.5	687
7	18.318 ± 0.133	1053.6 ± 39.3	718
8	18.045 ± 0.140	989.0 ± 38.1	674
9	17.765 ± 0.140	1016.9 ± 38.6	693
10	17.482 ± 0.142	1066.8 ± 39.6	727
11	17.198 ± 0.142	996.4 ± 38.2	679
12	16.911 ± 0.145	1068.3 ± 39.6	728
13	16.622 ± 0.145	1030.1 ± 38.9	702
14	16.330 ± 0.147	921.5 ± 36.8	628
15	16.037 ± 0.147	906.8 ± 36.5	618
16	15.743 ± 0.148	943.5 ± 37.2	643
17	15.448 ± 0.148	921.5 ± 36.8	628
18	15.138 ± 0.162	925.9 ± 36.9	631
19	14.814 ± 0.162	877.5 ± 35.9	598
20	14.488 ± 0.164	903.9 ± 36.4	616
21	14.161 ± 0.164	808.5 ± 34.4	551
22	13.846 ± 0.151	830.5 ± 34.9	566
23	13.544 ± 0.151	824.7 ± 34.8	562
24	13.229 ± 0.164	785.0 ± 33.9	535
25	12.902 ± 0.164	717.5 ± 32.5	489
26	12.568 ± 0.170	631.0 ± 30.4	430
27	12.228 ± 0.170	639.8 ± 30.6	436
28	11.879 ± 0.178	569.3 ± 28.9	388
29	11.523 ± 0.178	588.4 ± 29.4	401
30	11.162 ± 0.183	510.6 ± 27.4	348

Appendix C

Program directories

- E17002 analysis:

  `/nfshome/garfield/jej13/MSU19/Winter19/`

  `/Ana/` - all analysis code in this directory

  `/Macros/CalcXSection.C` - Calculates the cross-sections for K,Ar+Si.

  `/Macros/CalcXSection_Reduced.C` - Calculates the reduced cross-sections for K,Ar+Si.

  `/Macros/CheckPID.C` - Plots ΔE-TOF and PID gate.

  `/Macros/DrawExptvsCalc.C` - Plots the experimental K,Ar+Si data against the calculations.

  `/Macros/DrawExptvsTheory_Paper.C` - Plots the experimental K,Ar+Si data again the calculations with the appropriate formatting for the K+Si paper.

  `/Macros/DrawN20andN28_Paper.C` - Plots K,Ar+Si data based upon how close the nuclides are to either the N=20 or N=28 closed neutron-shells with formatting for the K+Si paper.

  `/Macros/DrawReducedExcFunc_Paper.C` - Plots the K,Ar+Si reduced excitation functions with formatting for the K+Si paper.

  `/Macros/DrawSivsOComparison_Paper.C` - Plots the K,Ar+Si reduced excitation functions for comparison to K,Ar+O reduced excitation functions with formatting for K+Si paper.

  `/Macros/GetPIDShift.C` - Gets the shift in order to move the PID spectrum for a particular run to match the gate made for the reference run.

`/Macros/GetPIDShift_AllRuns.C` - Gets the shift described above for all runs.

`/Macros/PlotEvA_AllE.C` - Plots the EvsA spectra for all energies at the same time.

`/Macros/PlotEvA.C` - Plots a specific EvsA spectrum.

`/Macros/PlotPES.C` - Plots the potential energy surface for K+Si.

`/Macros/QuickReadSRIM.C` - Reads the SRIM output files.

`/Macros/ReadSRIM_Transmit.C` - Reads the SRIM transmit files.

`/Macros/ReadSRIM_TransmitHalfTarget.C` - Read the SRIM transmit files used in the half-target calculations.

`/Macros/ReadSRIM_TransmitSBD.C` - Read the SRIM transmit files used in calculating the SBD energy.

`/Calib/T1/GetT1Calib.C` - Calculates the T1 calibration for E17002.

`/Calib/T2/GetT2Calib.C` - Calculates the T2 calibration for E17002.

`/Calib/T2/Mass/GetT2A.C` -

`/Calib/T2/ScatteringLine/` - Macros used in gating the ETOF scattering lines.

- Initial MuSIC@Indiana bench tests:

  `/nfshome/garfield/jej13/MUSIC/InitialTests/`

  `Ana/RawAnalyse_MUSIC.C` - Raw analysis of the bench data.

  `Ana/CalibAnalyse_MUSIC.C` - Calibrated analysis of the bench data.

  `Macros/MUSICCalib.C` - Creates the MuSIC calibration from the raw spectra.

  `Macros/ReadTraces.C` - Reads the data traces and plots them.

  `Macros/PlotMUSICCorrel.C` - Creates and plots the correlations between anodes of MuSIC.

135

`Macros/GetMUSICResolution.C` - Calculates the resolution of the MuSIC anodes.

- MuSIC simple analysis:

  `/nfshome/charlie/jej13/ND2021/`

  `/Ana/CalibAnalyse_MUSIC_countv3.C` - Simple analysis code.

  `/Macros/PlotAnodeCorrel_NIM.C` - Creates the anode-anode correlation plots with the formatting for the MuSIC simple analysis NIM.

  `/Macros/PlotSigma_NIM.C` - Creates the final MuSIC simple analysis cross-section with the formatting for the MuSIC simple analysis NIM.

  `/Macros/PlotTraces_NIM.C` - Plots the experimental traces with the formatting for the MuSIC simple analysis NIM.

  `/Macros/PlotdEdX_All.C` - Plots the experimental energy loss curves with the formatting for the MuSIC simple analysis NIM.

- MuSIC simulation:

  `/nfshome/charlie/jej13/ND2021/Simulation/`

  `IURange.C` - Creates the IURange class.

  `IUMusic.C` - Creates the IUMusic class.

  `IUMusicGeo.C` - Creates the MuSIC geometry class (important for simulating new data if the anode ever changes).

  `IUMusicSimInput.C` - Inputs to the MuSIC class.

  `IUMusicSimUtils.C` - Functions for the MuSIC class.

  `MuSICSim_LeftRight.C` - Code that creates the simulated library.

- MuSIC advanced analysis:

  `/nfshome/charlie/jej13/ND2021/`

`/AnaTest/AdvancedAna_compact.C` - Code which does the advanced analysis.

`/AnaTest/MakeMusicAnaSmart.C` - Creates the command to analyze multiple runs at once.

`/Macros/PlotAdvAna_AdvPaper.C` - Plots the final cross-section with the formatting for the advanced analysis paper.

`/Macros/PlotAdvAna_Sigma.C` - Plots the final cross-section.

`/Macros/PlotAdvTraces_AdvPaper.C` - Plots the traces of the advanced analysis with the formatting of the advanced analysis paper.

`/Macros/PlotChi2VsX_AdvPaper_Clean.C` - Plots Chi2 vs various parameters used in the advanced analysis with the formatting of the advanced analysis paper.

`/Macros/PlotMeasuredRvsE_AdvPaper.C` - Plots the measured ion range vs energy with the formatting of the advanced analysis paper.

`/Macros/PlotSimulatedTraces_AdvPaper.C` - Plots the simulated traces with the formatting of the advanced analysis paper.

`/Macros/PlotZ_AdvPaper.C` - Plots the measured Z-distribution with the formatting of the advanced analysis paper.

- Papers:

  `/nfshome/garfield/jej13/Papers/`

  `SiTgt/SiTgt_NIM.tex` - Silicon target NIM main text.

  `MUSIC/MUSIC_NIM.tex` - MuSIC simple analysis NIM main text.

  `MUSICAdvAna/` - Only contains figures. Main text is on overleaf.

  `XPlusSi/` - Only contains figures. Main text is on overleaf.

- RGA:

`/nfshome/garfield/jej13/Detector/RGA/RGA_Ana_Analog.C` - Reads and plots the RGA analog data.

`/nfshome/garfield/jej13/Detector/RGA/RGA_Ana_PvT.C` - Reads and plots the pressure vs time RGA data.

- RBS:

`/nfshome/garfield/jej13/Detector/RBS/Get_RBSData.C` - Reads and plots the RBS data.

`/nfshome/garfield/jej13/Detector/RBS/Get_RBSData_SH.C` - Reads and plots the RBS data (modified by Sylvie).

- XPS:

`/nfshome/garfield/jej13/Detector/XPS/XPS_Profile.C` - Reads the XPS data and creates the XPS profile.

Bibliography

[1] *2015 NSAC Long Range Plan: The Frontiers of Nuclear Science*, 2015. http://science.energy.gov/np/nsac/. 1

[2] W. D. Loveland, D. J. Morrissey, and G. T. Seaborg. *Modern Nuclear Chemistry.* John Wiley and Sons, Inc., 2006. 1, 4

[3] I. Tanihata, H. Hamagaki, O. Hashimoto, Y. Shida, N. Yoshikawa, K. Sugimoto, O. Yamakawa, T. Kobayashi, and N. Takahashi. Measurements of Interaction Cross Sections and Nuclear Radii in the Light p-Shell Region. *Phys. Rev. Lett.*, 55:2676, 1985. 1

[4] J. Vadas, Varinderjit Singh, B. B. Wiggins, J. Huston, S. Hudan, R. T. deSouza, Z. Lin, C. J. Horowitz, A. Chbihi, D. Ackermann, M. Famiano, and K. W. Brown. Probing the fusion of neutron-rich nuclei with re-accelerated radioactive beams. *Phys. Rev. C*, 97:031601(R), 2018. doi: 10.1103/PhysRevC.97.031601. 1, 22, 40, 41, 63, 64, 114

[5] Varinderjit Singh, J. Vadas, T. K. Steinbach, B. B. Wiggins, S. Hudan, R. T. deSouza, Zidu Lin, C. J. Horowitz, L. T. Baby, S. A. Kuvin, Vandana Tripathi, I. Wiedenhover, and A. S. Umar. Fusion enhancement at near and sub-barrier energies in ^{19}O+^{12}C. *Phys. Lett. B*, 765:99–103, 2017. doi: 10.1016/j.physletb. 2016.12.017. 1, 22, 39, 63

[6] S. Hudan, R. T. deSouza, A. S. Umar, Zidu Lin, and C. J. Horowitz. Enhanced dynamics in fusion of neutron-rich oxygen nuclei at above-barrier energies. *Phys. Rev. C*, 101:061601, 2020. doi: 10.1103/PhysRevC.101.061601. 1, 22, 119

139

[7] R. T. deSouza, V. Singh, S. Hudan, Z. Lin, and C. J. Horowitz. Effect of increasing neutron-excess on the fusion cross-section in $^{12-15}$C + ^{12}C at above-barrier energies. *Phys. Lett. B*, 814:136115, 2021. doi: 10.1016/j.physletb.2021.136115. 1, 22

[8] FRIB, 2022. URL http://frib.msu.edu. Facility for Rare Isotope Beams, Michigan State University, USA. 1

[9] E. M. Burbidge, G. R Burbidge, W. A. Fowler, and F. Hoyle. Synthesis of the Elements in Stars. *Rev. Mod. Phys*, 28:547–650, 1957. 2, 4

[10] P. Moller, J. R. Nix, and K. L. Kratz. Nuclear properties for astrophysical and radioactive-ion-beam applications. *At. Data Nuc. Data Tables*, 66:131–343, 1997. 3

[11] T. Kodama and K. Takahashi. R-process nucleosynthesis and nuclei far form the region of β-stability. *Nucl. Phys. A*, 239:489–510, 1975. 4

[12] C. Sneden and J. J. Cowan. Genesis of the Heaviest Elements in the Milky Way Galaxy. *Science*, 299:70–75, 2003. 5

[13] S. Goriely, P. Demetriou, H. T. Janka, J. M. Pearson, and M. Samyn. The r-process nucleosynthesis: a continued challenge for nuclear physics and astrophysics. *Nucl. Phys. A*, 758:587–594, 2005. 4

[14] Y. Z. Qian. Supernovae versus Neutron Star Mergers as the Major r-Process Sources. *The Astrophysical Journal*, 534:L67, 2000. 4

[15] The LIGO Scientific Collaboration. Advanced LIGO. *Class. Quantum Grav.*, 32: 074001, 2015. 4

[16] F. Acernese et al. Advanced Virgo: a second-generation interferometric gravitational wave detector. *Class. Quantum Grav.*, 32:024001, 2015. 5

[17] B. P. Abbott et al. GW170817: Observation of Gravitaitonal Waves from a Binary Neutron Star Inspiral. *Phys. Rev. Lett.*, 119:161101, 2017. 5

[18] A. Goldstein et al. An Ordinary Short Gamma-Ray Burst with Extraordinary Implications: Fermi-GBM Detection of GRB 170817A. *ApJL*, 848:2, 2017. 5

[19] V. Savchenko et al. INTEGRAL Detection of the First Prompt Gamma-Ray Signal Coincident with the Gravitational-wave Event GW170717. *ApJL*, 848:2, 2017. 5

[20] M. R. Drout et al. Light curves of the neutron star merger GW170817/SSS17a: Implications for r-process nucleosynthesis. *Science*, 358:1570–1574, 2017. 5

[21] W. Baade and F. Zwicky. Remarks on super-novae and cosmic rays. *Phys. Rev.*, 43:76, 1934. 5

[22] M. Seeds and D. Backman. *Astronomy: The Solar System and Beyond*. Cengage Learning, 2009. 6

[23] D. G. Ravenhall, C. J. Pethick, and J. R. Wilson. Structure of Matter below Nuclear Saturation Density. *Phys. Rev. Lett.*, 50:2066, 1983. 6

[24] M. E. Caplan, A. S. Schneider, and C. J. Horowitz. Elasticity of Nuclear Pasta. *Phys. Rev. Lett.*, 121:132701, 2018. 6

[25] H. Schatz and K. E. Rehm. X-ray binaries. *Nucl. Phys. A*, 777:601–622, 2006. 6

[26] A. Cumming and L. Bildsten. Carbon Flashes in the Heavy-Element Ocean on Accreting Neutron Stars. *The Astrophysical Journal*, 559:L127–L130, 2001. 6

[27] C. J. Horowitz, H. Dussan, and D. K. Berry. Fusion of neutron-rich oxygen isotopes in the crust of accreting neutron stars. *Phys. Rev. C*, 77:045807, 2008. doi: 10. 1103/PhysRevC.77.045807. 6

[28] C. E. Rolfs and W. S. Rodney. *Cauldrons in the Cosmos*. University of Chicago Press, 1988. 7

[29] F. Kaeppeler, H. Beer, K. Wisshak, D. D. Clayton, R. L. Macklin, and R. A. Ward. s-process studies in the light of new experimental cross sections. *The Astrophysical Journal*, 257:821–846, 1982. 7

[30] E. Rutherford. The Scattering of α and β Particles by Matter and the Structure of the Atom. *Philosophical Magazine*, 21, 1911. 8

[31] J. Chadwick. Existence of a Neutron. *Proceedings of the Royal Society A*, 136: 692–708, 1932. 8

[32] D. Iwanenko. The Neutron Hypothesis. *Nature*, 129:798, 1932. 8

[33] W. Heisenberg. Uber den Bau der Atomkerne. I. *Z. Physik*, 77:1–11, 1932. 8

[34] W. Heisenberg. Uber den Bau der Atomkerne. II. *Z. Physik*, 78:156–164, 1932. 8

[35] W. Heisenberg. Uber den Bau der Atomkerne. III. *Z. Physik*, 80:587–596, 1933. 8

[36] J. M. Pearson. The Quest for a Microscopic Nuclear Mass Formula. *Atomic Physics at Accelerators: Mass Spectrometry*, pages 59–74, 2001. 10

[37] M. G. Mayer. Nuclear Configurations in the Spin-Orbit Coupling Model. *Phys. Rev.*, 78:16, 1950. 11

[38] Kaitlin Cook. *Zeptosecond dynamics of trasnfer-triggered breakup: mechanisms, timescales, and consequences for fusion*. PhD thesis, Australia National University, 2016. 14

[39] T. D. Thomas. Cross section for compound-nucleus formation in heavy-ion-induced reactions. *Phys. Rev.*, 16:703, 1959. 14

[40] J. Lilley. *Nuclear Physics: Principles and Applications.* John Wiley and Sons, Inc., 2003. 14

[41] J. R. Huizenga and G. Igo. Theoretical reaction cross-sections for alpha particles with an optical model. *Nuclear Physics*, 29:462–473, 1962. 15

[42] D. L. Hill and J. A. Wheeler. Nuclear constitution and the interpretation of fission phenomena. *Physical Review*, 89:1102, 1953. 15

[43] O. Akyuz and A. Winther. Course on nuclear structure and heavy-ion reactions. In R. A. Broglia, C. H.Dasso, and R. Ricci, editors, *Proceedings of the Enrico Fermi School of Physics 1979.* North-Holland, 1979. 15

[44] J. O. Newton, R. D. Butt, M. Dasgupta, D. J. Hinde, I. I. Gontchar, C. R. Morton, and K. Hagino. Systematic failure of the woods-saxon nuclear potential to describe both fusion and elastic scattering: possible need for a new dynamical approach to fusion. *Phys. Rev. C*, 70:024605, 2004. 15

[45] A. M. Stefanini, G. Montagnoli, R. Silvestri, S. Beghini, L. Corradi, S. Courtin, E. Fioretto, B. Guiot, F. Haas, D. Lebhertz, N. Marginean, P. Mason, F. Scarlassara, R. N. Sagaidak, and S. Szilner. Fusion of the positive Q-value system ^{36}S+^{48}Ca well below the Coulomb barrier. *Phys. Rev. C*, 78:044607, 2008. 15

[46] G. Montagnoli et al. Effects of transfer channels on near- and sub-barrier fusion of ^{32}S + ^{48}Ca. *Phys. Rev. C*, 87:014611, 2013. doi: 10.1103/PhysRevC.87.014611. 15

[47] L. C. Vaz, J. M. Alexander, and G. R. Satchler. Fusion barriers, empirical and theoretical: evidence for dynamic deformation in subbarrier fusion. *Physic Reports*, 69:373–399, 1981. 15

[48] L. R. Gasques, L. C. Chamon, D. Pereira, M. A. G. Alvarez, E. S. Rossi, C. P. Silva, and B. V. Carlson. Global and consistent analysis of the heavy-ion elastic scattering

and fusion processes. *Phys. Rev. C*, 69:034603, 2004. doi: 10.1103/PhysRevC.69.034603. 15, 40

[49] L. C. Chamon, D. Pereira, M. S. Hussein, M. A. Cândido Ribeiro, and D. Galetti. Nonlocal description of the nucleus-nucleus interaction. *Phys. Rev. Lett. C.*, 79:5218–5221, Dec 1997. doi: 10.1103/PhysRevLett.79.5218. URL https://link.aps.org/doi/10.1103/PhysRevLett.79.5218. 16

[50] L. C. Chamon, B. V. Carlson, L. R. Gasques, D. Pereira, C. De Conti, M. A. G. Alvarez, M. S. Hussein, M. A. Candido Ribeiro, E. S. Rossi Jr., and C. P. Silva. Toward a global description of the nucleus-nucleus interaction. *Phys. Rev. C*, 66:014610, Jul 2002. doi: 10.1103/PhysRevC.66.014610. URL https://link.aps.org/doi/10.1103/PhysRevC.66.014610. 16, 47

[51] Varinderjit Singh, J. E. Johnstone, R. Giri, S. Hudan, J. Vadas, R. T. deSouza, D. Ackermann, A. Chbihi, Q. Hourdille, A. Abbott, C. Balhoff, A. Hannaman, A. B. McIntosh, M. Sorenson, Z. Tobin, A. Wakhle, S. J. Yennello, M. A. Famiano, K. W. Brown, C. Santamaria, J. Lubian, H. O. Soler, and B. V. Carlson. Impact of shell structure on the fusion of neutron-rich mid-mass nuclei. *Phys. Rev. C*, 104:L041601, 2021. 16, 60

[52] P. Ring. Relativistic mean field theory in finite nuclei. *Prog. Part. Nucl. Phys.*, 37:193–263, 1996. doi: 10.1016/0146-6410(96)00054-3. 16

[53] B. V. Carlson and D. Hirata. Dirac-Hartree-Bogoliubov approximation for finite nuclei. *Phys. Rev. C*, 62:054310, Oct 2000. doi: 10.1103/PhysRevC.62.054310. URL https://link.aps.org/doi/10.1103/PhysRevC.62.054310. 17, 18, 47, 60

[54] D. Bailin and A. Love. Superfluidity and superconductivity in relativistic fermion systems. *Phys. Rep.*, 105:325–385, 1984. 17

[55] H. Kucharek and P. Ring. Relativistic field theory of superfluidity in nuclei. *Z. Phys. A*, 339:23–35, 1991. 17

[56] F. B. Guimaraes, B. V. Carlson, and T. Frederico. Hartree-fock-bogoliubov approximation to relativistic nuclear matter. *Phys. Rev. C*, 54:2385, 1996. 17

[57] B. V. Carlson, T. Frederico, and F. B. Guimaraes. $^1S_0$ pairing correlations in relativistic nuclear matter and the two-nucleon virtual state. *Phys. Rev. C*, 56: 3097, 1997. 17

[58] C. H. Dasso, S. Landowne, and A. Winther. Channel-coupling effects in heavy-ion fusion reactions. *Nucl. Phys. A*, 405:381–396, 1983. doi: 10.1016/0375-9474(83) 90578-x. 19, 40

[59] C. H. Dasso and S. Landowne. CCFUS - A simplified coupled-channel code for calculation of fusion cross sections in heavy-ion reactions. *Comput. Phys. Commun.*, 47:187–191, 1987. 19

[60] J. Fernandez-Niello, C. H. Dasso, and S. Landowne. CCDEF - A simplified coupled-channel code for fusion cross sections including static nuclear deformations. *Comput. Phys. Commun.*, 54:409–412, 1989. 19

[61] K. Hagino, N. Rowley, and A. T. Kruppa. A program for coupled-channel calculations with all order couplings for heavy-ion fusion reactions. *Comput. Phys. Commun.*, 123:143–152, 1999. doi: 10.1016/s0010-4655(99)00243-x. 19

[62] J. R. Leigh, M. Dasgupta, D. J. Hinde, J. C. Mein, C. R. Morton, R. C. Lemmon, J. P. Lestone, J. O. Newton, H. Timmers, J. X. Wei, and N. Rowley. Barrier distributions from the fusion of oxygen ions with ^{144,148,154}Sm and ^{186}W. *Phys. Rev. C*, 52:3151, 1995. 20

145

[63] M. Beckerman, J. Ball, H. Enge, M. Salomaa, A. Sperduto, S. Gazes, A. DiRienzo, and J. D. Molitoris. Near- and sub-barrier fusion of ^{58}Ni with ^{58}Ni. *Phys. Rev. C*, 23:1581, 1981. 20

[64] K. Hagino, K. Ogata, and A. M. Moro. Coupled-channel calculations for nuclear reactions: From exotic nuclei to superheavy elements. *Prog. Part. Nucl. Phys.*, 125: 103951, 2022. 20

[65] J. W. Negele. The mean-field theory of nuclear structure and dynamics. *Rev. Mod. Phys.*, 54:913, 1982. 20

[66] A. S. Umar and V. E. Oberacker. Three-dimensional unrestricted time-dependent Hartree-Fock fusion calculations using the full Skyrme interaction. *Phys. Rev. C*, 73:054607, 2006. doi: 10.1103/PhysRevC.73.054607. 20

[67] V. E. Oberacker and A. S. Umar. Microscopic analysis of sub-barrier fusion enhancement in ^{132}Sn + ^{40}Ca versus ^{132}Sn + ^{48}Ca. *Phys. Rev. C*, 87:034611, 2013. 20, 21, 22

[68] R. T. deSouza, S. Hudan, V. E. Oberacker, and A. S. Umar. Confronting measured near- and sub-barrier fusion cross sections for ^{20}O+^{12}C with a microscopic method. *Phys. Rev. C*, 88:014602, 2013. doi: 10.1103/PhysRevC.88.014602. 20, 21

[69] A. S. Umar and V. E. Oberacker. Heavy-ion interaction potential deduced from density-constrained time-dependent Hartree-Fock calculation. *Phys. Rev. C*, 74: 021601(R), 2006. doi: 10.1103/PhysRevC.74.021601. 21

[70] A. S. Umar, V. E. Oberacker, and C. J. Horowitz. Microscopic sub-barrier fusion calculations for the neutron star crust. *Phys. Rev. C*, 85:055801, 2012. doi: 10. 1103/PhysRevC.85.055801. 21, 22, 39

[71] J. Thomas, Y. T. Chen, S. Hinds, D. Meredith, and M. Olson. Sub-barrier fusion of the oxygen isotopes: A more complete picture. *Phys. Rev. C*, 31:1980, 1986. 22, 31

[72] C. Simenel, A. S. Umar, K. Godbey, M. Dasgupta, and D. J. Hinde. How the pauli exclusion principle affects fusion of atomic nuclei. *Phys. Rev. C*, 95:031601, 2017. doi: 10.1103/PhysRevC.95.031601. 22

[73] A. S. Umar, C. Simenel, and K. Godbey. Pauli energy contribution to the nucleus-nucleus interaction. *Phys. Rev. C*, 104:034619, 2021. 22

[74] G. Bollen. FRIB - Facility for Rare Isotope Beams. *AIP Conf Proc*, 1124:432, 2010. 22

[75] P. Dolegieviez et al. Status of the SPIRAL2 project. Technical report, GANIL, 2019. 22

[76] A. Gade, B. M. Sherrill, et al. The Scientific Case for the 400 MeV/u Energy Upgrade of FRIB. Technical report, FRIB, 2019. 22

[77] P. F. F. Carnelli, S. Almaraz-Calderon, K. E. Rehm, M. Albers, M. Alcorta, P. F. Bertone, B. Digiovine, H. Esbensen, J. O. Fernandez Niello, D. Henderson, C. L. Jiang, J. Lai, S. T. Marley, O. Nusair, T. Palchan-Hazan, R. C. Pardo, M. Paul, and C. Ugalde. Measurement of Fusion Reactions of Low-Intensity Radioactive Carbon Beams on ^{12}C and their Implications for the Understanding of X-Ray Bursts. *Phys. Rev. Lett.*, 112:192701, 2014. doi: 10.1103/PhysRevLett.112.192701. 22, 33, 80, 82

[78] R. Planeta. Physics of heavy ion collisions. *Int. J. Mod. Phys. E*, 15:973–1068, 2012. 24

[79] T. K. Steinbach, J. Vadas, J. Schmidt, C. Haycraft, S. Hudan, R. T. deSouza, L. T. Baby, S. A. Kuvin, and I. Wiedenhover. Sub-barrier enhancement of fusion as

compared to a microscopic method in ^{18}O+^{12}C. *Phys. Rev. C*, 90:041603(R), 2014. 26, 27, 63, 85, 94, 95, 113

[80] J. D. Bowman and R. H. Heffner. A novel zero time detector for heavy ion spectroscopy. *Nucl. Instr. and Meth. Phys. Res.*, 148:503, 1978. 28

[81] T. K. Steinbach, M. J. Rudolph, Z. Q. Gosser, K. Brown, B. Floyd, S. Hudan, R. T. deSouza, J. F. Liang, D. Shapira, and M. Famiano. Measuring the fusion cross-section of light nuclei with low-intensity beams. *Nucl. Instr. Meth. A*, 743: 5–13, 2014. 28, 35

[82] J. Vadas, V. Singh, G. Visser, A. Alexander, S. Hudan, J. Huston, B. B. Wiggins, A. Chbihi, M. Famiano, M. M. Bischak, and R. T. deSouza. High-rate axial-field ionization chamber for particle identification of radioactive beams. *Nucl. Instr. Meth. A*, 837:28, 2016. 28

[83] Jessica Vadas. *Probing the Fusion of Neutron-Rich Nuclei with Modern Radioactive Beam Facilities*. PhD thesis, Indiana University, 2018. 29, 126, 127, 129

[84] N. G. Nicolis and J. R. Beene. evapOR. *unpublished*, 1993. 29, 103

[85] M. Cwoik, W. Dominik, Z. Janas, A. Korgul, K. Miernik, M. Pfutzner, M. Sawicka, and A. Wasilewski. Optical time projection chamber for imaging of two-proton decay of ^{45}Fe nucleus. *IEEE Trans Nucl Sci*, 52:2895, 2005. 32

[86] J. J. Kolata, A. M. Howard, W. Mittig, T. Ahn, D. Bazin, F. D. Becchetti, S. Beceiro-Novo, Z. Chajecki, M. Febbrarro, A. Fritsch, W. G. Lynch, A. Roberts, A. Shore, and R. O. Torres-Isea. Fusion studies with low-intensity radioactive ion beams using an active-target time projection chamber. *Nucl. Instr. Meth. A*, 830: 82, 2016. 32

[87] Y. Ayyad, N. Abgrall, T. Ahn, H. Alvarez-Pol, D. Bazin, S. Beceiro-Novo, L. Carpenter, R. J. Cooper, M. Cortesi, A. O. Macchiavelli, W. Mittig, B. Olaizola, J. S. Randhawa, C. Santamaria, N. Watwood, J. C. Zamora, and R. G. T. Zegers. Next-generation experiments with the Active Target Time Projection Chamber (AT-TPC). *Nucl. Instr. Meth. A*, 954:161341, 2020. 32

[88] M. Gai, D. Schweitzer, S. R. Stern, A. H. Young, R. Smith, M. Cwiok, J. S. Bihalowicz, H. Czyrkowski, R. Dabrowski, W. Dominik, A. Fijalkowska, Z. Janas, L. Janiak, A. Korgul, T. Matulewicz, C. Mazzocchi, M. Pfutzner, M. Zaremba, D. Balabanski, I. Gheorghe, C. Matei, O. Tesileanu, N. V. Zamfir, M. W. Ahmed, S. S. Henshaw, C. R. Howell, J. M. Mueller, L. S. Myers, S. Stave, C. Sun, H. R. Weller, Y. K. Wu, A. Breskin, V. Dangendorf, K. Tittelmeier, and M. Freer. Time Projection Chamber (TPC) detectors for nuclear astrophysics studies with gamma beams. *Nucl. Instr. Meth. A*, 954:161779, 2020. 32

[89] E. Koshchiy, G. V. Rogachev, E. Pollacco, S. Ahn, E. Uberseder, J. Hooker, J. Bishop, E. Aboud, M. Barbui, V. Z. Goldberg, C. Hunt, H. Jayatissa, C. Magana, R. O'Dwyer, B. T. Roeder, A. Saastamoinen, and S. Upadhyayula. Texas Active Target (TexAT) detector for experiments with rare isotope beams. *Nucl. Instr. Meth. A*, 957:163398, 2020. 32

[90] D. Bazin, T. Ahn, Y. Ayyad, S. Beceiro-Novo, A. O. Macchiavelli, W. Mittig, and J. S. Randhawa. Low energy nuclear physics with active targets and time projection chambers. *Prog. Part. Nucl. Phys.*, 114:103790, 2020. 32

[91] W. B. Christie, J. L. Romero, F. P. Brady, C. E. Tull, C. M. Castaneda, E. F. Barasch, M. L. Webb, J. R. Drummond, H. J. Crawford, I. Flores, D. E. Greiner, P. J. Lindstrom, H. Sann, and J. C. Young. A multiple sampling ionzation chamber (MUSIC) for measuring the charge of relativistic heavy ions. *Nucl. Instr. Meth. A*, 255:466–476, 1987. 32, 33

[92] K. Kimura, Y. Akiba, Y. Miake, and S. Nagamiya. A multiple sampling proportional counter for particle identification of relativistic heavy ions. *Nucl. Instr. Meth. A*, 297:190–198, 1990. 33

[93] R. N. Boyd, I. Tanihata, N. Inabe, T. Kubo, T. Nakagawa, T. Suzuki, M. Yonokura, X. X. Bai, K. Kimura, S. Kubono, S. Shimoura, H. S. Xu, and D. Hirata. Measurement of the $^8\text{Li}(\alpha,\text{n})^{11}\text{B}$ reaction cross section at energies of astrophysical interest. *Phys. Rev. Lett.*, 68:1283–1286, 1992. 33

[94] P. F. F. Carnelli, S. Almaraz-Calderon, K. E. Rehm, M. Albers, M. Alcorta, P. F. Bertone, B. Digiovine, H. Esbensen, J. Fernandez Niello, D. Henderson, C. L. Jiang, J. Lai, S. T. Marley, O. Nusair, T. Palchan-Hazan, R. C. Pardo, M. Paul, and C. Ugalde. Multi-Sampling Ionization Chamber (MUSIC) for measurements of fusion reactions with radioactive beams. *Nucl. Instr. Meth. A*, 799:197, 2015. doi: 10.1016/j.nima.2015.07.030. 33, 34, 81, 87, 91, 96, 98, 100

[95] B. W. Asher, S. Almaraz-Calderon, V. Tripathi, K. W. Kemper, L. T. Baby, N. Gerkena, E. Lopez-Saavedra, A. B. Morelock, J. F. Perello, and I. Wiedenhover. Experimental study of the $^{17}\text{F}+^{12}\text{C}$ fusion reaciton and its implications for fusion of proton-halo systems. *Phys. Rev. C*, 103:044615, 2021. 33, 80

[96] B. W. Asher, S. Almaraz-Calderon, K. W. Kemper, L. T. Baby, E. Lopez-Saavedra, A. B. Morelock, J. F. Perello, V. Tripathi, and N. Keeley. Resolution of a longstanding discrepancy in the $^{17}\text{O}+^{12}\text{C}$ fusion excitation function. *Eur. Phys. J. A.*, 57:272, 2021. 33

[97] D. G. Kovar, D. F. Geesaman, T. H. Braid, Y. Eisen, W. Henning, T. R. Ophel, M. Paul, K. E. Rehm, S. J. Sanders, P. Sperr, J. P. Schiffer, S. L. Tabor, S. Vigdor, B. Zeidman, and F. W. Prosser Jr. Systematics of carbon- and oxygen-induced

fusion on nuclei with $12 \leq A \leq 19$. *Phys. Rev. C*, 20:1305–1331, 1979. doi: 10.1103/ PhysRevC.20.1305. 34, 35, 85, 94, 95, 110

[98] M. L. Avila, K. E. Rehm, S. Almzaraz-Calderon, A. D. Ayangeakaa, C. Dickerson, C. R. Hoffman, C. L. Jiang, B. P. Kay, J. Lai, O. Nusair, R. C. Pardo, D. Santiago-Gonazalez, R. Talwar, and C. Ugalde. Experimental study of the astrophysically important ^{23}na$(\alpha,$p$)^{26}$mg and ^{23}na$(\alpha,$n$)^{26}$al reactions. *Phys. Rev. C*, 94:065804, 2016. 33

[99] M. L. Avila, K. E. Rehm, S. Almzaraz-Calderon, A. D. Ayangeakaa, C. Dickerson, C. R. Hoffman, C. L. Jiang, B. P. Kay, J. Lai, O. Nusair, R. C. Pardo, D. Santiago-Gonazalez, R. Talwar, and C. Ugalde. Study of $(\alpha,$p$)$ and $(\alpha,$n$)$ reactions with a Multi-Sampling Ionization Chamber. *Nucl. Instr. Meth. A*, 859:63–68, 2017. 33, 35, 80, 87, 96, 98, 100

[100] J. K. Bair and F. X. Haas. Total neutron yield from the reactions ^{13}C$(\alpha,$n$)^{16}$O and ^{17,18}O$(\alpha,$n$)^{20,21}$Ne. *Phys. Rev. C*, 7:1356–1364, 1973. 35

[101] Y. Eyal, M. Beckerman, R. Chechik, Z. Fraenkel, and H. Stocker. Nuclear size and boundary effects on fusion barrier of oxygen with carbon. *Phys. Rev. C*, 13: 1527–1535, 1976. doi: 10.1103/PhysRevC.13.1527. 35, 85, 94, 95, 113

[102] D. J. Morrissey and NSCL Staff. A new high-resolution separator for high-intensity secondary beams. *Nucl. Instr. Meth. B*, 126:316, 1997. 36

[103] *The MSU/NSCL Re-acclerator ReA3*, 2015. SRF 2009, Berlin, Germany. 37

[104] G. Montagnoli and A. M. Stefanini. Recent experimental results in sub- and near-barrier heavy-ion fusion reactions. *Rev. Mod. Phys.*, 53:169, 2017. 39

[105] J. J. Kolata, V. Guimaraes, and E. F. Aguilera. Elastic scattering, fusion, and breakup of light exotic nuclei. *The European Physical Journal A*, 52(5):1–38, 2016. doi: https://doi.org/10.1140/epja/i2016-16123-1. 39

[106] M. Alcorta, K. E. Rehm, B. B. Back, S. Bedoor, P. F. Bertone, C. M. Deibel, B. DiGiovine, H. Esbensen, J. P. Greene, C. R. Hoffman, C. L. Jiang, J. C. Lighthall, S. T. Marley, R. C. Pardo, M. Paul, A. M. Rogers, C. Ugalde, and A. H. Wuosmaa. Fusion reactions with the One-Neutron Halo Nucleus ^{15}C. *Phys. Rev. Lett*, 106: 172701, 2011. 39

[107] M. Beckerman, M. Salomaa, A. Sperduto, H. Enge, J. Ball, A. DiRienzo, S. Gazes, Yan Chen, J. D. Molitoris, and Mao Nai-feng. Dynamic influence of valence neutrons upon the complete fusion of massive nuclei. *Phys. Rev. Lett.*, 45:1472–1475, Nov 1980. doi: 10.1103/PhysRevLett.45.1472. URL https://link.aps.org/doi/10.1103/PhysRevLett.45.1472. 39

[108] H. A. Aljuwair, R. J. Ledoux, M. Beckerman, S. B. Gazes, J. Wiggins, E. R. Cosman, R. R. Betts, S. Saini, and O. Hansen. Isotopic effects in the fusion of ^{40}Ca with ^{40,44,48}Ca. *Phys. Rev. C*, 30:1223, 1984. 39

[109] G. Montagnoli, A. M. Stefanini, C. L. Jiang, H. Esbensen, L. Corradi, S. Courtin, E. Fioretto, A. Goasduff, F. Haas, A. F. Kifle, C. Michelagnoli, D. Montanari, T. Mijatoviand K. E. Rehm, R. Silvestri, Pushpendra P. Singh, F. Scarlassara, S. Szilner, X. D. Tang, and C. A. Ur. Fusion of ^{40}Ca+^{40}Ca and other Ca+Ca systems near and below the barrier. *Phys. Rev. C*, 85:024607, 2012. doi: 10.1103/PhysRevC.85.024607. 39

[110] C. Y. Wong. Interaction barrier in charged-particle nuclear reactions. *Phys. Rev. Lett.*, 31:766–769, 1973. doi: 10.1103/PhysRevLett.31.766. 40, 95

[111] L .F. Canto, D. R. Mendes Junior, P. R. S. Gomes, and J. Lubian. Reduction of fusion and reaction cross sections at near-barrier energies. *Phys. Rev. C*, 92:014626, 2015. 45

[112] A. Koszorus, X. F. Yang, W. G. Jiang, S. J. Novario, S. W. Bai, J. Billowes, C. L. Binnersley, M. L. Bissell, T. E. Cocolios, B. S. Cooper, R. P. de Groote, A. Ekstrom, K. T. Flanagan, C. Forssen, S. Franchoo, R. F. Garcia Ruiz, F. P. Gustafsson, G. Hagen, G. R. Jansen, A. Kanellakopoulos, M. Kortelainen, W. Nazarewicz, G. Neyens, T. Papenbrock, P. G. Reinhard, C. M. Ricketts, B. K. Sahoo, A. R. Vernon, and S. G. Wilkins. Charge radii of exotic potassium isotopes challenge nuclear theory and the magic character of n=32. *Nature Physics*, 17:439–443, 2021. doi: 10.1038/s41567-020-01136-5. 45

[113] A. D. Frawley, N. R. Fletcher, and L. C. Dennis. Resonances in the ^{16}O + ^{12}C fusion cross section between E$_{c.m.}$=12 and 20 MeV. *Phys. Rev. C*, 25:860–865, 1982. doi: 10.1103/PhysRevC.25.860. 45

[114] G. S. Li, J. G. Wang, J. Lubian, H. O. Soler, Y. D. Fang, M. L. Liu, N. T. Zhang, X. H. Zhou, Y. H. Zhang, B. S. Gao, Y. G. Qiang, S. Guo, S. C. Wang, K. L. Wang, K. K. Zheng, R. Li, and Y. Zheng. Fusion reactions in the ^{9}Be + ^{197}Au system above the Coulomb barrier. *Phys. Rev. C*, 100:054601, Nov 2019. doi: 10.1103/PhysRevC. 100.054601. URL https://link.aps.org/doi/10.1103/PhysRevC.100.054601. 47

[115] M. Fisichella, A. C. Shotter, P. Figuera, J. Lubian, A. Di Pietro, J. P. Fernandez-Garcia, J. L. Ferreira, M. Lattuada, P. Lotti, A. Musumarra, M. G. Pellegriti, C. Ruiz, V. Scuderi, E. Strano, D. Torresi, and M. Zadro. Breakup and *n*-transfer effects on the fusion reactions ^{6,7}Li+^{120,119}Sn around the coulomb barrier. *Phys. Rev. C*, 95:034617, Mar 2017. doi: 10.1103/PhysRevC.95.034617. URL https://link.aps.org/doi/10.1103/PhysRevC.95.034617. 47

[116] L. F. Canto, P. R. S. Gomes, R. Donangelo, J. Lubian, and M. S. Hussein. Recent developments in fusion and direct reactions with weakly bound nuclei. *Physics Reports*, 596:1–86, 2015. ISSN 0370-1573. doi: https://doi.org/10.1016/j.physrep.2015.08.001. URL https://www.sciencedirect.com/science/article/pii/S0370157315003385. 47

[117] L. F. Canto, P. R. S. Gomes, R. Donangelo, and M. S. Hussein. Fusion and breakup of weakly bound nuclei. *Physics Reports*, 424(1):1–111, 2006. ISSN 0370-1573. doi: https://doi.org/10.1016/j.physrep.2005.10.006. URL https://www.sciencedirect.com/science/article/pii/S037015730500459X. 47

[118] L. C. Chamon, B. V. Carlson, and L. R. Gasques. Sao Paulo potential version 2 (SPP2) and Brazilian nuclear potential (BNP). *Computer Physics Communications*, 267:108061, 2021. ISSN 0010-4655. doi: https://doi.org/10.1016/j.cpc.2021.108061. URL https://www.sciencedirect.com/science/article/pii/S0010465521001739. 47

[119] C. J. Horowitz. Private Communication, 2010. 48

[120] M. Beckerman, M. Salomaa, A. Sperduto, H. Enge, J. Ball, A. DiRienzo, S. Gazes, Yan Chen, J. D. Molitoris, and Mao Nai-feng. Dynamic influence of valence neutrons upon the complete fusion of massive nuclei. *Phys. Rev. Lett.*, 45:1472–1475, Nov 1980. doi: 10.1103/PhysRevLett.45.1472. URL https://link.aps.org/doi/10.1103/PhysRevLett.45.1472. 62

[121] R. G. Stokstad and E. E. Gross. Analysis of the sub-barrier fusion of $^{16}O+^{148,150,152,154}Sm$. *Phys. Rev. C*, 23:281–294, Jan 1981. doi: 10.1103/PhysRevC.23.281. URL https://link.aps.org/doi/10.1103/PhysRevC.23.281. 62

[122] D. Abriola, D. DiGregorio, J. E. Testoni, A. Etchegoyen, M. C. Etchegoyen, J. O. Fernandez Niello, A. M. J. Ferrero, S. Gil, A. O. Macchiavelli, A. J. Pacheco, and

J. Kittl. Energy dependence of the optical potential for the ^{16}O+^{144}Sm system near the Coulomb barrier. *Phys. Rev. C*, 39:546–552, Feb 1989. doi: 10.1103/PhysRevC. 39.546. URL https://link.aps.org/doi/10.1103/PhysRevC.39.546. 62

[123] S. Raman, C. W. Nestor, and P. Tikkanen. Transition probability from the ground to the first-excited 2+ state of even–even nuclides. *Atomic Data and Nuclear Data Tables*, 78(1):1–128, 2001. ISSN 0092-640X. doi: https://doi.org/10.1006/adnd.2001.0858. URL https://www.sciencedirect.com/science/article/pii/S0092640X01908587. 62

[124] A. M. Sandorfi, L. R. Kilius, and J. L. Gallant. The preparation of silicon films suitable for studies of electron-induced fission. *Nuclear Instruments and Methods*, 136:395–396, 1976. 63, 64, 68

[125] A. J. Michielsen and P. Decowski. Silicon targets. *Nucl. Instr. Meth. A*, A282: 121–123, 1989. 63, 69

[126] Able Electropolishing, 2019. URL www.ableelectropolishing.com. 65

[127] Goodfellow, 2019. URL www.goodfellowusa.com. 68

[128] J. R. Rumble Jr., editor. *CRC Handbook of Chemistry and Physics, 100th Edition*. CRC Press/Taylor and Francis, Boca Raton, FL, 2019. 68

[129] Bing-Feng Ju, Yuan-Liu Chen, Mingming Fu, Ye Chen, and Yunhai Yang. Systematic study of electropolishing technique for improving the quality and production reproducibility of tungsten STM probe. *Sensor Actuat A-Phys*, 155:136–144, 2009. 69

[130] A. M. Awad, N. A. Abdel Ghany, and T. M. Dahy. Removal of tarnishing and roughness of copper surface by electropolishing treatment. *Appl. Surf. Sci.*, 256: 4370–4375, 2010. 69

[131] Kurt J. Lesker, 2019. URL https://www.lesker.com. 70

[132] J. F. Ziegler, M. D. Ziegler, and J. P. Biersack. SRIM - The stopping and range of ions in mattter (2010). *Nucl. Instr. Meth. B*, 268:1818–1823, 2010. 74, 87, 98

[133] M. Mayer. *SIMNRA User's Guide.* Report IPP 9/113, Max-Planck-Institut fur Plasmaphysik, Garching, Germany, 1997. 76

[134] L. Foreman, P. Kleban, L. D. Schmidt, and H. T. Davis. Drift velocities and electrons in methane-inert-gas mixtures. *Phys. Rev. A*, 23:1553–1557, 1981. 80

[135] J. Va'vra, P. Coyle, J. Kadyk, and J. Wise. Measurement of electron drift parameters for helium and CF_4-based gases. *Nucl. Instr. Meth. A*, 324:113, 1993. 80

[136] R. T. deSouza. Zeptosystems Inc., 2021. 83, 85

[137] B. Heusch, C. Beck, J. P. Coffin, P. Engelstein, R. M. Freeman, G. Guillaume, F. Haas, and P. Wagner. Entrance channel effect for complete fusion of O + C isotopes. *Phys. Rev. C*, 26:542–554, 1982. doi: 10.1103/PhysRevC.26.542. 85, 94, 95, 109, 113

[138] D. Bazin, O. Tarasov, M. Lewitowicz, and O. Sorlin. The program LISE: a simulation of fragment separators. *Nucl. Instr. Meth. A*, 482:207–327, 2002. 87

[139] J. Vadas, T. K. Steinbach, J. Schmidt, V. Singh, C. Haycraft, S. Hudan, R. T. deSouza, L. T. Baby, S. A. Kuvin, and I. Wiedenhover. Evidence for survival of the α cluster structure in light nuclei through the fusion process. *Phys. Rev. C*, 92: 064610, 2015. 108, 109

[140] P. Sperr, S. Vigdor, Y. Eisen, W. Henning, D. G. Kovar, T. R. Ophel, and B. Zeidman. Oscillations in the Excitation Function for Complete Fusion of $^{16}O+^{12}C$. *Phys. Rev. Lett.*, 37:321, 1976. 110

[141] I. Tserruya, Y. Eisen, D. Pelte, A. Gavron, H. Oeschler, D. Berndt, and H. L. Harney. Total fusion cross section for the ^{16}O+^{16}O system. *Phys. Rev. C*, 18:1688, 1978. 110

[142] J. E. Johnstone, R. Kumar, S. Hudan, V. Singh, R. T. deSouza, J. Allen, D. W. Bardayan, D. Blankstein, C. Boomershine, S. Carmichael, A. Clark, S. Coil, S. L. Henderson, and P. D. O'Malley. MuSIC@Indiana: An effective tool for accurate measurement of fusion with low-intensity radioactive beams. *Nucl. Instr. Meth. A*, 1014:165697, 2021. 112

James E. Johnstone
jej13@iu.edu
ORCID: 0000-0002-1862-6832
ResearcherID: I-5201-2016

Education
Indiana University Bloomington
- PhD Chemistry with a concentration in Physical, Department of Chemistry (completed August 2022)

Abilene Christian University
- BS, Dual Majors in Chemistry and Physics, Department of Chemistry and Biochemistry and Department of Engineering and Physics (completed May 2017)

ACS Nuclear and Radiochemistry Summer School
- Six-week course in nuclear and radiochemistry including lab offered at Brookhaven National Lab (June 2015-July 2015)

Instructional Experience
Indiana University Department of Chemistry
Nuclear Chemistry Associate Instructor (fall semester 2019, fall semester 2020, fall semester 2021)
- Conducted discussion section for the course
- Aided students on homework problems and preparation for exams
- Graded all homework and exams
- Taught course lectures during professor absence or for special topics of current research
- Experience teaching in-person and online

Abilene Christian University Department of Engineering and Physics
Departmental Tutor (September 2014 – December 2015)
- Aided groups of students in understanding concepts in math, physics, and engineering
- Prepared students for upcoming exams

General Physics Lab Assistant (September 2013 – May 2015)
- Assisted in the set-up and tear down of lab equipment
- Oversaw and guided the lab participants during the execution of the lab

Engineering Physics II Teaching Assistant (August 2016 – December 2016)
- Graded all homework assignments

Optics Lab Assistant (August 2016 – December 2016)
- Assisted in the set-up and tear down of lab equipment
- Guided the students in completing each lab during the scheduled lab time
- Supervised students working in the lab during unscheduled lab times

Abilene Christian University Department of Chemistry and Biochemistry
Physical Chemistry Lab Assistant (August 2016 – May 2017)
- Was responsible for the set-up and tear down of lab equipment every week
- Primary supervisor for the students while conducting labs

Abilene Christian University Athletic Department
Individual Tutor (January 2015 – May 2015)
- Used chemistry knowledge and teaching experience as a one-on-one tutor for a student-athlete taking organic chemistry

Research Experience
Indiana University Bloomington
Graduate Research Assistant (July 2017 – present)
- Studying the fusion of neutron-rich isotopes in the lab of Dr. Romualdo deSouza
- Prepared and characterized high-quality thin silicon films for use as targets in fusion studies involving radioactive beams
- Prepared for and executed E17002 at NSCL/ReA3 to measure the fusion excitation functions of ^{36,44}Ar/^{41,45}K + ^{28}Si/^{16}O
- Designed, constructed, and commissioned a Multi-Sampling Ionization Chamber (MuSIC) for use in fusion studies involving low-intensity, neutron-rich beams

Abilene Christian University Department of Chemistry and Biochemistry
Undergraduate Research Assistant (September 2014 – May 2017)
- Studied novel osmium-containing compounds in the lab of Dr. Gregory Powell
- Synthesized new inorganic compounds using a microwave reactor
- Characterized and purified compounds using thin-layer chromatography/column chromatography
- Crystallized compounds using slow evaporation and layering techniques

Texas A&M University Department of Chemistry
Undergraduate Research Assistant (May 2016 – August 2016)
- Studied the photodissociation of carbonyl sulfide in the lab of Dr. Simon North
- Worked with multiple lasers and imaging systems as well as various computational programs

Conferences and Presentations
1. **American Physical Society April Meeting (April 2022)**
   - "Insight into the effects of shell structure on the fusion of mid-mass nuclei using isotopic chains of K and Ar nuclei on a Si target"
2. **Indiana University Department of Chemistry End-of-Year Symposium (April 2021)**
   - "Understanding the character of neutron-rich matter"
3. **Indiana University Department of Chemistry Physical Chemistry Seminar (February 2020)**
   - "Measurement of the fusion excitation functions for ^{41,45}K + ^{28}Si and ^{36,44}Ar + ^{28}Si at near-barrier energies"
4. **Fall Meeting of the American Physical Society Division of Nuclear Physics (October 2019)**
   - "Measurement of the fusion excitation functions for ^{41,45}K + ^{28}Si and ^{36,44}Ar + ^{28}Si at near-barrier energies"
   - "Design, Simulation and Construction of MuSIC@Indiana"
5. **Gordon Research Seminar in Nuclear Chemistry (June 2019)**
   - "Comparing Fusion for Stable and Radioactive K and Ar Isotopes on a Si Target"
6. **American Physical Society April Meeting (April 2019)**
   - "Production of thin, self-supporting ^{28}Si foils for near barrier fusion experiments with radioactive beams"
   - "Measuring the fusion excitation functions for ^{41,45}K + ^{28}Si and ^{36,44}Ar + ^{28}Si"
   - "Probing fusion by using an isotopic chain of neutron-rich oxygen isotopes to bombard a carbon target"

7. **American Physical Society April Meeting (April 2018)**
   - "Incorporating position sensitivity into an ExB design microchannel plate detector"
   - "Measuring fusion of ^{41,45}K and ^{36,44}Ar with ^{28}Si target nuclei at near barrier energies"
8. **American Chemical Society Meeting in Miniature (April 2016)**
   - "Osmium Carbonyl Clusters with Metal-Containing Dicarboxylate Ligands"
9. **Abilene Christian University Undergraduate Research Festival (April 2016)**
   - "Osmium Carbonyl Clusters with Iodine Atoms"
10. **Texas A&M Summer Undergraduate Research Poster Presentation (August 2016)**
   - "Photodissociation of OCS at 230 nm"

Awards
- ACU University Scholar (2017)
- Sigma Pi Sigma Physics Honor Society Member (2017)
- ACS Undergraduate Award in Inorganic Chemistry (2017)
- ACU Chemistry Department Paul C. Witt Award (2017)
- Society of Physics Students Sigma Pi Sigma Honor Society Member (2016)
- Perry C. Reeves Research Scholar Award (2016)
- American Association of Physics Teachers Outstanding Physics Learning Assistant (2015)
- Alphi Chi Honor Society Member (2014)
- Phi Eta Sigma Honor Society Member (2014)
- Scotts Miracle-Gro Scholarship Award (2013-2017)
- Eagle Scout Rank Boy Scouts of America (2013)
- National Merit Scholar (2013)

Professional Affiliations
American Physical Society (2017 – present)
- Division of Nuclear Physics
- Division of Astrophysics
American Chemical Society (2015 – present)
- Nuclear Chemistry and Technology Division

Extracurricular Activities
ACU Chemistry Club: participant (August 2013 – May 2017), vice president (May 2015 – May 2016), and president (May 2016 – May 2017)
- Chemistry Circus (participant – 2013/2014, host – 2015)
- "What is a Scientist?" Day at Taylor Elementary School (2016)
ACU Engineers and Scientists Cooperative: participant (August 2013 – May 2017), secretary (August 2015 – May 2016)
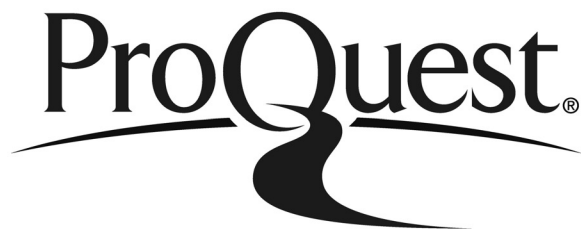
Published Work
1. James E. Johnstone, Varinderjit Singh, R. Giri, et al. **Proton and neutron exchange as a prelude to fusion at near-barrier energies**. Phys. Rev. C **106**, L011603 (2022).
2. James E. Johnstone, Rohit Kumar, Sylvie Hudan, Romualdo T. deSouza, J. Allen, D. W. Bardayan, D. Blankstein, C. Boomershine, S. Carmichael, A. Clark, S. Coil, S. L. Henderson, P.

D. O'Malley. **Improving the characterization of fusion in a MuSIC detector by spatial localization**. Nucl. Instrum. Methods Phys. Res. A. **1025**, 166212 (2022).

3. Varinderjit Singh, James E. Johnstone, Rekam Giri, et al. **Impact of shell structure on the fusion of neutron-rich mid-mass nuclei**. Phys. Rev. C **104**, L041601 (2021).

4. James E. Johnstone, Rohit Kumar, Sylvie Hudan, Varinderjit Singh, Romualdo T. deSouza, J. Allen, D. W. Bardayan, D. Blankenstein, C. Boomershine, S. Carmichael, A. M. Clark, S. Coil, S. L. Henderson, P. D. O'Malley. **MuSIC@Indiana: an effective tool for accurate measurement of fusion with low-intensity radioactive beams**. Nucl. Instrum. Methods Phys. Res. A. **1014**, 165697 (2021).

5. James E. Johnstone, Sylvie Hudan, Carley Folluo, Tyler Werke, Paul A. DeYoung, Romualdo T. deSouza. **Production and characterization of thin, self-supporting Si foils for use as targets in radioactive beam experiments**. Nucl. Instrum. Methods Phys. Res. A. **953**, 163267 (2020).

6. Kylie M. Wilson, John W. Swartout, Henry A. Touchton, Erica N. Lambert, James E. Johnstone, Ashley K. Archambeau, David M. Marolf, Emily R. Mikeska, Vincent M. Lynch, Vladimir N. Nesterov, Eric W. Reinheimer, Gregory L. Powell, Cynthia B. Powell. **Asymmetric diosmium sawhorse complexes**. Act. Crystallogr C Struct Chem. **C75**, 529-537 (2019).

7. Amanda C. Dugan, Brittney S.N. Nolan, Kristen L. Brehm, Joel L. Jackson Jr., Nigel Gwini, Sarah D. Floris, David M. Marolf, James E. Johnstone, Soo Hun Yoon, Gregory L. Powell, Vladimir N. Nesterov, Hannah M. Johnston, Kayle N. Green. **Triosmium carbonyl complexes with multiple 1,3,5-triaza-7-phosphaadamantane (PTA) ligands: Synthesis of a new water-soluble Os3 cluster**. Polyhedron. **114**, 292-298 (2016).

8. Jade Y. Jung, David K. Kempe, Soo Hun Yoon, Nigel Gwini, Audrey G. Fikes, David M. Marolf, Michelle L. Parker, James E. Johnstone, Gregory L. Powell, Li Yang, Vladimir Nesterov, Michael G. Richmond. **Microwave-induced dppm ligand substitution in triosmium clusters: Structural and DFT evaluation of Os-3 clusters containing multiply activated dppm ligands through cyclometalation, ortho metalation, and P-C bond cleavage**. Journal of Organometallic Chemistry. **813**, 15-25 (2016).

ProQuest Number: 29321765

INFORMATION TO ALL USERS
The quality and completeness of this reproduction is dependent on the quality
and completeness of the copy made available to ProQuest.